PERIODIC CELLULAR CORES WITH TAILORED ARCHITECTURES FOR IMPROVED MECHANICAL PROPERTIES

by

Omar Abdulhadi Al Osman

A Thesis Presented to the Faculty of the
American University of Sharjah
College of Arts and Science
in Partial Fulfillment
of the Requirements
for the Degree of

Doctor of Philosophy in
Material Science and Engineering

Sharjah, United Arab Emirates

September 2024

Declaration of Authorship

I declare that this (dissertation) is my own work and, to the best of my knowledge and belief, it does not contain material published or written by a third party, except where permission has been obtained and/or appropriately cited through full and accurate referencing.

Signature: Omar Al Osman

Date: September 23, 2024

Approvals

We, the undersigned, approve the PhD Dissertation written by: Omar Al Osman.

Dissertation Title: Periodic Cellular Cores with Tailored Architectures for Improved Mechanical Properties

Date of Defense: September 23, 2024

Name, Title and Affiliation
Dr. Maen Alkhader Professor Department of Mechanical Engineering Dissertation Advisor
Dr. Wael Abuzaid Associate Professor Department of Mechanical Engineering Dissertation Co-advisor
Dr. Mehmet Eglimez Professor Department of Physics Dissertation Committee Member
Dr. Mohammad Hamdan Professor Department of Mechanical Engineering Dissertation Committee Member
Dr. Rami Haweeleh Professor Department of Civil Engineering Dissertation Committee Member
Dr. T.A. Venkatesh Associate Professor Department Materials Science and Chemical Engineering\ Stony Brook University Dissertation Examiner

Accepted by:
Dr. Mohamed El-Tarhuni
Vice Provost for Research and Graduate Studies
Office of Research and Graduate Studies

Acknowledgment

First and foremost, I extend my heartfelt gratitude to God for giving me strength and encouragement throughout the challenging times during the completion of this dissertation. I am eternally grateful for the abundant blessing bestowed upon me, and no amount of thanks will ever suffice.

A special thanks and acknowledgment to my advisors, Dr. Maen Alkhader and Dr. Wael Abuzaid, for their contributions and continuous support provided throughout my doctoral thesis. Their guidance and support throughout this journey have been outstanding and exceptional. I have learned many lessons from them and will forever look up to them. I would also like to acknowledge the program coordinator, Dr. Ali Al Naser, for his unwavering support throughout the doctoral program. A special acknowledgment goes to the graduate office for financially supporting this work through a graduate research assistantship.

I am grateful for the guidance of my father, who always encouraged me to pursue my PhD and believed in my ability to achieve this remarkable goal. A special thank you goes to my mother, who has continuously supported me and for whom I will forever be grateful. I hope I have made you proud.

A special acknowledgment goes to my dear friend and colleague, Assil. I want to sincerely thank you for your continuous support and for always being there before and after my PhD. A special thanks go to the biomedical team, Nour and Waed, for being there during lunch breaks and continuously supporting my diet with homemade food. I also want to acknowledge Shahbaz and Tahir for their continuous technical help in the electrodeposition setup.

I would also like to acknowledge my siblings, Ahmad and Mira, for continuously listening to me as I shared my findings with them and for always trying to offer new insights when I felt stuck. Many thanks to Ahmad Naji for his unwavering support throughout my journey. A final and special thanks goes to my best friend, Yazan, who has continuously encouraged me throughout this journey, for which I will be forever grateful.

Abstract

Cellular solids, which include foams and lattice structures, exhibit uniquely high specific structural and thermal properties due to their porous structures, as well as their topological and morphological features. These properties make them attractive for various weight-sensitive applications in aerospace, automotive, and biomedical fields. This work aims to accelerate the use of cellular solids in engineering applications by enhancing their properties through tailoring their topological and morphological features. Multiple approaches were used in this work to enhance the mechanical and thermal properties of cellular solids. The first approach focused on coating metallic aluminum foams with copper to improve their properties. This research path employed both numerical and experimental techniques, including finite element analysis (FEA), electrodeposition, scanning electron microscopy (SEM), energy dispersive X-ray spectroscopy (EDS), and uniaxial quasi-static compression. Results showed that coating aluminum foam with 4% relative density with copper significantly enhances its stiffness and thermal conductivity. Improvements reaching 138% and 196% in stiffness and thermal conductivity were realized, respectively. Analytical models predicting the macroscopic stiffness, yield, and thermal conductivity of coated metallic foams were derived. These models are applicable to material systems other than the copper and aluminum system investigated, generalizing this work to assist engineers in designing hybrid coated metallic foams from a wide range of constituents compatible with electrodeposition. The second approach involved enhancing the mechanical properties of lattice structures by modifying their topology with sinusoidal perturbations. Numerical simulations were conducted to analyze the effects of these perturbations on the modified honeycomb's response to out-of-plane, in-plane, transverse shear, flexural loadings, and low-velocity impacts. Results showed that the sinusoidal perturbations can shift the failure mode from elastic buckling to yielding, increasing the peak load capacity by up to 28.5% under concentrated out-of-plane loads.

Keywords: *Finite Element Analysis (FEA), Cellular Solids, Scanning Electron Microscopy (SEM), Energy dispersive X-ray spectroscopy (EDS), Electrodeposition, Functionally Graded Coating, Energy Absorption*

Table of Contents

List of Figures

List of Tables

Chapter 1: Introduction

Cellular solids are materials that consist of a periodic cellular structure or a randomly porous structure. Gibson and Ashby [1] described cellular solids as materials composed of interconnected networks of solid struts or plates that form the cells' edges and faces. The network of solids or struts creates an assembly of prismatic or polyhedral cells with solid edges and faces packed periodically or randomly to fill space [2]. Based on the packing configuration, cellular solids are classified into lattices, foams, and Triply Periodic Minimal Surfaces (TPMS). A cellular structure is often characterized by its underlying repeating unit-cell shape and relative density [1]. Generally, cellular structures are divided into two groups: lattice-based or stochastic.

Lattice structures are a class of cellular solids consisting of a periodic unit cell, often two-dimensional and extruded in the out-of-plane dimension. Due to their periodicity, lattice structures exhibit a high degree of symmetry and predictable properties that are appealing for various engineering applications. The most commonly used lattice unit-cells are square [3], Hexagonal [4], triangular [5], Re-entrant [6], and truss [7]. The variety of shapes used in lattice structures allows for tuning the mechanical or thermal properties based on specific applications. Recently, three-dimensional lattice structures have been proposed. The most common type is TPMS structures. These consist of a periodic three-dimensional polyhedral unit cell that repeats in all directions. TPMS structures allow for realizing the lowest possible surface area occupying a given volume [8]. This property makes the structures appealing for applications favoring high surface area-to-volume ratios. Some of the most commonly used TPMS unit cells are the Gyroid [9], Diamond [10], and Schwarz [11].

Stochastic cellular solids, commonly known as foam structures, consist of a randomly distributed network of three-dimensional polyhedral cells. Unlike lattice structures, foams consist of an irregular distribution of pores. The irregularity of the foam structures can be characterized using various mathematical approaches such as the Voronoi tessellations [12]. The relative density of foams is generally much lower than that of lattice structures. Gibson and Ashby [1] have characterized foam structures to have a minimum porosity of 80%. A general classification tree of cellular solids is shown in Figure 1.

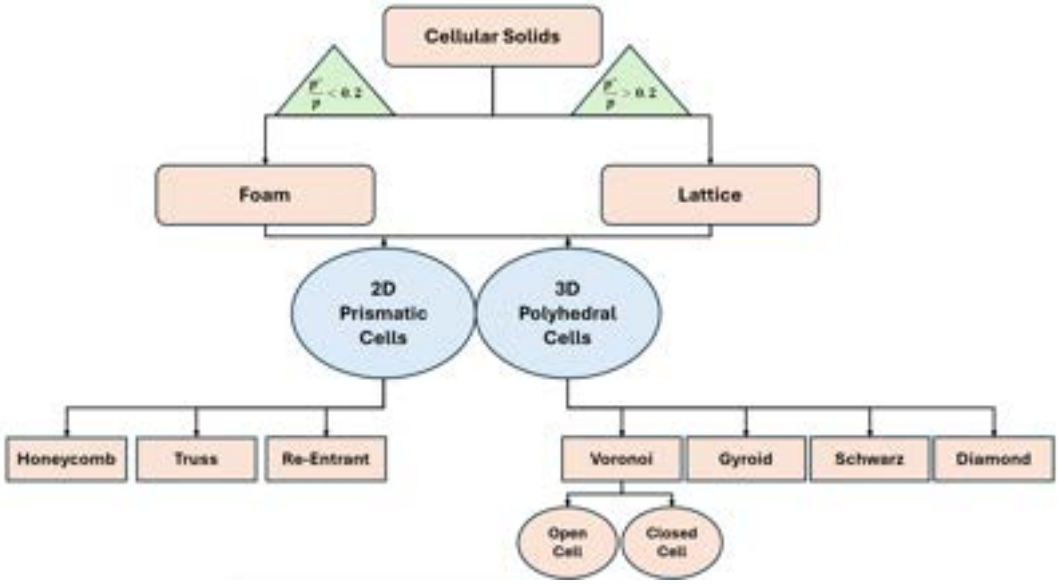

Figure 1: Classification tree of cellular solids

Cellular solids deliver high stiffness and strength-to-weight ratios and offer excellent ability to mitigate impact energy. In addition, they are helpful in noise reduction and damping, and they have unique thermal properties due to their porous structure and high surface area. Accordingly, cellular solids are used in various applications across various industries. Most prominently, cellular solids are used as cores in sandwich structures used in aerospace [13], [14], automotive [15], [16], marine [17], highway bridged [18] and biomedical applications[19], [20], [21], [21], [22]. In addition, cellular solids are used in high-performance heat exchangers [23], [24].

The industrial relevance of cellular solids has motivated improving their properties to accelerate their adoption and optimize their performance. The move to optimize cellular solids' properties has also been motivated by the advancement of the manufacturing industry in which Machine learning, finite element analysis, computer-aided design, and additive manufacturing have been integrated. This integration opened doors for tailoring the microscale [16] and macroscale [13] properties of cellular solids to meet the demand of specific applications. Multiple approaches have been followed to enhance the properties of cellular solids. These include utilizing special topologies such as TPMS topologies [15] or optimizing cellular solids porosity [17]. Such techniques allowed for realizing improved stiffness and strength-to-weight ratios as well as high surface areas. However, tuning the porosity or topology of cellular solids to optimize their properties proved expensive and impractical, as fabricating most of

the proposed high-performance topologies (e.g., TMPS) requires utilizing expensive additive manufacturing (AM) techniques. Generally, when used in industrial applications, cellular solids are used in large amounts. Accordingly, there is a need to develop cellular solids with improved properties that can be mass-produced with the need to utilize additive manufacturing. This work aims to satisfy this requirement by developing cellular solids with enhanced properties that can be mass-produced using conventional manufacturing methods. In this dissertation, two approaches were taken to enhance the mechanical properties of cellular material. The first approach compromises developing hybrid coated metallic open-cell foams using electrodeposition, which will be conducted through numerical, experimental, and analytical setups. The second approach focuses on modifying the cellular topology of aluminum honeycombs by introducing sinusoidal perturbations with the aim of enhancing the energy absorption capabilities and out-of-plane compression applications.

Chapter 2: Literature Review

This chapter provides a detailed background regarding cellular solids, their mechanical and thermal properties, and the parameters affecting their properties.

2.1 Mechanical Properties

Cellular solids are of great interest to numerous researchers due to their unique mechanical and thermal properties, which makes them appealing for various engineering applications. From a mechanical perspective, the main property governing the behavior of cellular solids is the relative density [1]. Relative density is the ratio of the density of the cellular material (p^*) to the density of its constituent material (p). The relative density is inversely related to the porosity (ϕ) of the structure, where $\phi = 1 - p^*/p$. As the density of a cellular structure increases, the porosity decreases as more solid fills up the gaseous phase in the material. As previously discussed, foam structures can feature cells with different cell shapes and distributions, either regular or irregular. Nevertheless, their relative density typically remains low, at around 0.2. Topological modifications to cellular materials can be done by varying the cell shape [25] or cell size [26]. Based on different experimental and analytical solutions, the mechanical and thermal properties depend weakly on the cell size [1]. However, that is not the case for the cell shape, as different cell shapes exhibit different mechanical properties.

2.1.1 Cell shape

The regularity and distribution of the cells within the cellular core, regardless of the cell shape, affect the overall uniformity of the structure. If the cells are equal in all sizes, the core is isotropic. However, if the cells are elongated or flattened, the structure is anisotropic, and the mechanical behavior is sensitive to the loading direction [27]. Moreover, a three-dimensional cell shape compared to a two-dimensional cell also affects the mechanical properties. Figure 2 shows the different cell shapes that are often used in 2D and 3D cellular solids. While it should be noted that the depicted cell shapes are frequently used, the cells are not representative of an exhaustive list, as new cell shapes continue to emerge with the aim of optimizing the mechanical and thermal properties of cellular solids. The variety of cell shapes allows for more geometrical variables that can be tuned to achieve the required properties. Each unit cell's relative density can be calculated based on the geometric properties of the unit cell.

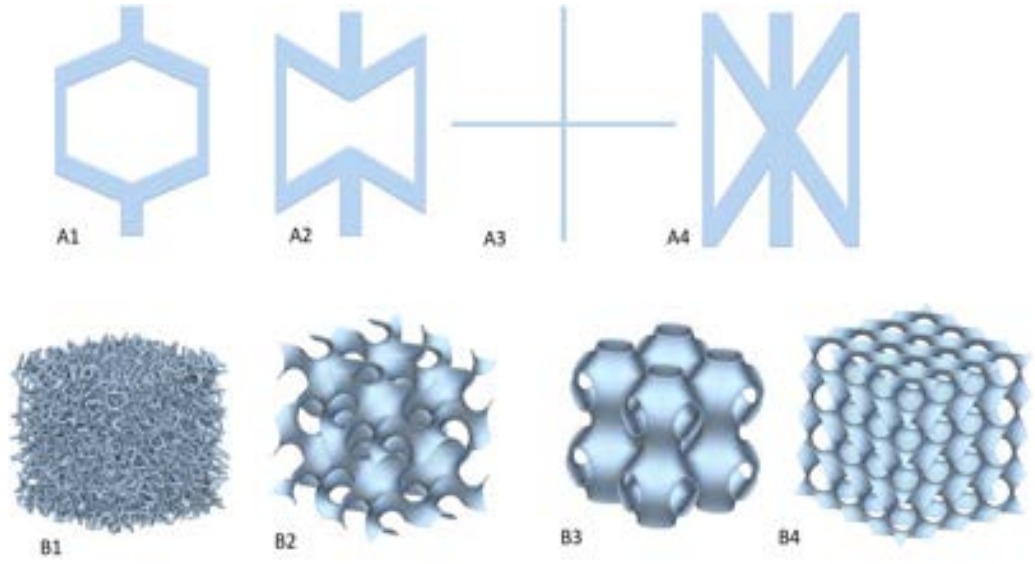

Figure 2: A1) Honeycomb A2) Re-entrant A3) Square A4) Triangular B1) Voronoi B2) Gyroid B3) Schwarz B4) Diamond

For example, Gibson and Ashby [1] have analytically approximated the relative density of a regular honeycomb unit cell with $h = l$ and $\theta = 30$ as

$$\frac{\rho^*}{\rho} = \frac{t/l(h/l+2)}{2cos\theta(h/l+sin\theta)} = \frac{2}{\sqrt{3}}\frac{t}{l} \quad (1)$$

where t is the cell wall thickness, l is the strut length, h is the height of a unit cell, and θ is the angle between the struts. Similarly, the analytical relative density for other unit cells can be determined based on their geometrical features.

The macro-scale properties of a cellular solid are influenced not only by its cell shape and relative density but also by the mechanical and thermal behavior of its constituent material. These materials can include metals [28], polymers [29], ceramics [30], glasses [31], or even composites [32].

2.1.2 In-plane mechanical properties

Two-dimensional cellular solids such as honeycombs have two distinct direction-dependent behaviors: in-plane and out-of-plane. The out-of-plane direction is aligned with the extrusion direction and is usually much stiffer and stronger than the in-plane direction. However, the in-plane direction usually delivers specific energy absorption. 2D cellular solids are able to absorb and dissipate energy effectively in their in-plane direction. When a 2D cellular solid is subjected to an in-plane

compressive load, the response of the solid passes through three phases: linear elastic, non-linear plastic, and densification. During the linear elastic phase, the cell walls are subjected to elastic bending. Once the strains exceed a critical limit, deformation in cell walls becomes plastic. Both plastic yielding and buckling can occur, depending on the nature of the cell wall material as well as the topological features of the unit cell. As cells collapse and cell walls start to touch each other, the stiffness of the structure increases rapidly, marking the start of the densification stage. Due to the nature of cellular solids, the densification stage occurs as the pores within the unit cells begin closing, and the structure starts absorbing energy. The stiffness of the structure rapidly increases once all the cell walls are completely collapsed. At this stage, the cellular structure no longer has any pores and thus acts as a thin plate. Figure 3 shows the stress-strain behavior of classical 2D cellular solids (e.g., honeycomb structure) under in-plane compression [1].

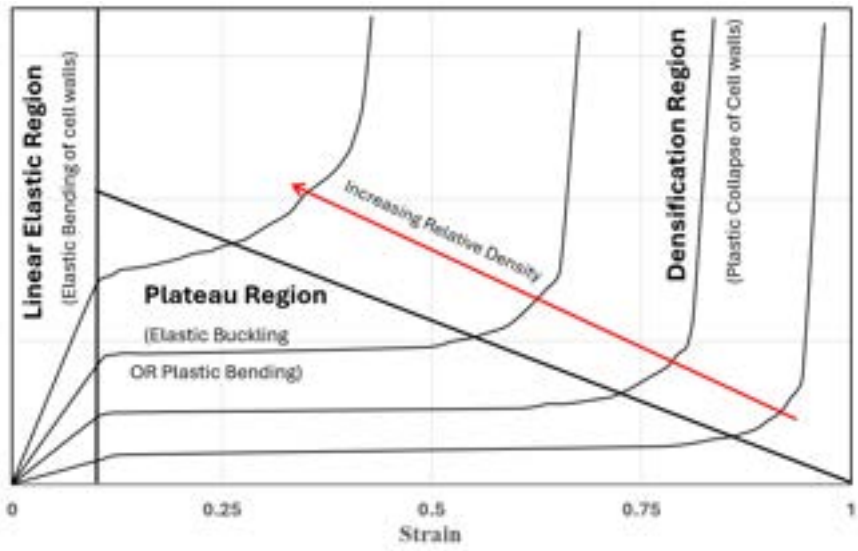

Figure 3: Stress vs. strain diagram of in-plane uni-axial compression of a honeycomb structure

The three phases of deformation are governed by the relative density, which is in direct relationship with the length of the struts l and the cell wall thickness t. As the cell walls become thicker, consequently increasing the relative density, the overall performance of the cellular structure is enhanced with the drawback of increasing the weight. From Figure 3, the elastic stiffness, plateau stress, and densification strain are significantly increasing as the relative density increases. The plastic region can include

buckling, yielding, or brittle fracture, depending on the constituent material. The in-plane tensile behavior is slightly different than that of the compression. The linear elastic region is equivalent for both behaviors with the same modulus. However, in the plastic region, the cell walls do not undergo buckling behavior; instead, the cell walls rotate towards the tensile axis, which causes the overall stiffness to increase. In the case of a brittle constituent material, the cell walls tend to fail abruptly in tension without minimal non-linear deformations.

For in-plane compression and tension behavior, the standard beam theory can be applied to calculate the elastic modulus of the material. Figure 4 shows a unit cell of a honeycomb subjected to uniaxial compression.

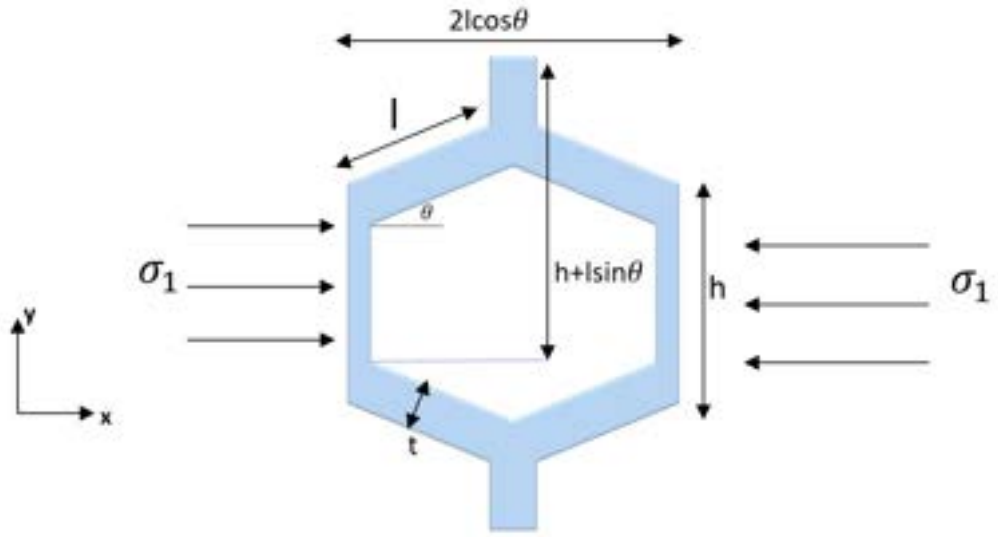

Figure 4: Honeycomb unit-cell under uni-axial compression

The height h and length l are often equal to each other for a standard hexagonal honeycomb, which renders the inplane behavior isotropic since the cells are equal and symmetric in both directions. During mass manufacturing of metallic honeycombs, the cell walls are often piled on top of each other to create the cellular structure, which makes the vertical overlapping cell walls have a double thickness compared to the inclined struts. However, to calculate the Elastic modulus analytically, a uniform thickness is assumed for the unit cell. The total length of the unit cell is calculated to be $2lcos\theta$ in the x-direction and $h + lsin\theta$ in the y-direction. As the load is applied to

the unit cell, the struts are subjected to local deformations δ. The stress applied to the unit cell in the *x*-direction, σ_1, can be calculated as

$$\sigma_1 = \frac{P}{A} = \frac{P}{(h+lsin\theta)b} \tag{2}$$

where b is the in-depth thickness of the unit cell in the z-direction. Similarly, the strain on the unit cell is the deformation of the unit cell in the x-direction divided by the total length of the strut in the *x*-direction.

$$\epsilon_1 = \frac{\delta sin\theta}{lcos\theta} \tag{3}$$

Thus, the elastic modulus can be calculated as

$$E = \frac{\sigma_1}{\epsilon_1} = \frac{\frac{F}{(h+lsin\theta)b}}{\frac{\delta sin\theta}{lcos\theta}} \tag{4}$$

The deflection of a honeycomb unit cell is calculated as [1]

$$\delta = \frac{Psin\theta l^3}{12E_s I} \tag{5}$$

where $Psin\theta$ is the applied load in the direction of the inclined strut, E_s is the Young's Modulus of the solid constituent material, and I is the second moment of inertia of a cell wall. If the wall is assumed to have a rectangular cross-section, then $I = bt^3/12$. Substituting the deflection equation in the Young's Modulus equation,

$$E = \frac{P}{h+lsin\theta} * \frac{lcos\theta}{Psin^2\theta l^3} * \frac{12E_s bt^3}{12} \tag{6}$$

this can be simplified into

$$\frac{E}{E_s} = \left(\frac{t}{l}\right)^3 \frac{cos\theta}{(h/l+sin\theta)sin^2\theta} \tag{7}$$

the in-plane Young's modulus is a function of the constituent's material's Young's modulus E_s, the relative density of the honeycomb core $(t/l)^3$ and the cell geometry h, l, and θ. The in-plane properties are similar in both the *x* and *y* directions, given that the honeycomb is a regular shape where $h = l$. Similarly, the inplane elastic modulus can be calculated for different periodic cell shapes. However, for a Voronoi foam-based

structure, the response would depend on the randomness of the foam. Based on Gibson and Ashby's derivation [1], the normalized elastic modulus for open-cell and closed-cell foams, respectively, are

$$\frac{E}{E_s} = C_1 \left(\frac{\rho^*}{\rho_s}\right)^2 \tag{8}$$

$$\frac{E}{E_s} = C_2 \phi^2 \left(\frac{\rho^*}{\rho_s}\right)^2 + C_3 (1-\phi) \frac{\rho^*}{\rho_s} \tag{9}$$

where C_1,C_2 and C_3 are constants based on the geometrical features of the random distribution of the cells.

2.1.3 Compressive strength: cell collapse

The collapse of honeycomb unit cells, or any other cellular shape, can occur due to elastic bucking or plastic yielding [33]. Elastic buckling in cellular solids occurs when the struts of the unit cell undergo axial or bending loads, where if the load exceeds the critical buckling load, the structure undergoes sudden deformation or buckling. Plastic yielding implies that the deformation occurring in the cell walls exceeds the plastic yield strength; thus, local deformations occur, and as the load increases, the number of cells undergoing plastic deformation increases. Figure 5 shows the plastic-yielding deformation behavior of an aluminum honeycomb under in-plane compressive strength [34]. As the load increases initially in Figure 5a, the aluminum honeycomb undergoes elastic deformation. As the load incrementally increases, some of the cell walls begin to yield, which causes local deformation, as illustrated in Figure 5b. As the load increases, the cell walls continue to yield and end up collapsing, as shown in Figure 5c and Figure 5d. As for elastic buckling, Figure 6 shows the elastic buckling modes, in which a honeycomb unit cell that is loaded in the y-direction undergoes elastic deformations. It is important to note that if the loading direction is changed to the x-direction, the force act perpendicular to the longer dimension of the unit-cell, causing the cell walls to simply bend.

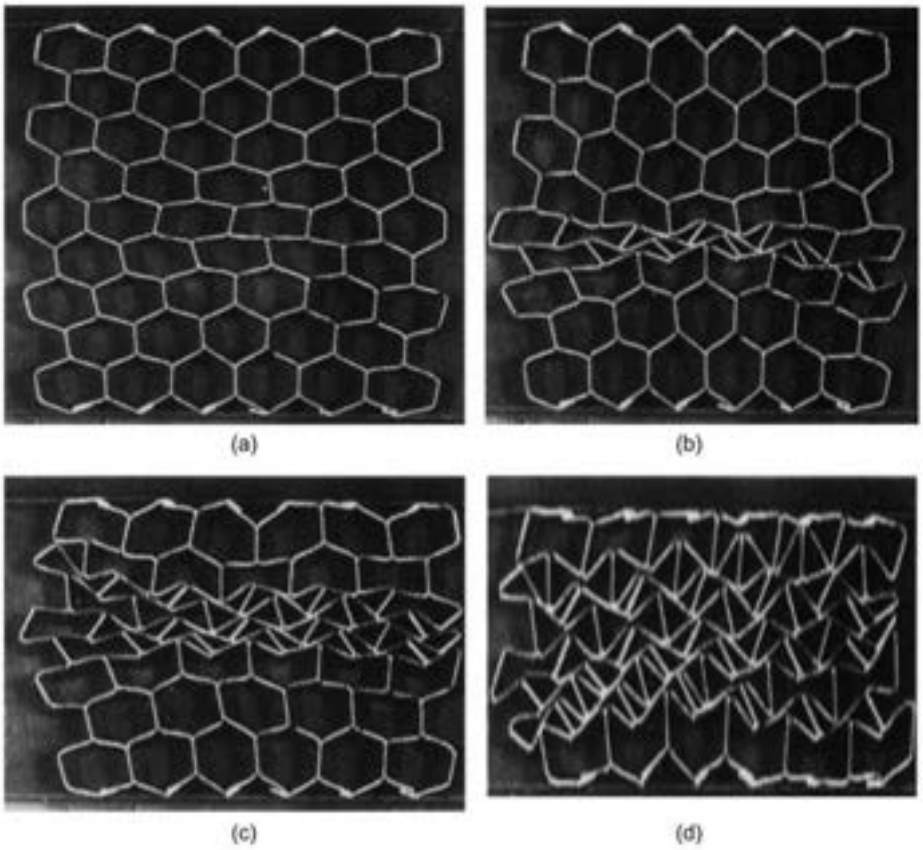

Figure 5: Deformation mechanism due to the plastic collapse of aluminum honeycomb (a) Symmetric Deformation of cell walls (b) Center row collapse due to shear failure caused by nonlinear deformations (c) Symmetric deformation leading to densification of cell walls (d) Unsymmetrical collapse that is followed by shear collapse [35]

The structure bends in the x-direction, as opposed to buckling in the y-direction, as the walls act as simply supported beams and are loaded in the transverse direction [1].

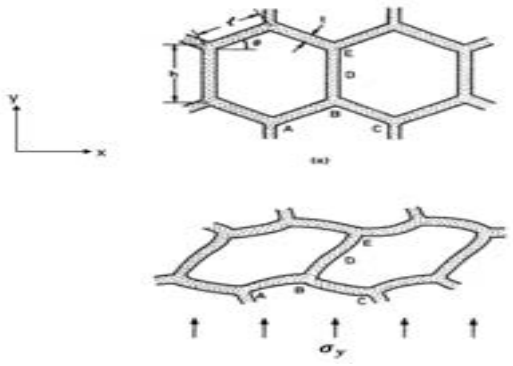

Figure 6: a) Traditional honeycomb unit-cell b) elastic buckling of honeycomb unit-cell loaded in the y-direction [1]

2.1.3.1 Elastic buckling

As shown in Figure 6, it is evident that the buckling behavior of the cell walls is similar to that of the Euler buckling load [35], [36]. The critical Euler buckling load, which is often used as column buckling [37], is given by

$$P_{cr} = \frac{n^2 \pi^2 E_s I}{h^2} \tag{10}$$

where n is an end-constraint that depends on the boundary conditions of the column. The end constraints n for the cell walls depend on the stiffness of the adjacent inclined struts. As shown in Figure 6, the joints at which the struts are connected rotate as the vertical cell walls undergo elastic buckling. Therefore, the rotational stiffness of the vertical and the inclined struts is the determining factor of the end-constraint factor n. The constraint factor can be calculated using experimental means [38] or analytical means [1]. Accordingly, the elastic buckling stress can be calculated as

$$\sigma_{el} = \frac{P_{cr}}{2lcos\theta b} = \frac{n^2 \pi^2 E_s}{h^2 2lcos\theta b} \frac{bt^3}{12} \tag{11}$$

this is rearranged into the final form of

$$\frac{\sigma_{el}}{E_s} = \frac{n^2 \pi^2}{24} \frac{(t/l)^3}{(h/l)^2 cos\theta} \tag{12}$$

Based on the analytical analysis that has been conducted by Gibson and Ashby [1], in which they have used elastic line analysis to compute the end constraints, the elastic buckling stress for a regular honeycomb is

$$\frac{\sigma_{el}}{E_s} = 0.22(t/l)^3 \tag{13}$$

The previous analysis can be modified to fit unit cells with different geometrical features, such as the unit cells of the rectangular, re-entrant, or even the random Voronoi foam structure.

2.1.3.2 Plastic yielding

After the elastic critical load is reached, the cell walls tend to yield plastically, which means that the cell walls can no longer revert to their original shape. During plastic buckling, the stiffness of the cell walls tends to deteriorate, which causes a decrease in the load-bearing capacity and overall stability of the structures. For a honeycomb structure, the cell walls begin to buckle as they reach their respective plastic

bending moment. The plastic buckling stress is equivalent to the plateau stress in which the cell walls collapse. Once the stress in the cell walls reaches the yield stress of the constituent material, yielding begins, and the cell walls start to collapse plastically. The end joints of the struts tend to yield initially, and as the force increases, the yielding propagates to the rest of the strut. As the entire cross-section of the strut yields, it forms a "plastic hinge" in which the section is able to rotate like a pin joint [39]. The internal plastic moment that forms at the plastic hinges (once the entire cross-section has yielded) is

$$M_p = \sigma_{ys}\left(\frac{bt}{2}\right)\frac{t}{2} = \sigma_{ys}\frac{bt^2}{4} \tag{14}$$

where the term $\sigma_{ys}\left(\frac{bt}{2}\right)$ is the load due to the applied stresses and $\frac{t}{2}$ is the effective length between the force and the plastic hinge [1]. From the summation of moments on one of the joints, the applied moment can be expressed as

$$M_{app} = \frac{Flsin\theta}{2} \tag{15}$$

As discussed earlier, plastic hinges develop once the entire cross-section has yielded, and this occurs when the applied moment is equivalent to the internal plastic moments [39]. The Force F in the previous equation can be re-written in terms of stresses so that the final plastic stress σ_{pl} can be calculated.

$$M_{app} = \left(\sigma_{pl}\right)(h + lsin\theta)\left(\frac{lsin\theta}{2}\right) = M_p = \sigma_{ys}\frac{bt^2}{4} \tag{16}$$

Rearranging the equation, the plastic collapse stress is given as [1]

$$\frac{\sigma_{pl}}{\sigma_{ys}} = (t/l)^2\frac{1}{2(h/l+sin\theta)sin\theta} \tag{17}$$

Similar to the derived modulus and elastic buckling stress, the plastic collapse stress is dependent on the material, relative density (t/l) and the geometric features of the unit cell. For a regular honeycomb, where $h = l$ and $\theta = 30$, the plastic collapse stress can be calculated as

$$\frac{\sigma_{pl}}{\sigma_{ys}} = \frac{2}{3}\left(\frac{t}{l}\right)^2 \tag{18}$$

The shown procedure can be followed to derive the plastic collapse stresses for various other cell shapes with different geometric features. The collapse of the unit cell is dependent on either the plastic yielding or the elastic buckling strength, depending on which stress is lower. In order to determine the critical relative density that is required for a cellular honeycomb structure to buckle elastically, the two equations are equated to each other. Similarly, following the same approach, Zhang et al. [40] calculated the critical relative density to predict the failure modes for additively manufactured octagonal honeycombs [41] for nanoporous foam structures. As the critical relative density is calculated, researchers can predict the failure modes, whether it is due to elastic buckling or plastic yielding, with respect to the relative density of the structure. For honeycomb topology, the critical relative density is calculated below.

$$(E_s)\frac{n^2\pi^2}{24}\frac{(t/l)^3}{(h/l)^2 cos\theta} = \frac{\sigma_{ys}(t/l)^2}{2cos^2\theta} \tag{19}$$

Rearranging the equation and keeping (t/l) on one side results in

$$(t/l)_{crit} = \frac{12}{n^2\pi^2}\frac{(h/l)^2}{cos\theta}\frac{\sigma_{ys}}{E_s} \tag{20}$$

If the relative density is above the critical relative density, the honeycomb structure ought to elastically buckle prior to yielding. In contrast, if the relative density is higher than the critical relative density, the structure undergoes plastic yielding. So, for a regular hexagonal honeycomb, where $h = l$ and $\theta = 30$, the critical relative density can be reduced to

$$(t/l)_{crit} = 3\frac{\sigma_{ys}}{E_s} \tag{21}$$

Based on the solid material that a regular hexagonal honeycomb is made from, the in-plane failures can be predicted. For metals, the ratio of yield stress to Young's modulus is very low, which means that the structure is more likely to yield rather than elastically buckle in the in-plane direction unless the relative density is extremely low (0.5% and lower). However, for regular polymeric honeycombs, the ratio of yield stress to Young's modulus is higher, which means that in regular polymeric honeycombs, structures are more likely to buckle elastically than yield when loaded in the in-plane direction.

2.1.4 Out-of-plane properties

The out-of-plane mechanical behavior of cellular solids is crucial to study as they are directly related to the energy absorption capabilities of the cellular structure. The out-of-plane properties imply that the structure is being loaded in a direction perpendicular to the plane of material or structure, the z-direction. One prominent engineering application where the study of out-of-plane properties of cellular solids is essential is their use in sandwich panels [5], [7], [42].

The reason for that is sandwich panels with cellular cores tend to have a high stiffness-to-weight ratio and are able to absorb high energies relative to their weight. The use of cellular sandwich panels extends to different fields, such as aerospace [13], automotive [43], marine [44], and construction industry [45]. When loaded in the z-direction, any cellular shape tends to experience buckling or crushing behavior, and often the stiffness and plateau stresses that were calculated in the previous section for the in-plane behavior are much higher. This is because axial and bending deformations are involved. Figure 7 shows the out-of-plane direction for a honeycomb unit cell. It is evident from the figure that the deformation occurring in the out-of-plane direction is different than that of the in-plane. Therefore, the mechanical behavior is different. The Young's modulus in the z-direction is derived in a similar fashion to that in the in-plane direction. Young's modulus in the z-direction is [1].

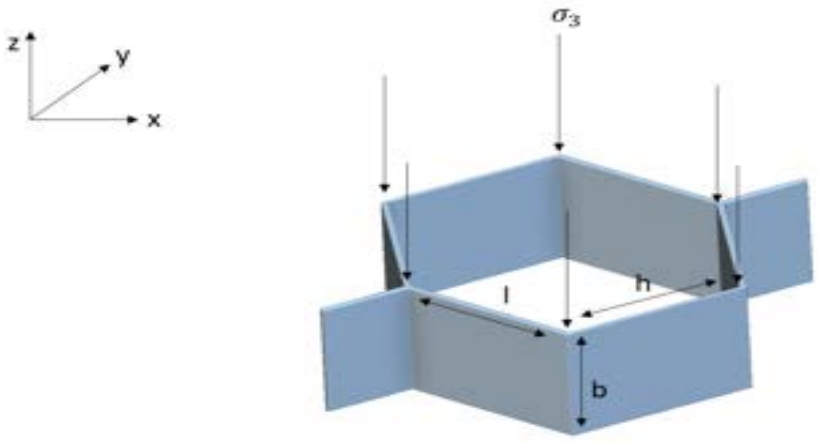

Figure 7: Out-of-plane loading directions on a honeycomb unit-cell

$$\frac{E}{E_s} = \left(\frac{t}{l}\right)\frac{(h/l)+2}{2(h/l+sin\theta)cos\theta} \tag{22}$$

Compared to the in-plane elastic modulus, the relative density, or the ratio of the wall thickness to the inclined length, is to the power of 3 in Equation (7), whereas the elastic modulus in the z-direction is only to the power of one. Therefore, the mechanical properties are significantly different depending on the loading direction. Thus, when comparing x and y-direction loadings to the z-direction, the honeycomb unit cell is anisotropic.

2.1.4.1 Elastic buckling

To estimate the elastic buckling, authors have treated the cell walls of cellular materials as plates [1], [46], [47] and calculated the final elastic buckling stress as the sum of all the buckling stresses on all the plates. For the in-plane direction, the buckling of the cell walls is determined by assuming that the buckling behavior follows the Euler load buckling. The critical buckling load for a plate is given in Equation (23) [48]:

$$P_{cr} = \frac{KE_s t^3}{(1-v_s)h} \tag{23}$$

where K is an end-constraint factor that is dependent on the boundary conditions, t is the thickness of the plate, and v_s is the Poisson's ratio of the plate's solid material. Similar to the in-plane direction, the end constraint Factor K is dependent on the stiffness of the adjacent cell walls. The value K is approximated based on the geometrical features of the unit cell. For example, for a square honeycomb, [47] has approximated K from experimental tests to be around 4 for square honeycombs, whereas [1] has estimated K to be 6.2 for $b > 3l$ if the plate joints are assumed to be fully fixed and K to be 2 if the cell walls are free to rotate. Assuming a commercial honeycomb unit-cell with cell walls with thickness t on the inclined walls and double thickness on the overlapping walls $2t$, the elastic buckling stress can be calculated using the following governing Equation (24) [49],

$$\frac{\partial^4 w}{\partial x} + 2\frac{\partial^4 w}{\partial y^2\,\partial z^2} + \frac{\partial w^4}{\partial z^4} = -\frac{\rho}{D}\frac{\partial w^2}{\partial z^2} \tag{24}$$

where w is the displacement function that is assumed to follow a sinusoidal path of buckling, which is predetermined based on experience and experimental analysis. The displacement function is a function of y and z. p is the applied pressure on the width of

the unit cell, D is the flexural stiffness of the walls. This flexural stiffness is assumed to be that of a plate, which was described by Equation (25) as $D = Et^3/12(1-v_s^2)$. Applying this approach to a commercial honeycomb requires making several assumptions [49]. The upper and lower cell walls are assumed to be simply supported, the joint between the unit cells remains straight during initial elastic buckling, and the function of the adjacent walls is to carry loads in addition to the load that is carried by the main cell walls. Finally, the inclined walls with a thickness t, are assumed to maintain the same loading capacity until the collapse of the thicker $2t$ vertical walls. The displacement function in which the cell walls buckle is assumed to follow the sinusoidal function in Equation (25)

$$w = f(y)sin\frac{mnz}{b} \tag{25}$$

the ODE defined earlier can be solved to obtain Equation (26)

$$\sigma_z = \frac{hP_{crit}+2lP'_{crit}}{2l(h+lsin\theta)cos\theta} \tag{26}$$

where P_{crit} is the elastic buckling load for the vertical cell walls and P'_{crit} is the elastic buckling load for the inclined cell walls.

2.1.4.2 Plastic yielding

If the applied loads are higher than that of the yield stress of the solid σ_{ys}, then the structural core would fail by axial yielding rather than buckling. According to Gibson and Ashby plastic collapse formulation [1], in out-of-plane compression, metallic honeycombs tend to buckle plastically. Figure 8 shows the deformation shape of a honeycomb unit cell prior to buckling.

From Figure 8, it is evident that there are folds that occur while the unit cell is being compressed, and as the load gradually increases, the number of folds increases [50]. To approximate the plastic collapse stress, the cell walls are assumed to have the folding behavior illustrated in Figure 8, and the stress is calculated for a single cell wall. As the cell walls are compressed in the out-of-plane direction, the cell walls tend to buckle, forming a plastic hinge similar to that in the in-plane direction.

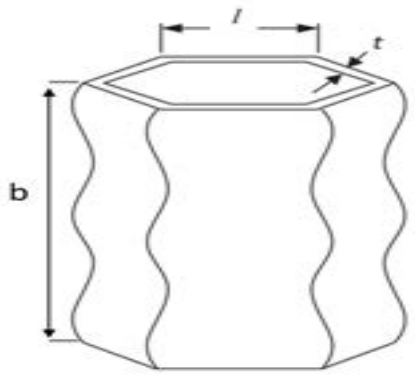

Figure 8: Plastic buckling of honeycomb unit-cell [51]

Figure 9 is an illustration of how one cell wall progresses from no buckling to forming the plastic hinge. Finally, the cell wall rotates around the plastic hinge and becomes fully folded [1]. As the load P is applied on the cell wall, it buckles and forms a plastic hinge.

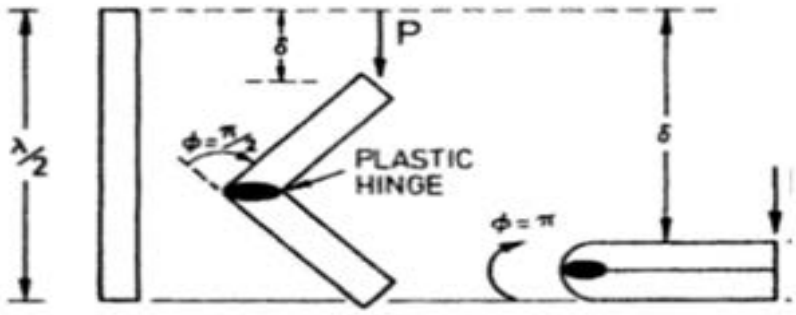

Figure 9: Schematic showing the buckling and folding effect in the out-of-plane direction [1]

The internal and external work calculations are made to calculate approximately the out-of-plane plastic collapse stress. $\lambda/2$ resembles half a wavelength of folding, so when a cell wall completely collapses, a full sine wavelength collapse is assumed. The folding angle, as illustrated in Figure 9, goes up to 180 degrees when it is fully folded. The plastic moment M_p is considered to have the same value that it had previously in the in-plane calculations Equation (15). However, instead of multiplying by b, the depth of the honeycomb unit cell, it is now multiplied by the length of the cell wall that is associated with one cell.

$$M_p = \frac{\sigma_{ys} t^2}{4}(2l + h) \tag{27}$$

This is because the depth of Figure 9 is the length of the cell wall rather than the z-direction depth. The internal and external work done on the cell wall are set equal, and the equation is solved to determine σ_{zp}, which is the plastic collapse stress in the z-direction. The internal plastic work done by the moment is

$$W_{int} = M_p \pi \tag{28}$$

And the external work done i by the external forces that are applied P so,

$$W_{ext} = \frac{P\lambda}{2} \tag{29}$$

where λ is half the wavelength of buckling, Converting the applied force in terms of σ_{zp}, the applied force is multiplied by the area on which the force is applied $P = \sigma_{zp}(h + lsin\theta)(2lcos\theta)$

$$\sigma_{zp} = \frac{\pi}{4}\sigma_{ys}(t/l)^2 \frac{h/l+2}{(h/l+sin\theta)cos\theta} \tag{30}$$

The derived plastic collapse stress in the out-of-plane direction is documented by Ashby and Gibson [1]. The plastic collapse stress is also dependent on the relative density, which is similar to all of the mechanical properties that were discussed. Following the same procedure, the mechanical properties in the in-plane and out-of-plane directions can be calculated for various cell shapes, and all the mechanical properties would still be dependent on the relative density where the difference would lie in the geometrical features as it could differ from a honeycomb unit-cell to other shapes. For random open-cell and closed-cell foams, the geometrical features would be difficult to consider in such calculations. Instead, geometrical constants are often used to approximate the mechanical or thermal properties of foams.

2.2 Thermal Properties

Cellular solids with low relative densities, such as foams, are attractive materials for thermal applications due to their low thermal conductivity, high surface area to volume ratio, and good insulation properties. Some of the applications in which the use of foams is dominant are thermal insulation [51], acoustic insulation [52], packaging [53], heat exchangers [54], thermal energy storage [55], or fire-retardant applications [56]. They are used for insulation applications as the porous media is excellent in preserving heat transfer, which reduces the overall energy consumption and maintains

temperatures for certain applications. Similarly, for acoustic applications, porous media is able to absorb sound waves and noise pollution. The only material that exhibits lower thermal conductivity is aerogels [1]. The low thermal conductivity of foam structures arises from the high-volume fraction of gas within the pores, and gases have a low thermal conductivity. Adding on, the small cell size of the pores suppresses convection and radiation through absorption and reflection of thermal energy [1].

2.2.1 Steady state heat conduction

Steady-state conduction refers to a state in which the temperature remains constant with time, and the temperature gradient remains constant. It is crucial to study the steady-state conduction in foams as it fits the criteria for thermal applications. The transfer of heat in building material, or packaging applications, remains constant, and thus, the study of the steady state conduction in foams is important. Fourier's law is a fundamental principle in the study of heat transfer. It states that the rate of heat transfer through a material is directly proportional to the temperature gradient, the change in temperature with respect to distance, and the cross-sectional area of the material. The Fourier's heat transfer equation can be expressed as

$$q = -\lambda \nabla T \tag{31}$$

Where q is the heat flux, λ is the thermal conductivity, and ∇T is the temperature gradient in all three directions. This can be written in 1D as,

$$q = -\lambda \frac{\partial T}{\partial x} \tag{32}$$

where x is the distance at which the heat flux is flowing. In the context of cellular materials, such as open-cell foams, the study of steady-state thermal conduction is highly significant. The unique morphology of a Voronoi structure, which includes a high surface area to volume ratio as well as interconnected porosity, allows for tailoring the structure through parametric optimization to enhance the thermal properties. The metallic foam matrix, which is an interconnected web of cell walls, facilitates efficient heat conduction due to the high thermal conductivity of metal. In addition, the porous structure allows for the impregnation of various filling mediums, such as air, water, oil, or paraffin, each of which can affect the overall thermal conductivity of the foam.

The interconnected pores provide a pathway for the heat to be transferred through both the solid and the fluid phases of the structure, which results in a combined conductive behavior that can be tailored for specific industrial applications. Understanding the steady-state conduction in these materials aids in optimizing their design for applications such as heat exchangers, energy storage, or thermal management devices. The application of Fourier's law, described in Equation (31), allows for the prediction of heat transfer and aids in the development of advanced materials.

Furthermore, the topological features of a cellular structure, such as the relative density and cell size, significantly influence the thermal conductivity. Understanding the influence of topological features on thermal conductivity under steady-state conditions enables the development of analytical models that can predict thermal conductivity based on factors like relative density and cell size.

2.2.2 Unsteady heat conduction

If the temperature varies over time, then the heat conduction is a nonsteady state. Diffusivity becomes an important parameter to study in foam structures as it describes the rate at which heat energy is transferred through a material due to thermal diffusion. In unsteady state heat conduction, the temperature changes with respect to time, and so does the temperature gradient. Diffusivity is a material property that describes how quickly heat is conducted through a material as a function of time, which is related to the thermal conductivity, heat capacity, and density of the material. A material with high diffusivity will conduct more heat in a shorter time span than that of low diffusivity. In certain applications of heat transfer, such as heat exchangers, electronic devices, or any thermal management systems, it is important to understand how quickly heat is conducted through a material over time. The relationship between temperature, time, heat flow direction, and diffusivity is given as

$$\frac{\partial T}{\partial t} = \alpha \frac{\partial^2 T}{\partial x^2} \tag{33}$$

where T is the temperature, t is the time, and α is the diffusivity, which can be directly related to the thermal conductivity and heat capacity of the constituent material of the solid by:

$$\alpha = \frac{\lambda}{\rho C_p} \tag{34}$$

where C_p is the specific heat capacity of the material, and when the heat capacity is multiplied by the density, it represents the volumetric heat capacity. The heat capacity can be defined as the heat energy that is required to raise the temperature of a unit volume of the material by one degree. There are several factors to consider when calculating the thermal conductivity of a foam structure. Such considerations include conduction through the solid λ_s, conduction through the gas λ_g, convection within the cells λ_s, and heat transfer through radiation λ_r [1].Therefore, the final thermal conductivity of a foam structure, or any cellular structure, can be calculated as

$$\lambda = \lambda_s + \lambda_g + \lambda_c + \lambda_\mathrm{r} \tag{35}$$

where the thermal conductivity of the foam is λ, and it is the sum of all the contributions. The conduction through the solid is dependent on the relative density of the foam structure as well as the tortuosity, which can be expressed as

$$\lambda_s = \eta(\rho^*/\rho) \tag{36}$$

where η is an efficiency factor that is dependent on the tortuosity of the foam structure. Tortuosity refers to the degree of curvature or twisting in a path or channel and (ρ^*/ρ) is the relative density of the cellular material. It can be quantified as the ratio of the actual length of the pathway to the straight-line distance between the endpoints of the pathway. This ratio is often referred to as the tortuosity factor or the tortuosity index. Similarly, the conduction through the gas in foams can be expressed as

$$\lambda_g = \lambda_g(1 - \rho^*/\rho) \tag{37}$$

where λ_g is the conductivity of the gas and $(1 - \rho^*/\rho)$ is the volume of the gas or the porosity of the sample. Most of the contribution to the thermal conductivity of the foam is dependent on the conduction through gas. Thus, the relative density is a crucial factor in determining the needed thermal conductivity for specific applications.

2.3 Tailoring Thermal and Mechanical Properties of Cellular Solids

The thermal and mechanical properties of cellular solids can be enhanced in several ways. Based on Section 2.1 and Section 2.2, different factors affect the

properties, with the dominant factor being the relative density. In this section, three different approaches will be discussed to enhance the mechanical and thermal properties of cellular solids: Tailoring the topological features of the cell shape, adding lightweight filler material in the voids of the cells, and applying different coating materials for various cell shapes and relative densities.

2.3.1 Coating of cellular solids

Various factors influence the resulting properties of open-cell foams, including the constituent material, relative density, strut thickness, and pore size. This allows for a wide range of properties that can be optimized and tailored to specific engineering applications. Two main approaches have been used to realize metallic open-cell foams with improved or tailored properties. The first approach used constituent materials with higher specific properties (e.g., stiffness, strength, and thermal conductivity). This approach required developing manufacturing technologies capable of creating open-cell metallic foams with controlled porosities from a wide range of materials (e.g., aluminum [57], copper [58], titanium [59], and magnesium [60]).

Accordingly, multiple manufacturing approaches were developed (e.g., casting, powder metallurgy) [1], [61], [62]. However, for metallic foams, casting became the most prominent and delivered, compared to cost, the best properties. The second approach, which was motivated by the advent of finite element and computer-aided design tools as well as computer-assisted tomography, explored the potential for tuning the properties of metallic open-cell foams by tuning their topological and morphological features. Thus, effects of cell size and its distribution [63], [64], [65], [66], cell irregularities [67], [68], ligaments geometry [69] and defects [70], [71] on the structural properties (e.g., stiffness [63], [72], yield strength [73], [74], densification strain [75], strain rate sensitivity [67], [76], and toughness [77]) and thermal properties (e.g., thermal conductivity [78]) of open-cell foams were investigated. These efforts showed that the optimal structural and thermal specific properties of metallic open-cell foams are achieved by minimizing open-cell foams' structural (i.e., topology and morphology) heterogeneities and defects, motivating establishing better control on their fabrication processes (e.g., controlling the distribution and growth of the gaseous phase introduced during casting [1]). The aforementioned two approaches were, in general, focused on the objective of increasing their specific stiffness, strength, and toughness

as well as the thermal conductivity of open-cell foams. However, despite the relative success in developing open-cell foams with improved structural and thermal properties, the approaches had limitations, as they produced foams whose properties were inherently dependent on their constituent materials.

This limited the range of foam properties that can be achieved and hindered the potential for realizing tuned or application-tailored properties. In addition, enhancing metallic foams properties through reducing heterogeneities and defects is limited by an upper bound (i.e., when a defect-free and uniformly distributed open-cell foam structure is realized). Recently, a different approach to enhance and tune the properties of metallic open-cell foams has been proposed. In this approach, which draws on the established history of tailoring materials' properties using coatings, thin metallic coatings (e.g., copper and nickel) are electrodeposited on metallic open-cell foams to reinforce them and improve their structural and thermal properties.

For instance, Ni-W was electrodeposited on aluminum foams to increase their specific strength and energy absorption capacity [79]. Similarly, Cu [80], [81], [82] and Ni [82], [83] were electrodeposited on aluminum foams to increase their strength, plateau stress, and impact energy mitigation capacity. Improved strength and energy absorption capacity of the coated foams are related to an increase in their ligaments' flexural stiffness and flexural load-carrying capacity [84]. Coating metallic open-cell foams to produce hybrid foams has substantial advantages and potential. First, it is relatively simple as it is based on electrodeposition, which is a well-known and straightforward process. Second, it is a cost-effective approach to tailor metallic open-cell foams properties since it allows for augmenting the properties of commercially available open-cell foams with additional functionality (i.e., coating properties). For instance, depositing nickel coatings on open-cell aluminum foams allows them to exhibit better corrosion resistance, higher hardness, ferromagnetic abilities, and catalytic properties [79]. These properties are not readily deliverable by aluminum foams.

Accordingly, coating metallic open-cell foams allows for realizing a wide range of application-tailored properties that cannot be delivered by a foam made from a single metallic constituent. According to the pioneering efforts that experimentally developed hybrid metallic open-cell foams, both coating material and coating thickness play

instrumental roles in determining the overall properties of hybrid foams [79]. However, the thickness effect and its interaction with porosity levels, though known as important, is not well investigated. Most experimental efforts utilized few thickness values in their experimental work and did not systematically investigate the thickness effect over a wide range of foam porosities. In addition, correlations relating coating properties and thickness to the macroscopic properties of hybrid foams of different porosities are lacking.

These correlations are needed to facilitate designing hybrid foams, particularly as they would allow for determining the coating thickness and porosity required to provide a desired property. Subsequently, the required thickness can be obtained by controlling the current and bath time during the electrodeposition process. Few applications have already started to utilize open-cell foams in a multifunctional capacity (i.e., utilizing their structural and thermal properties simultaneously). Examples of the latter include micro-heat exchangers [85] and thermal management solutions in lithium-ion battery packs [86].

Tunable properties of metallic foams represent a crucial feature of their applicability across various engineering domains, where customized materials tailored for specific applications are desired to meet performance criteria. The relative density of the structure, defined as the ratio of the foam's density to the density of the solid material, is a primary determinant of its mechanical strength and stiffness. Stochastic foams' morphological features that directly influence their relative density include cell shape [69], size [66], and cell wall thickness [87]. Apart from tuning stochastic foams by altering their relative density, recent efforts have been made through the application of coating through different techniques (i.e., electrodeposition [82], PVD [88], CVD [89]). Coating metallic foams has been deemed effective due to the high surface area to volume ratio within low relative density foams [90]. A minimal quantity of coating can cover a larger area, ensuring enhanced mechanical performance without the need for excessive material. This efficiency not only reduces material costs but also minimizes the additional weight associated with coating, maintaining the lightweight characteristic of the foam. In recent efforts, nickel-coated aluminum foam was tested under static and dynamic compressive loadings, where the energy absorption was found to increase by a factor of 9 under quasi-static loading and 4.5 under dynamic loading [91].

Similarly, authors have tested different coating materials, such as the combination of Nickel and Copper on aluminum foam, and found that they led to enhanced stiffness, yield strength, and energy absorption capabilities [82]. The use of Finite Element Analysis (FEA) is dominant in this field, as tuning morphological and topological features of cellular cores can be achieved with the aid of Computer Aided Design (CAD) [92] and Computer Assisted Tomography [93]. To further enhance energy absorption capabilities effectively, researchers have focused on developing functionally graded coatings on metallic foams. Functionally graded nickel-coated aluminum foam was developed using electrodeposition. It exhibited diverse compressive stress-strain responses [94]. Specifically, the functionally graded samples showed promising capability to absorb energy at a wide range of impact velocities [94].

Electrodeposition constitutes the dominant foam coating technique in the industry. Its cost-effectiveness, ease of scalability, and tuning made it favored by the industry. In complex porous geometries, it is easy to manipulate the electrodeposition parameters to achieve varying coating thicknesses and gradients. In a recent study by Shajari et al. [95], the authors have investigated the effect of heat treatment on the macrostructure, microstructure, and mechanical properties of nickel-coated open-cell silver foams that were produced by electrodeposition. The samples were subjected to a heat treatment at 410°C for one hour in an argon atmosphere. The mechanical properties of the foam were evaluated by uniaxial compression testing, while its microstructure and morphological features were assessed using Scanning Electron Microscopy (SEM). The samples were subjected to a direct current of 1.7A for various electrodeposition times, namely 4,6,8,10, and 12 hours. The electrodeposition process resulted in a homogeneous microstructure, where large conglomerates were formed at nodes due to flow leakage, and higher deposition time resulted in thicker nickel layers with improved coating uniformity. The heat treatment enhanced the mechanical properties, specifically the yield strength, which increased from 1.03MPa to 1.76MPa. The plateau stress was also enhanced, and the energy absorption increased from 0.91 mJ/mm^3 to 3.45 mJ/mm^3.

In different electrodeposition studies, researchers have produced a range of coating thicknesses by changing the electroplating setup, acidic concentration, deposition time, induced voltage, and current. In one of the recent studies, Grill et al. [96] studied the factors that affected the homogeneity of the coating with electrodeposition and developed a model that can predict the optimal process

parameters for coating open cell foams. A full factorial design of experiments was used to study the influence of the electrodeposition parameters on the coating thickness homogeneity. The Nernst-Planck equation, which includes convection, diffusion, migration, and reaction terms, was used to model the electrodeposition process. The findings of the study, from an experimental perspective, showed that the coating thickness varies across the foam and that higher densities and velocities led to less uniform coatings. The simulation results overestimated the coating homogeneity for high coating rates and high current densities. The current density and duty cycle had the highest effects on the coating thickness homogeneity.

Additional studies have focused on improving or optimizing the electrodeposition of foams. For instance, in a study by Sengupta et al. [97], the authors focused on optimizing the electrodeposition process through the dynamic hydrogen bubble template method. The setup used attempted to coat nickel foams with copper using baths comprising different compositions and varying concentrations of $NiCl_2$ and $NiSO_4$. The effect of pH was studied for a variety of ranges from 1 to 7, in which both chloride and sulfate baths were used. Additionally, the applied voltage varied from 3 to 9V, and the deposition time ranged from 2 to 600 s. This electrodeposition time is relatively low compared to other studies. SEM and XRD analysis were employed to assess the coating quality, as well as the morphological features of the deposits, crystal structure, and residual stress evolution over time. The results showed that the optimal bath composition to achieve uniform honeycomb-like structures with regular-sized pores was 0.1M $NiCl_2$ and 1M of NH_4Cl.

The higher concentrations resulted in planar deposits without distinct pore formation. The initial deposits showed compact films with no pores, which were evaluated between 2 and 10 seconds. At 30 seconds, the isolated pores began to appear, and between minutes 1 and 3, the honeycomb structures started forming due to pore coalescence. The uniformity of the coating was achieved at minute 5, which the authors noted as the critical time for structural development; higher deposition times resulted in the formation of larger pores, which is mainly due to hydrogen bubble coalescence.

As for the applied voltage effects, the authors noted that at low voltages (3V to 5V), planar or dendritic nickel networks have formed, and the pore formation began at 6V. To achieve honeycomb structure deposits, the authors concluded that high voltages,

specifically between 7V and 9V, are optimal. A notable difference was present when the bath solution varied between chloride and sulfate. The planar depositions occurred at pH 1 in the chloride baths, and at higher concentrations (pH 2 to 6), the pore diameter increased. While the sulfate bath had similar trends, the overall pore size was smaller at higher concentrations.

2.3.2 Tailoring topology in cell shapes

Tailoring the topology of cell shapes of cellular solids has been motivated mainly by realizing better-performing sandwich structures. Cellular solids are often used as cores in sandwich structures due to their high stiffness and strength-to-weight ratios as well as their ability to mitigate impact energy. A composite sandwich panel structure is comprised of two parallel, thin, stiff sheets that are adhesively bonded, often using epoxy [13], silicon [98], or polyurethane [99], to a lightweight cellular core in the middle. The cellular core increases the second moment of inertia of the sandwich structure without compromising its weight. The two thin sheets carry tensile or compressive loads, whereas the core carries transverse shear loads. The high energy absorption of a sandwich panel is a result of the highly nonlinear plastic deformation that occurs when the cell walls of the core collapse progressively under compressive or impact loadings. Tailoring such mechanical properties to specific engineering applications has attracted the efforts of researchers [100].

Numerous studies were initially conducted to understand the deformation mechanisms and mechanical response due to dynamic loading on cellular sandwich panels. Li et al. [101] studied the deformation mechanisms and debonding effects of blast impact on aluminum honeycomb sandwich panels by experimental and numerical methods. Hou et al. [102] focused on understanding inertia effects on aluminum honeycomb sandwich panels under impact loadings. Asprone et al. [103] utilized FEA to simulate the buckling behavior and characteristics of aluminum honeycombs.

Optimizing the design of cellular sandwich panels is highly dependent on developing cellular solids with higher stiffness and strength-to-weight ratios and a higher ability to mitigate impact energy. Some efforts focused on using high-performance composite sheets and core constituent materials [104], [105]. Other efforts emphasized improving cores' properties by modifying their relative density, cell size, wall thickness, or cell shape. Safarabadi et al. [105] studied the effect of foam-filling

Nomex honeycombs with glass-epoxy face sheets on the buckling strength and energy absorption of the material. This study was conducted with the aid of FEA and investigated the elastic and viscoelastic material behavior. Similarly, topological features were altered to achieve higher buckling strength in honeycombs. For instance, Miller et al. [106] conducted experimental and numerical compression tests on hexa-chiral and tetra-chiral honeycombs. Zhong et al. [107] investigated the global and local response in a hybrid honeycomb in which cell shapes varied within the sandwich panel. Tailoring the cell shapes significantly enhanced the buckling strength of the sandwich panels.

Chapter 3: Research Significance and Literature Gaps

Multiple techniques have been used to enhance the mechanical and thermal properties of cellular solids. Each of these techniques has limitations. This work aims to address these limitations. The most commonly used technique to enhance or tune the properties of cellular solids is to modify their topology. Topological modification of cellular solid unit cells has been shown to be effective in enhancing these properties. However, the viability and manufacturability of proposed unit cells are often constrained by costly manufacturing methods such as additive manufacturing. To overcome this challenge, this work investigates the potential for improving the mechanical properties of cellular solids by imposing sinusoidal perturbation on them. These perturbations are designed to be compatible with cellular solids' conventional manufacturing methods. Thus, the introduced perturbations would not require the use of expensive additive manufacturing techniques. The approach is applied to honeycomb structures, which are commercially available and widely used in the aerospace industry.

Adding metallic coatings to cellular solids to form hybrid foam composites is another technique that was utilized to create hybrid foams with tailored mechanical and thermal properties. However, all efforts in this regard have been experimentally or numerically driven. So far, analytical models that can relate the hybrid coated foam properties to the properties of their constituent materials, porosity, and thickness of the coating have not been developed. These models are necessary to assist designers and engineers in developing customized coated foams to meet the needs of pre-determined applications and properties. This work aims to develop analytical models that can accurately predict the structural and thermal properties of coated cellular solids.

Chapter 4: Research Questions and Objectives

The main objectives of this dissertation are:

1. Enhance the mechanical and thermal properties of cellular solids by modifying their topological features through superposing periodic sinusoidal patterns.
2. Develop hybrid coated cellular foams with tailored and enhanced mechanical and thermal properties.
3. Develop analytical models capable of predicting the mechanical and thermal properties of hybrid coated cellular foams.

Based on the set research questions, this dissertation is divided into three different sections that aim to tailor the mechanical and thermal properties by imposing sinusoidal periodic patterns and applying metallic coatings.

Chapter 5: Workplan

The first research objective is achieved by conducting the following tasks:

1. Develop an automated algorithm to impose sinusoidal perturbations on the cell walls of honeycombs.
2. Investigate the effect of sinusoidal perturbations on the buckling and post-buckling behavior of perturbed honeycombs.
3. Investigate the effect of sinusoidal perturbations on the in-plane and out-of-plane behavior of perturbed honeycombs.
4. Conduct parametric studies to find the optimum sinusoidal frequency and amplitude.
5. Develop analytical models to approximate the in-plane and out-of-plane mechanical properties.

The second and third objectives are achieved by conducting the following tasks:

1. Develop CAD models of foam structures utilizing Voronoi Tessellations with controlled cell wall thickness, relative density, and pore size.
2. Develop finite element models of the CAD models using ABAQUS software. The finite element models are used to investigate the structural and thermal responses of the coated foams.
3. Verify the numerical results using experiments in which electrodeposition is used to coat aluminum foams and honeycombs.
4. Develop an analytical model based on the obtained results to create a generalized model for metallic coatings for cellular solids.

Chapter 6: Methodology

6.1 Altering Topological Features of Honeycombs by Introducing Sinusoidal Perturbations

6.1.1 Core geometry and properties of superposed perturbations

To increase sandwich structures' resilience to low-velocity impacts, this work aims to improve their honeycomb cores' resistance to damage under out-of-plane loads by superposing periodic sinusoidal perturbations on their cell walls. The periodic perturbations applied are illustrated in Figure 10.

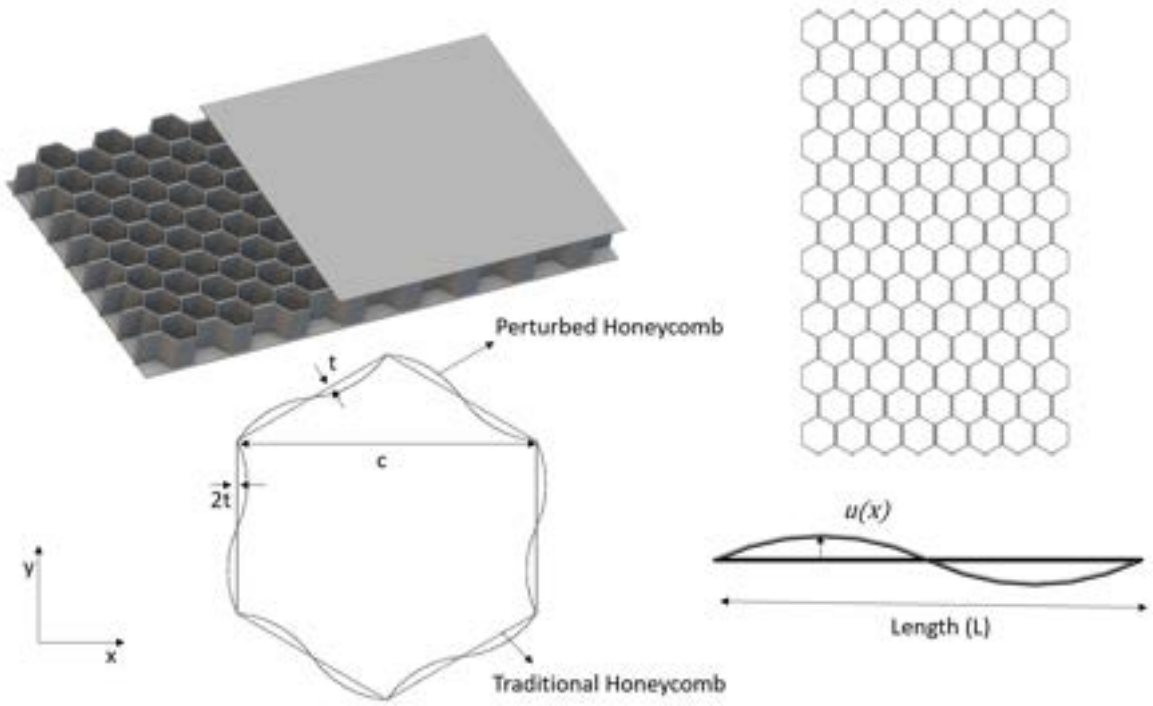

Figure 10: Schematics of a sandwich structure with a honeycomb core, showing the core geometry before and after the superposition of the periodic sinusoidal perturbations

These perturbations were proposed to tailor honeycomb cores' acoustic properties [108], [109]. However, they are used here to increase cell walls' second moment of inertia and, in turn, their resistance to buckling or bending failure under out-of-plane loads. The superposed perturbations satisfy two constraints: they do not substantially increase the walls' lengths or relocate the walls' intersections (vertices) of the parent core. The first constraint prevents increasing the core mass substantially, and the second keeps the modified cores compatible with the simple manufacturing methods used to

create honeycomb cores (e.g., corrugation and bonding techniques [110]). The superposed sinusoidal perturbations are governed by

$$u(x) = \mathrm{A}\, sin\left(\frac{n\pi x}{L}\right) \tag{38}$$

where A is the amplitude, n is the number of waves per cell wall, and L is the cell wall length. Perturbations are superposed on each wall by applying the displacement function $u(x)$, as seen in Figure 10. The direction of $u(x)$ is perpendicular to the longitudinal direction of the wall. The modified shape of the wall is governed by the amplitude (A) and frequency (n). Figure 11 shows the cell walls after superposing a perturbation with a frequency of one wave per wall. The amplitude and frequency parameters are varied in this work to investigate their effect. The amplitudes used are 0.15, 0.2, 0.25, and 0.3 mm, and the frequencies used are 1, 2, 3 and 4 waves per wall.

The different amplitudes and frequencies result in 16 cases. The cross-sectional geometries of these cases are shown in Figure 11. The vertically aligned walls have double the thickness of the inclined ones, as the parent honeycomb core (i.e., perturbations are superposed on) is assumed to be made by corrugation and bonding techniques. The parent honeycomb is a conventional aluminum honeycomb core.

Its cell wall length, thickness, and out-of-plane height are 5.285 mm, 0.1 mm, and 15 mm, respectively. The superposed perturbations do not affect cell wall thickness and out-of-plane height but increase cell wall length moderately. The effect of perturbations on cell wall length is presented in Table 1.

The highest increase in length is 11.8% and is associated with the highest perturbation frequency and amplitude values used. However, for all the cases, except at (A=0.3, n=4), (A=0.25, n=4), and (A=0.25, n=3), the increase in cell wall length is less than 6%, which is ignorable. Tracking the effect of the superposed perturbations on cell wall length is important, as it affects the core's relative density. Since the superposed perturbations are periodic and do not affect the location of the parent core's vertices, the relative density of the perturbed cores is directionally proportional to their cell wall length. For instance, increasing the cell wall length by 10% increases the relative density by 10%.

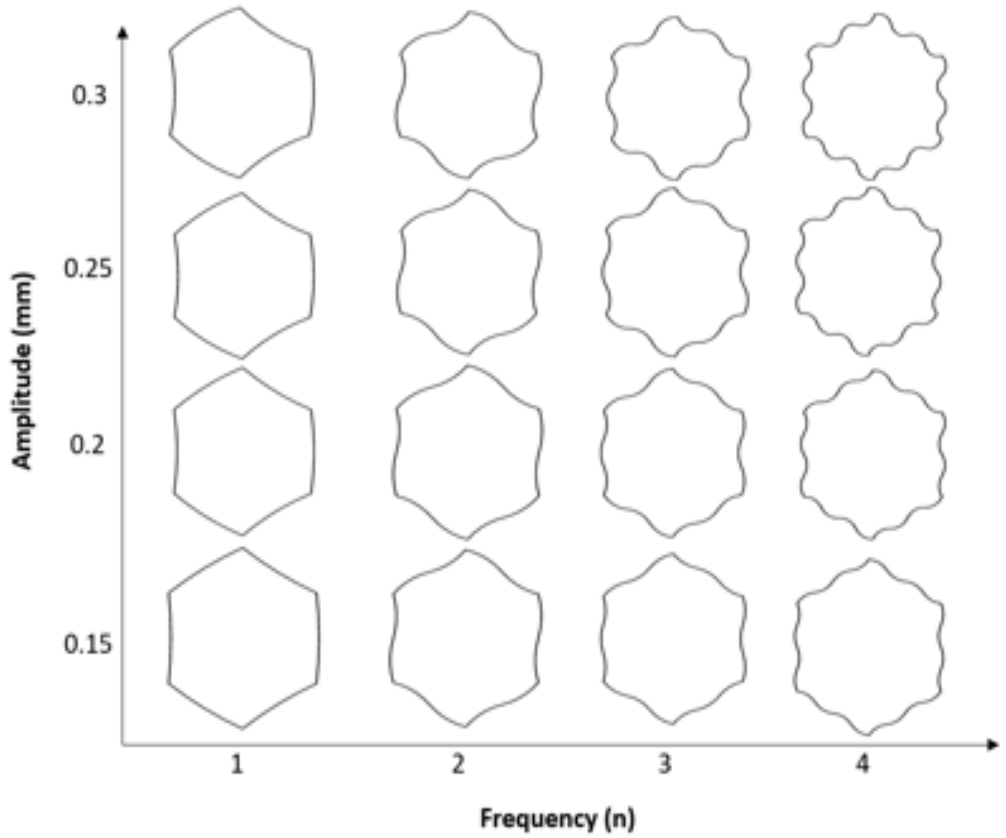

Figure 11: Cross-section geometry of the perturbed honeycomb cores, showing the effect of perturbation amplitude and frequency

Table 1: Length of the perturbed cell wall as a function of frequency and amplitude

	Cell wall length (mm)			
Frequency (n)	**A=0.15**	**A=0.2**	**A=0.25**	**A=0.3**
1	5.296	5.304	5.315	5.328
2	5.327	5.356	5.400	5.450
3	5.379	5.450	5.539	5.645
4	5.450	5.572	5.725	5.904

The perturbations introduced to the traditional honeycomb struts cause an increase in the relative density of the unit cell. For a regular honeycomb with double thickness on vertical walls, equal horizontal and inclined struts with $\theta = 30$, the relative density is [111],

$$\frac{\rho^*}{\rho_s} = \frac{t}{l}\frac{8}{3\sqrt{3}} \tag{39}$$

The goal is to estimate the relative density of a perturbed honeycomb, considering the geometrical parameters, frequency, and amplitude. The arclength method is employed initially to approximate the perturbed lengths, considering different frequencies and amplitudes. The final perturbed length is expressed as,

$$l_p = n(0.0948 + 1(l/n) + 0.2068a) \tag{40}$$

Using this perturbed length, the relative density of the perturbed honeycombs, for $h = l$ and $\theta = 30$, can be calculated to be,

$$\frac{\rho^*}{\rho_s} = \left(\frac{t}{l}\right)\left[0.146\left(\frac{n}{l}\right) + 0.318\left(\frac{an}{l}\right) + \frac{8}{3\sqrt{3}}\right] \tag{41}$$

In the absence of any perturbations on the honeycomb ($n = 0, a = 0$), the relative density simplifies to the previously derived relative density of double-thickness honeycombs, as represented in Equation (38). Figure 12 shows the exact relative densities derived from the CAD models of the perturbed honeycombs against the approximated relative density shown in Equation (38).

The differences between the estimated relative densities and the exact relative density are due to errors that occurred during the approximations of the sinusoidal curves. These curves were calculated using the arc length method, with the highest reported relative error being 3.64. As illustrated in Figure 12, the relative density demonstrates an upward trend as both the amplitude and frequency increase. However, the increase in frequency has a more significant impact on the relative density compared to the amplitude. The largest observed rise in relative density is 0.39%, which corresponds to a substantial 13.21% increase relative to the initial value.

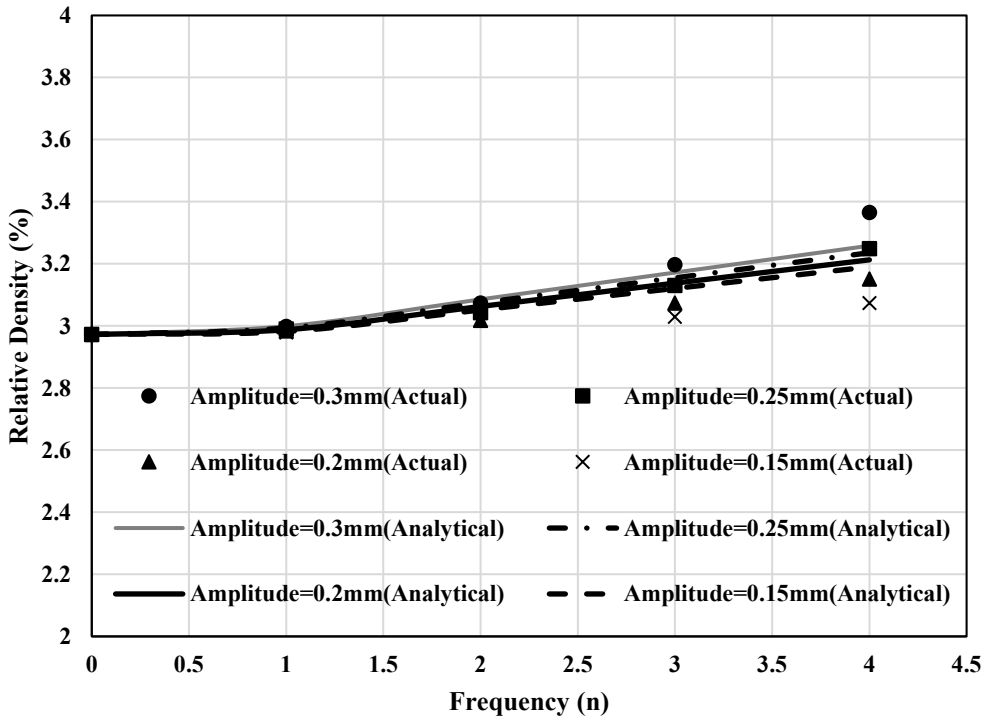

Figure 12: Relative density as a function of frequency and amplitude

6.1.2 Uniaxial in-plane and out-of-plane compression

When a sandwich structure is subjected to low-velocity impact, its core is subjected to localized out-of-plane forces transmitted through its composite sheets. The location and size of the core area subjected to localized forces can vary significantly depending on the impacting subject size, location of impact, and properties of the composite sheet. Moreover, the number of cell walls sharing the localized load could vary considerably depending on the site and size of the impact area. To overcome the randomness associated with the localized loadings generated by low-velocity impact, four loading scenarios are considered. These scenarios are not exhaustive of all possible loading scenarios but give insights into out-of-plane loadings resulting from impact with objects of different sizes. The four out-of-plane loadings loading scenarios are shown in Figure 13.

They represent very small (i.e., sub-cell) to moderate impact areas (i.e., multiple cells). The sub-cell category is represented by two scenarios: localized loading on one cell wall and three cell walls. The category with impacts spanning more than one cell is represented by two scenarios: localized loading on one cell and three entire cells. Enhancing honeycomb cores' out-of-plane strength under the four loading scenarios ensures improving their strength under all other localized loading scenarios.

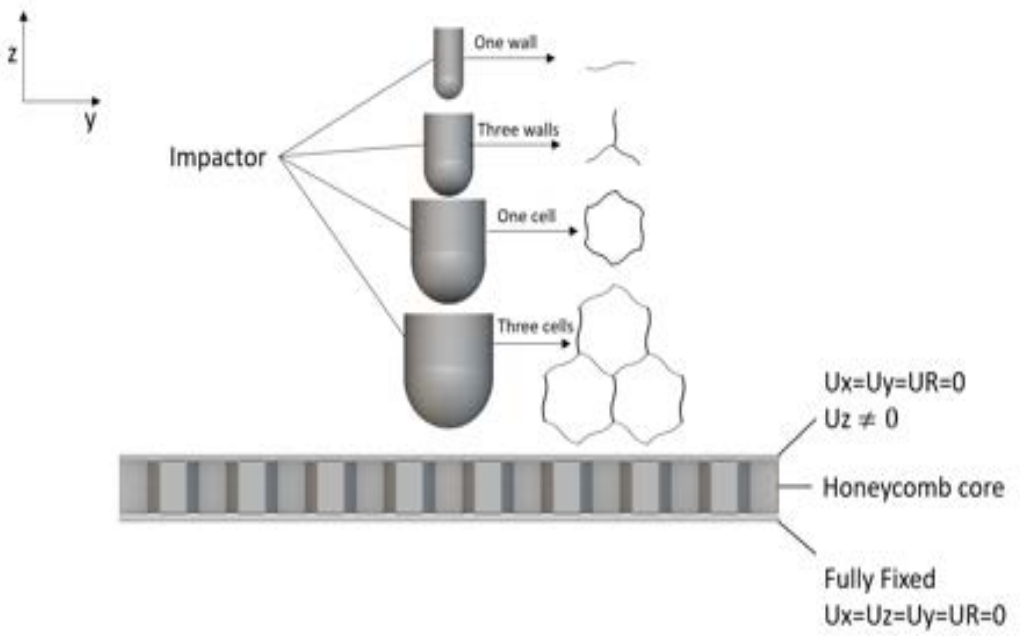

Figure 13: Impact scenarios analyzed, showing the portion of the core subjected to loading in each scenario

The finite element software ABAQUS is used to analyze the response of the perturbed honeycomb cores under the four localized loading scenarios. Riks solver is used as the cores are anticipated to fail due to elastic and plastic buckling modes. Riks solver allows capturing the post-buckling softening behavior and efficiently solves nonlinear problems. Finite element models representing the perturbed honeycomb cores have 8×8 cells. Their walls are discretized using 4 node shell elements with hourglass control and reduced integration (S4R). A finite element model is created for each of the 16 perturbed conditions and one model for the parent honeycomb. Accordingly, the four loading scenarios are applied to 17 models. The cell walls of the 17 honeycombs are assumed to be made from 6061-T6 aluminum alloy. The Johnson-Cook model was used to describe the behavior of the aluminum alloy. Table 2 presents the used Johnson-Cook model parameters [112], [113], [114].

Table 2: Johnson-Cook model parameters

Material	**ρ (kg/m3)**	**E(MPa)**	**μ**	**A(MPa)**	**B(MPa)**	**n**
Al6061-T6	2700	72,600	0.33	324.1	113.18	0.42

The models assume a sandwich structure configuration, and therefore, they limit the lateral motion of the cores' top and bottom edges. Accordingly, the translational and rotational degrees of freedom of the nodes at the cores' bottom edges are fixed. In addition, the translational, except along the impact direction, and rotational degrees of freedom of the nodes at the cores' top edges are fixed. A uniform distributed loading of 1 N.mm is applied on the top edges of the loaded cell walls. The boundary conditions are schematically represented in Figure 13. A linear buckling perturbation step is used before the Riks analysis step to determine the first 10 linear elastic eigenmodes. The 10 modes are superposed on the walls to represent small manufacturing-induced imperfections. These small imperfections are needed to trigger buckling. The modes are scaled by 0.1% to keep the imperfections very small. Subsequently, a Riks analysis step with ABAQUS's default settings is used to determine the cores nonlinear response. The two-step analysis, i.e., linear buckling followed by Riks, is widely used to analyze structures post-buckling or nonlinear collapse [115].

The effect of the superposed periodic perturbations on the in-plane compressive behavior is also assessed to ensure that they do not result in adverse effects. The in-plane behavior is investigated by subjecting a model comprising 8×8 perturbed honeycomb cells to a uniaxial compressive load, as seen in Figure 14. This particular number of cells is used as it results in cell size-independent behavior [92]. The core's top and bottom sides are coupled to rigid surfaces to eliminate localized deformation at the loaded boundaries [63]. The rigid surface on one side is fully fixed, and the opposite rigid surface is prescribed a compressive displacement. The translating side is allowed only to move along the y-direction shown in Figure 14. Cell geometry, material, and element type are identical to those used in the out-of-plane models. Nonlinear analysis is performed on the models to determine the in-plane force-displacement response of the perturbed cores.

Mesh sensitivity analysis is used to determine the element size needed to ensure mesh size independence. Analysis shows that the out-of-plane loading is the most sensitive to element size. An element size of 0.25 mm is found sufficient to ensure mesh size independence in the out-of-plane loading simulations. In comparison, an element size of 0.5 mm is found sufficient to ensure mesh size independence in the in-plane compressive loading simulations.

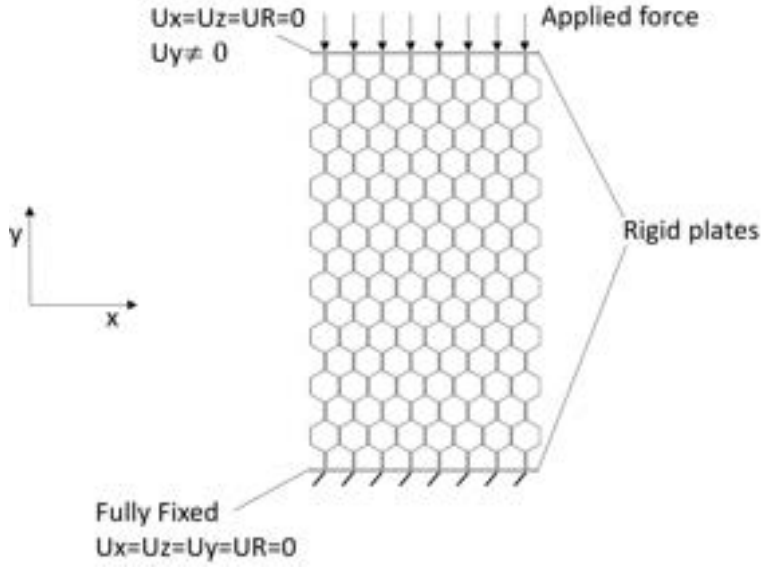

Figure 14: Schematics showing the in-plane compressive loading

6.1.3 Pure bending and transverse shear loading

FEA, with the aid of the commercially available finite element package ABAQUS Static General, was used to investigate the transverse shear and bending behavior of the modified honeycomb cores. The cores were modeled in a sandwich panel configuration. The model comprised a honeycomb core and two face sheets. The cores and the face sheets were made from the same constituent material, Aluminum 6061-T6 with a Young's Modulus of 72 GPa and Poisson's ratio of 0.33. The panels were discretized by linear quadrilateral 4-node double-curved thick shell elements with hourglass-control. A mesh sensitivity analysis was conducted to ensure the accuracy of the developed mesh. It showed that an element size of 0.22 mm is sufficient to realize mesh-size independence.

To analyze the effect of sinusoidal perturbations on the flexural response, an 8×8 sandwich panel was subjected to pure moment loads. A nonlinear static solver was used. The left side of the panel was fully fixed (i.e., not allowed to rotate or translate in all directions), whereas on the other end, the panel was subjected to rotation. The loading scheme is shown in Figure 15. A rigid wall is imposed on the sides of the panel where boundary conditions were imposed. The rigid wall prevents local deformation at the loaded edges.

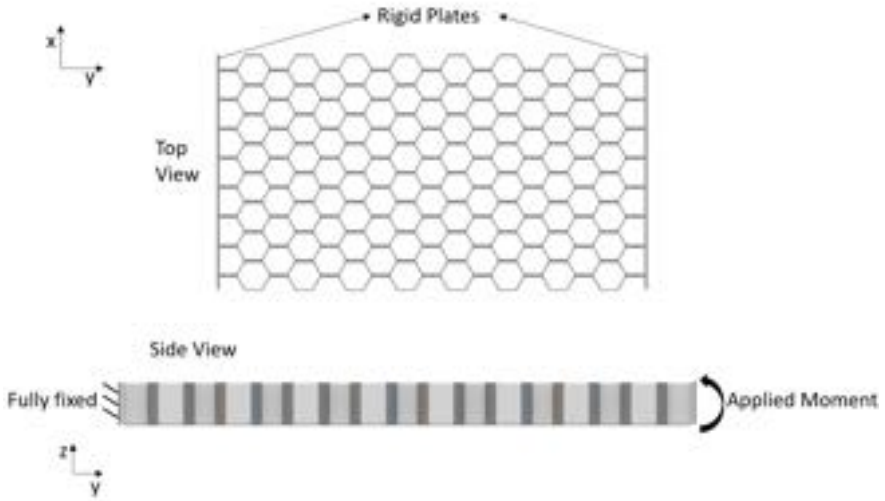

Figure 15: Boundary conditions applied to induce pure flexural loading

The objective of the aforementioned loading, pure bending, is to characterize the bending stiffness as a function of frequency and amplitude. The finite element software calculated the moment applied at the right end to induce the imposed rotation. The applied moment was plotted against the imposed rotation, and the resulting plot was used to calculate the flexural stiffness of the modified lattice.

To characterize the transverse shear response, a transverse displacement was applied on one end while the other end of the model was fully restrained. ABAQUS's nonlinear static solver was used to analyze the model. The side at which the transverse load is applied was restrained to move upward only. ABAQUS was used to compute the transverse force required to induce the imposed transverse displacement. The panel used in the model comprised 8×1 cells. A small number of cells is used across the load transfer direction to ensure that the loading mimics a short beam and to induce a loading scenario dominated by transverse stresses. The loading scenario is illustrated in Figure 16.

Two rigid plates were attached to the ends subjected to the transverse load boundary conditions. The plates minimize the localized deformation in the incomplete cells at the boundaries. The transverse force computed by ABAQUS and the transverse displacements imposed were plotted against each other and used to determine the transverse shear response of the perturbed lattices. In the simulations, 8 cells are used in flexure and transverse shear loading, as studies focusing on investigating the size

effects in cellular solids have shown that 8 cells are sufficient to represent the bulk behavior of honeycombs [92]. As a result, an 8×8 panel was chosen for the pure bending simulations and an 8×1 panel for the transverse shear simulations.

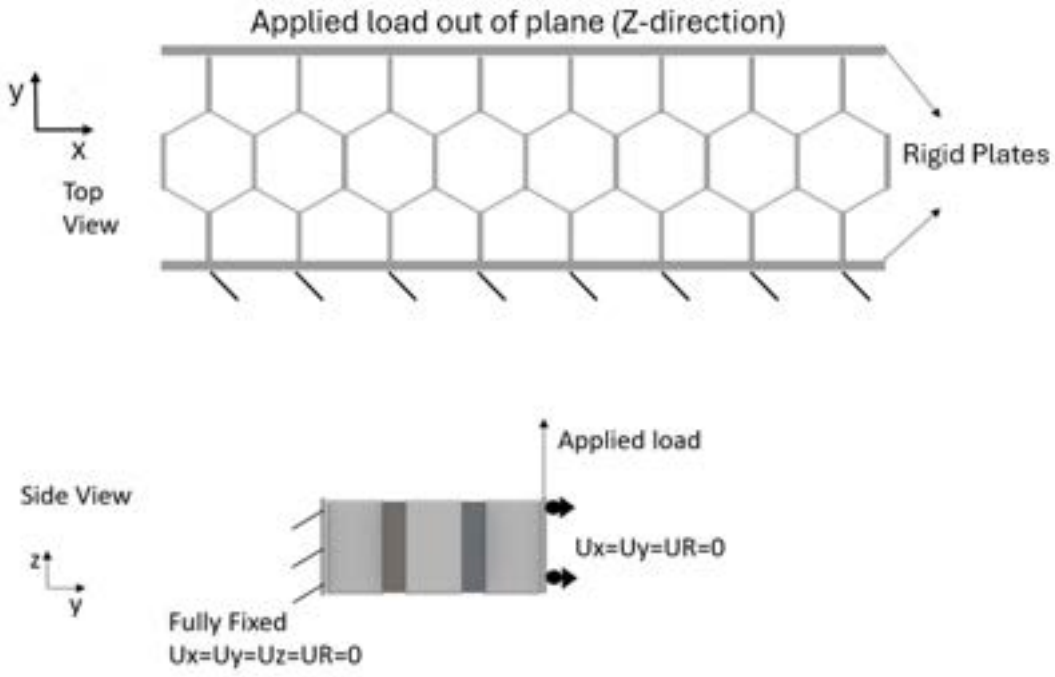

Figure 16: Transverse shear boundary loading conditions

6.1.4 Three-point bending

Numerical simulations utilized ABAQUS's explicit solver as it can automatically and effectively model the contacts between the rollers and the sandwich structure. To ensure convergence and reduce the computational cost, a finer mesh is applied at areas of contact and large deformation gradients. Based on mesh sensitivity analysis, it was determined that a 0.5 mm element size is required for areas subjected to impact or exhibiting large deformation gradients. In contrast, a 1mm element size is sufficient to model the rest of the beam. Four node shell elements (S4R) are used to model both the thin aluminum sheets and the walls of the honeycomb core. On the other hand, four-node rigid elements (R3D4) are used to model the rollers.

Although the sandwich structures' sheets and honeycomb core are assumed to be made from the same aluminum alloy, experimental evidence shows that they might exhibit different mechanical properties [116]. The latter relates to the different

manufacturing technologies used to fabricate each of them. An experimental assessment of a sandwich structure whose sheets and traditional honeycomb core are made from AL5052 showed a difference between the properties exhibited by the sheets and those of the core [116]. Table 3 shows the material properties in which the sheets exhibited an elastic-perfect plastic response. On the other hand, the core material exhibited a hardening plastic response that can be described by the Johnson-Cook model. Material properties shown in Table 3 are used to model the sheets and the walls of the perturbed cores in this work. The material properties for the three-point bending test for the sinusoidal honeycomb core are different than those used in the uniaxial compression, bending, and shear tests, which ensure that the model is validated with experimental results.

To simplify the modeling process, the sheets are assumed to be perfectly bonded to the core. Thus, the finite element model does not consider the adhesive layer that typically bonds the sheets to the core. This assumption might not be accurate at very large deformations or in situations involving large cyclic loading. However, under 3-point bend loading, the load under the loading roller is compressive, and debonding between the sheets and core is not usually observed in experiments [116]. Thus, modeling the adhesive sheet is not required, and the sheets can be considered fully bonded to the core. Adding on, the aluminum core and sheets are assumed to have isotropic material properties, and the perturbed waves are assumed not to have any imperfections, which could be a result of the manufacturing process.

Table 3: Three-point bending material properties

Material	**ρ(kg/m3)**	**E(MPa)**	**μ**	**A(MPa)**	**B(MPa)**	**n**	**m**
Al5052-Core	2680	73,000	0.33	148	345	0.18	0.859
				Yield Strength (MPa)			
Al5052-Sheets	2680	53,500	0.33	114	-	-	-

The interactions between the rollers and the sheets of the sandwich structure are modeled using surface-to-surface interactions, which assumes the friction coefficient between the rollers and sheets to be 0.2. The boundary conditions used to simulate the

3-point bend test are shown in Figure 17. The two lower rollers are constrained in all directions, while the top roller is allowed to move along the vertical direction only.

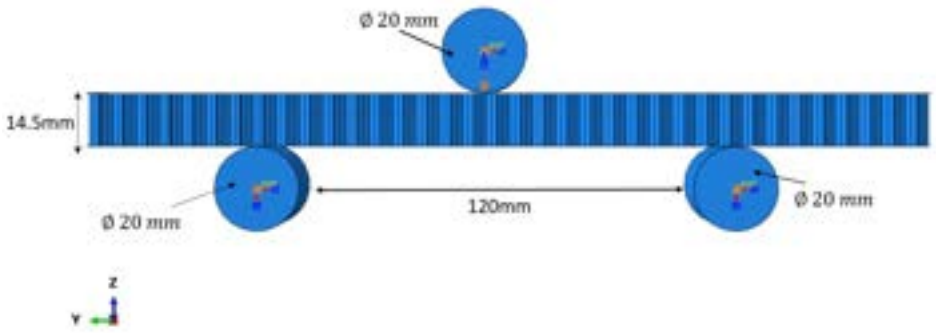

Figure 17: Three-point bending boundary conditions

A displacement rate of 50mm/s is applied on the top roller to load the sandwich structure. This rate is used in this work as it was used to load sandwich structures similar to the ones used in this work but with traditional cores [116]. Having a benchmark allows for evaluating the effect of applying perturbations to the cores of sandwich structures.

6.1.5 Validation of the finite element models

The ability of the finite element models to capture the honeycomb cores' behavior under out-of-plane loading conditions is verified by comparing the buckling strength determined using finite element models with that obtained analytically [49] for the parent unperturbed honeycomb. The comparison, shown in Figure 18a, demonstrates the excellent agreement between the finite element and analytical results, underscoring the accuracy of the finite element models. The finite element results employed in the comparison correspond to the third loading condition, namely the loading of a single cell.

This loading closely aligns with the implicit assumptions incorporated into the analytical model, which was derived using a hexagonal unit cell. Similarly, the accuracy of the in-plane finite element models is verified by modeling an aluminum honeycomb characterized experimentally in the literature [117]. Figure 18b compares the finite element predicted response with the experimental results and demonstrates their

excellent agreement. The finite element models used in the comparison utilized the cell size and material properties of the honeycomb core used in the experiments [117].

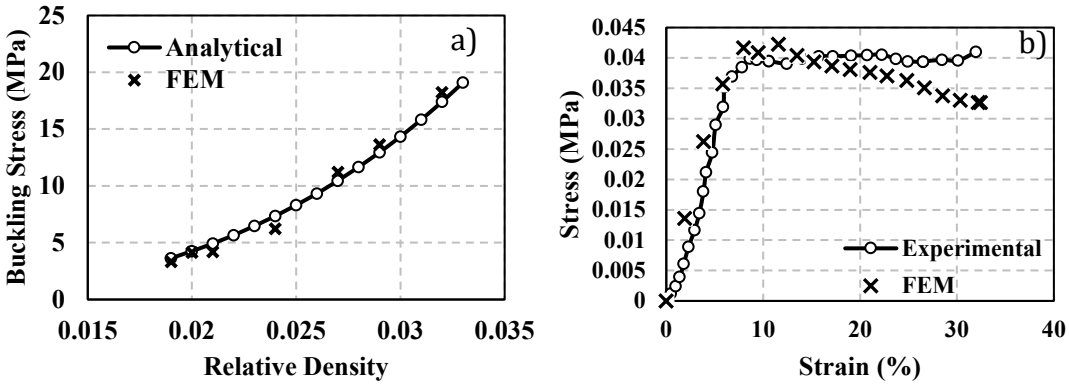

Figure 18: Validation of the out-of-plane and in-plane finite element models, showing a) a comparison between the finite element predicted buckling strength and the analytical one [50] and b) a comparison between the finite element predicted compressive stress-strain response and the experimentally determined [117]

6.2 Application of Metallic Coating on Metallic Foams

This work will utilize finite element analysis (FEA) and representative unit cell approach to analyze the behavior of hybrid coated open-cell foams with a wide range of porosities. The commercial finite element software ABAQUS is used throughout this work as it proved effective in modeling the response of cellular solids in general (e.g., [63], [118]). ABAQUS has a rich library of elements and constitutive models that allows it to model the physical behavior (i.e., elastic and plastic deformations as well as heat conduction) considered in this study effectively. The following details the process used to create and analyze the foam models.

Additionally, experimental tests were conducted on functionally copper-coated aluminum foams. The porosities, pore size, and cell thickness are no longer studied in the experimental part; instead, the electrodeposition time is varied to achieve a functionally graded coating thickness. Characterization techniques, including SEM and energy-dispersive X-ray Spectroscopy (EDS), are used to gain a comprehensive understanding of the morphological features of the coated and uncoated samples. Additionally, the Vickers Hardness test is conducted on the uncoated samples to assess the microhardness of the cell walls. Quasi-static compression tests are conducted on the coated and uncoated samples to determine the effectiveness of the copper coating. This

is done by evaluating Young's modulus, plateau stress, densification strain, and energy absorption capabilities.

6.2.1 Finite element modeling Voronoi foam structures

Voronoi tessellations are used in this work to represent the geometry of open-cell foams as they can effectively represent the underlying physical processes (i.e., nucleation, growth, and coalescence of gas bubbles) driving the formation of the inner structure of open-cell foams during casting [119]. Voronoi tessellations have been frequently used to represent open-cell foams [63], particularly in conjunction with FEA, as they can capture the stochastic and geometric features of open-cell foams accurately. Generating the Voronoi-based geometry is performed using the commercial software nTopology from nTopology, NY. To create the Voronoi-based geometry, seed points are created first. An average limiting distance of 3 mm is enforced between the nearest neighbors. This distance represents the average spacing between two adjacent nucleation points and represents the average cell size in the final Voronoi structure. An average spacing of 3 mm is chosen as many commercially available open-cell aluminum foams have an average cell size of about 3 mm [120], [121]. Upon creating the seed points, the nToplogy software creates the Voronoi tessellation automatically. The resulting Voronoi geometry is represented by lines, as seen in Figure 19. These lines are subsequently assigned thickness and converted to solid struts. The thickness assigned is calculated based on the desired porosity, which is defined as the ratio of the volume of the porous phase to the volume of the cube occupied by the solid phase.

Figure 19 shows the process of generating a Voronoi open-cell foam representing a sample: creating seed points, generating Voronoi tessellation (line representation), and assigning thickness to the lines. The size of Voronoi-based samples, such as the one shown in Figure 19, should be selected carefully to ensure that the behavior of the Voronoi sample is representative of that of an infinitely large sample. When this condition is satisfied, the Voronoi sample can be referred to as a representative volume element. For the condition to be satisfied, the Voronoi sample should include enough cells to eliminate free boundary effects and obtain size-independent results. Using representative cells is important as large Voronoi samples can be computationally prohibitively expensive.

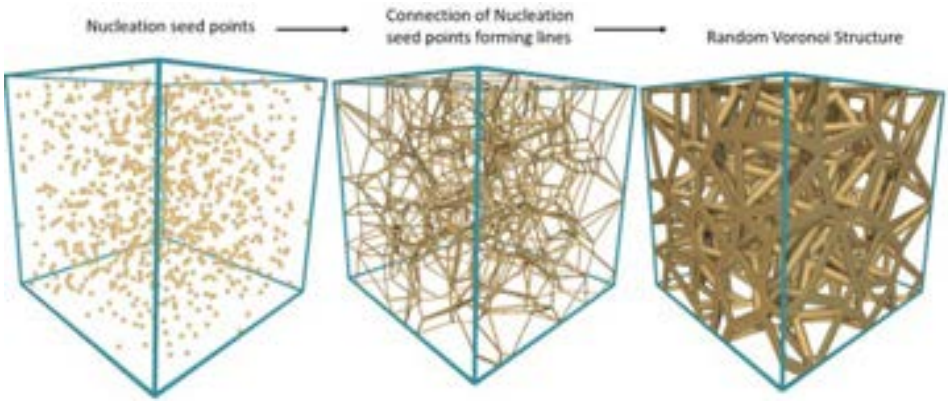

Figure 19: The process of creating a Voronoi tessellation, showing seed points (left), Voronoi line representation (middle), and final Voronoi tessellation with solid ligaments (right)

According to the literature, using a cubic sample with a cube length-to-cell size ratio of 8 is sufficient to realize size-independent elastic and yield behaviors for Voronoi-based foams and open-cell foams [121]. As an additional verification measure, the effect of sample size on their stiffness was investigated in this work. Accordingly, cubic Voronoi foam samples with sizes that translate to length (a) to average cell size (d) ratios of 4, 6, 8, 10, 12, and 14 were modeled, and their elastic modulus was determined. These samples, which used aluminum as a constituent material and did not include a coating, had an average cell size of 3 mm, a porosity of 80%, and accounted for the effect of randomness during nucleation. For the latter, at each a/d ratio, 4 samples were created.

Each had its random seed points and thus Voronoi geometry. The elastic moduli of the Voronoi samples with different a/d ratios are shown in Figure 20. Error bars in Figure 20 represent the effect of the randomness of seed points. Error bars represent the deviation of the maximum and minimum obtained moduli from the mean at a given a/d ratio. Results in Figure 20, particularly when considering the spread represented by error bars, confirm that an a/d ratio of 8 is sufficient to realize relatively size-independent behavior.

The abovementioned approach for creating Voronoi foams is used to create Voronoi samples with 5 relative densities (20%, 15%, 10%, 7%, 4%). Multiple porosities are considered to investigate the effect of porosity on the response of the hybrid copper-coated aluminum foams.

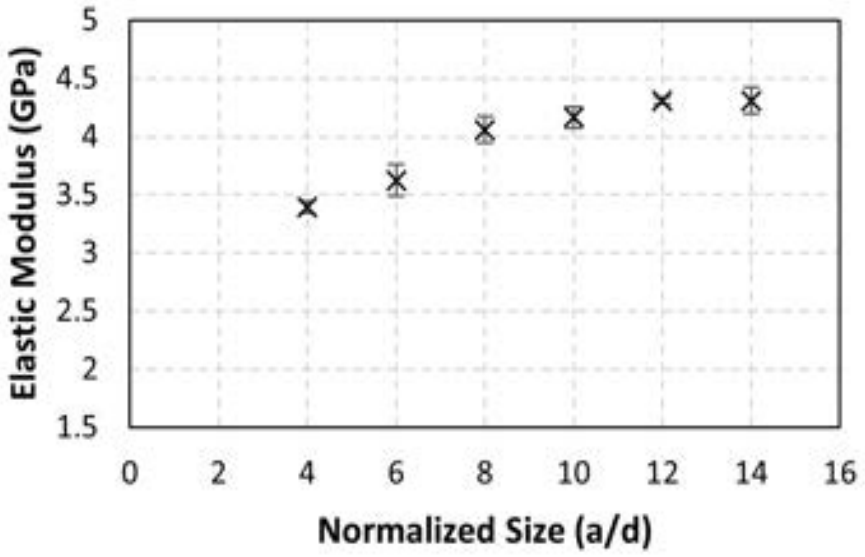

Figure 20: Effect of cell size and seed point randomness on the elastic modulus

The same seed points are used to create the Voronoi samples with different porosities to eliminate randomness effects. Created Voronoi foam samples have an average cell size (d) of 3 mm and a cubic length (a) of 24 mm, thus satisfying the condition of a/d=8

6.2.2 Finite element modeling – static tests

The solid struts of the Voronoi foam samples are meshed using tetrahedral 4-node linear elements. Voronoi foam samples are converted to hybrid copper-coated foams by adding a shell-element-based coating layer, as shown in Figure 21. This layer is created using ABAQUS's shell offset mesh tool command which creates a layer of shell element on the outer surfaces of solid features. Shell elements representing the coatings are assumed to be fully bonded to the tetrahedral elements representing the aluminum substrate underneath them. Triangular 3-node linear elements are used to model the shell-elements-based coatings.

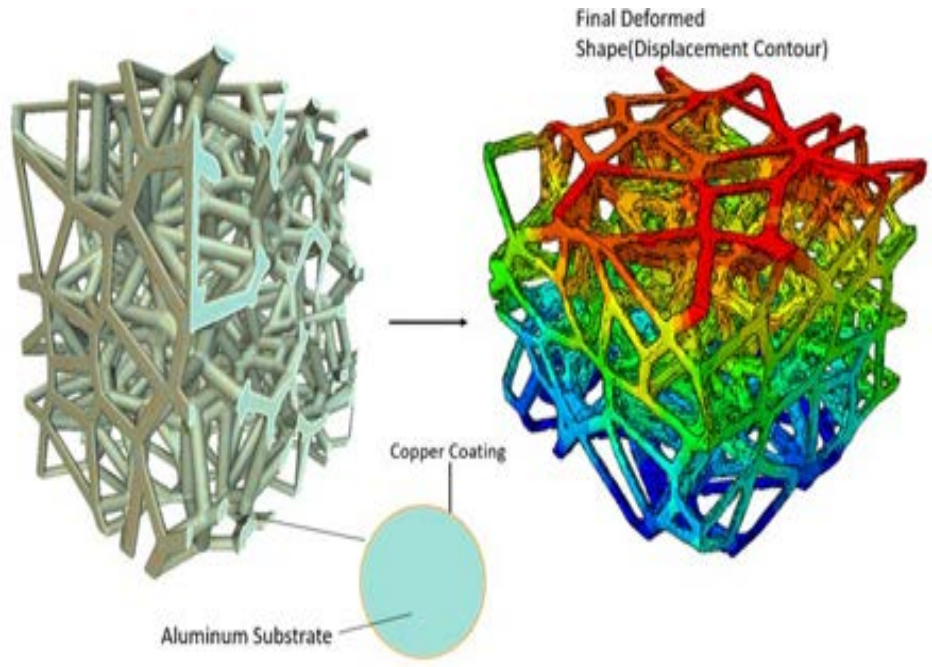

Figure 21: Copper coated Voronoi foam and the final deformed shape

Modeled hybrid-coated foams are comprised of a copper coating and an aluminum open-foam substrate. The Johnson-Cook model is used to represent the plastic behavior of the copper and aluminum phases. The material properties of copper and aluminum used in the models are listed in Table 4 [122].

A linear static coupled temperature-displacement analysis is used to determine the thermal conductivity of the unit cell samples. On the other hand, a non-linear static analysis is used to determine the sample's elastic modulus and yield strength. A schematic illustrating the loading conditions used is shown in Figure 22.

Table 4: Properties of copper and aluminum used in FEA models

Material	**ρ(kg/mm3)**	**E(MPa)**	**μ**	**Tm (K)**	**A**	**B**	**n**	**M**	**k(W/mK)**
Al	$2.70 * 10^{-6}$	72,000	0.33	893.15	148	345	0.183	0.859	237.2
Cu	$8.96 * 10^{-6}$	124,000	0.34	135 6	90	292	0.31	1.09	386

To determine the heat conductivity of a particular sample, its top and bottom surfaces were subjected to the temperatures of 400 K and 273 K, respectively. Subsequently, the heat flux (q) at both the top and bottom surfaces is computed using

the finite element software. The heat flux (q) is used in conjunction with Fourier law $q = -k\Delta T/L$ to compute the effective heat conduction coefficient (k).

Here, ΔT is the temperature difference across the specimen boundaries, and L is the specimen length. The lateral faces of the samples are assumed to be insulated to render the problem at the homogenous level one dimensional. To determine the elastic modulus and yield strength, a displacement (along the y-axis) of 0.5 mm is prescribed to the nodes situated on the sample's top surface, while the nodes on its bottom boundary are constrained (i.e., their y-direction displacement is fixed).

The lateral surfaces of the foam sample are assumed to be traction-free. The reaction forces at the top boundary are computed using ABAQUS and used to calculate the nominal stress, while the displacement of the top nodes is used to compute the nominal strain. Subsequently, the nominal stress-strain curves are plotted and used to determine the sample modulus (slope of the linear phase) and yield strength (using the 0.2% offset).

A mesh sensitivity analysis was performed to ensure that the results were mesh size independent. This analysis was performed on non-coated Voronoi foam samples with 15% relative density. The mesh size was characterized using the average element length (l) to strut diameter (ϕ) ratio. Multiple l/ϕ ratios were considered, namely 1.48, 2.52, 3.6, and 5.04. The change in the elastic, yield, and effective heat conduction coefficient obtained using the l/ϕ ratio of 5.04 are within 0.5% of their counterparts obtained using the l/ϕ ratio of 3.6. Thus, an average element size to strut diameter of approximately 5 is used throughout this work.

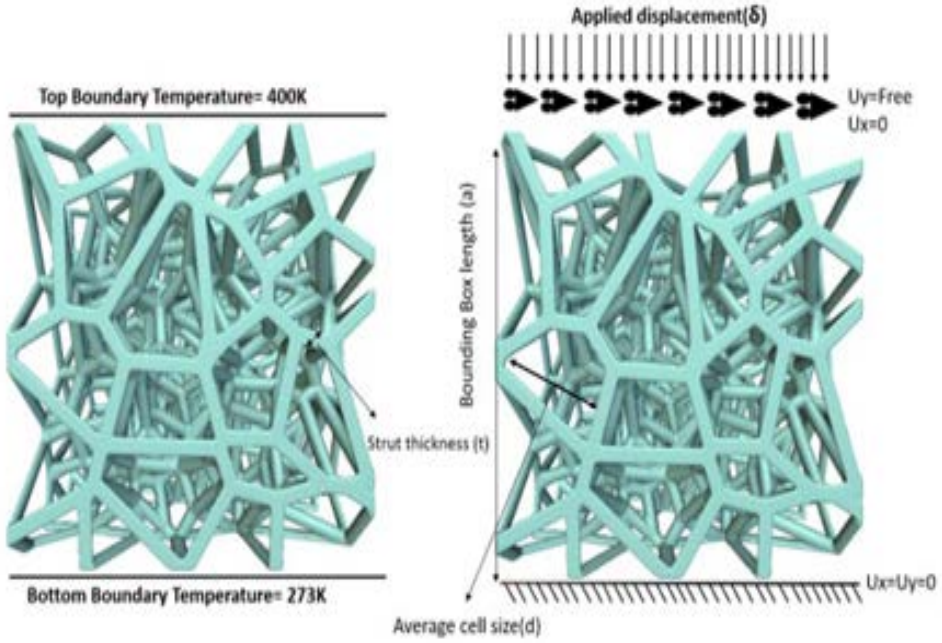

Figure 22: Uni-axial compression and temperature boundary conditions applied

6.2.3 Finite element modeling – dynamic tests

Models of open-cell foams were generated using Voronoi tessellations. The analyzed foam was assumed to have a relative density of 0.15 (85% Porosity) and a pore size of 3 mm. These properties are chosen as they are consistent with the properties of the commercially available ALPORAS aluminum open-cell foams, similar to those in Sections 6.2.2 and 6.2.4. The Voronoi tessellations that were used in this study follow a similar process of modeling to that in Section 6.2.1.

The Voronoi-based foam model occupied a cubic volume with a side length of 24 mm. The cube dimensions are chosen to be big enough to represent the bulk behavior of the foam yet to be small enough to reduce the computational cost of the dynamic analysis. For a model to represent the bulk behavior of its parent foam, it has to include enough number of cells. This condition can be satisfied if the cube length to cell size ratio is 8 or higher, as illustrated in Figure 20.

The size of the models in this work is consistent with the latter ratio. The cell walls of the open-foam model were assumed to be made of aluminum. The metallic coating applied on the aluminum cell was assumed to be made of copper. The applied coatings had a range of thicknesses, namely 30 μm, 50 μm and 100 μm. The material properties of the aluminum and copper used in the models are shown in Table 4.

The plastic deformation of both aluminum and copper was modeled using Johnson Cooke's model with the constants defined in Table 4. Contact between cell walls was modeled to capture densification upon the collapse of cell walls. The explicit ABAQUS solver is used as it is very efficient in detecting and resolving surface contacts in problems involving large deformations. The metallic coating was modeled using S3R shell elements, while the foam's cell wall was modeled using C3D4 linear tetrahedral elements. The shell elements were assumed to be fully bonded to the tetrahedral elements of the cell walls.

Upon conducting mesh sensitivity analysis, it was found that using a total of 533,145 C3D4 Linear tetrahedral elements and 198,512 S3R linear triangular shell elements allows for realizing a mesh-independent solution. The high number of elements used increased the computational cost but was needed to ensure the accuracy of the results. To model wall to wall contact interaction, the dynamic explicit general contact interaction algorithm was used. Accordingly, a contact property was imposed on all cell walls.

The interaction property assumed interacting surfaces to have frictionless tangential behavior. In addition, it assumed that the normal behavior between interacting surfaces was to follow the hard contact option in ABAQUS.

Low impact velocity was imposed on the model by applying a vertical velocity of 5 m/s for 0.005 seconds to its top surface. This loading condition is equivalent to a strain rate of 200 s−1. The vertical displacements at the bottom surface of the model were constrained. A schematic representation of the model and the imposed boundary conditions is shown in Figure 23.

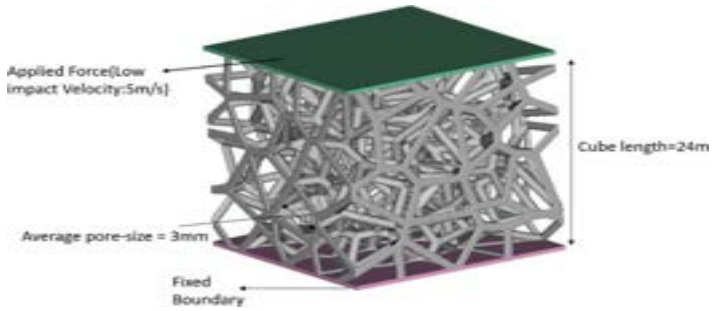

Figure 23: A schematic representation of the open-cell foam, loading, and boundary conditions used in the finite element models

6.2.4 Uniaxial compression testing – functionally graded samples

Open-cell aluminum foams were subjected to varying durations of electrodeposition to achieve different levels of coating thickness. The aluminum foams used in this study, sourced from Duocel® by ERG Material, exhibited an average porosity of 90% with a Pores Per Inch (PPI) of 10 and were composed of base material Al6101 T6. The geometric and material properties of the samples are outlined in this section. Figure 24 shows the workflow that has been adopted in this study.

Electrodeposition was utilized to attain the desired coating thicknesses, followed by various characterization techniques. SEM was utilized for profiling the coating thickness along the length of the foam samples, and Vickers Hardness testing was conducted on the uncoated samples to assess the microhardness of the aluminum cell walls, which was then compared to the bulk hardness of the aluminum reported in the literature. Additionally, EDS was used to determine the compositional distribution of the aluminum foam. Electrodeposition was carried out on three samples for different durations— 3600 s, 5000 s, and 9000 s. To ensure consistency and repeatability, each sample was replicated four times, resulting in a total of 12 coated and 4 uncoated samples. These samples were subjected to quasi-static compression testing to evaluate their elastic modulus, plateau stress, and energy absorption capabilities.

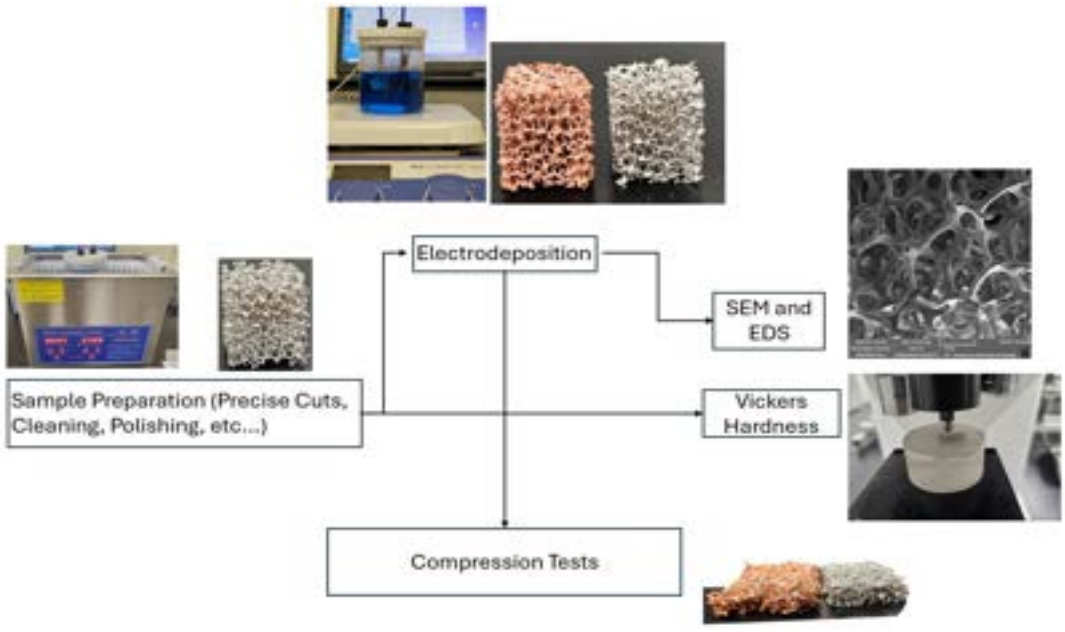

Figure 24: Static experimental tests on aluminum foam workflow

6.2.4.1 Aluminum foam properties

A total of 16 samples were utilized in this study, each with slight variation in the geometrical properties due to the stochastic nature of the foam structure. Depending on the electrodeposition time, the added weight of copper varied for each sample. Table 5 shows the geometrical properties of all the samples that were tested.

The electrodeposition time was varied across 12 samples, which resulted in an increase in the coating thickness for the samples with higher electrodeposition time. Depending on the stochastic nature of the foam samples, the average coating thickness on the surface varied. Additionally, the slight variation in the surface area within each sample results in a difference in the added copper weight within the samples.

6.2.4.2 Coating technique

The coated samples were prepared with the aid of electrodeposition, specifically following the procedure designed by Wang et al. [15]. Initially, the foam specimens were subjected to a pre-treatment process in which the samples were rinsed with ethanol and deionized water in an ultrasonic cleaner for a total of 10 minutes. This is done to remove any contaminants and ensure a clean surface that is more effective in electrodeposition. This step is essential for ensuring a uniform coating layer and enhancing the adhesion of copper to the aluminum substrate. The specimens were subjected to electrodeposition using a 0.5 M solution of copper sulfate ($CuSO_4$) in 250 ml solution.

The molarity of the copper sulfate was carefully determined through an iterative process to optimize the uniformity of the coating, coating adhesion, and effective deposition time. Throughout the deposition process, the electrolyte, anode, and cathode were maintained at a temperature of 65°C, and a magnetic stirrer was used in the solution at 180 rpm to minimize electrolyte concentration gradients. The electrodeposition process was carried out at approximately 0.3 mA/cm2 current density. The schematic and setup of this process are shown in Figure 25.

Table 5: Geometric properties of samples

Sample	**Electroplating Time(s)**	**Avg Coating Thickness (Surface)(μm)**	**Mass before plating (g)**	**Mass after plating (g)**	**Dimensions (length x width x height)**
Al-F1	0	0	0.4176	-	12.02x11.95x14.67
Al-F2	0	0	0.4362	-	12.06x12.01x15.05
Al-F3	0	0	0.4082	-	12.16x12.12x14.30
Al/Cu-F1(3600S)	3600	37.36	0.4297	0.7386	12.21x12x15.35
Al/Cu-F2(3600S)	3600	39.28	0.4426	0.7832	12.24x12.02x16.25
Al/Cu-F3(3600S)	3600	39.01	0.4073	0.7182	12.26x12.15x14.55
Al/Cu-F4(3600S)	3600	38.72	0.4321	0.7821	12.39x12.05x15.60
Al/Cu-F1(5000S)	5000	55.09	0.4178	0.8542	13.33x12.16x16.25
Al/Cu-F2(5000S)	5000	51.88	0.4081	0.8663	12.42x12.02x16.49
Al/Cu-F3(5000S)	5000	48.9	0.4356	0.8542	11.95x12.18x15.50
Al/Cu-F4(5000S)	5000	53.04	0.4240	0.8240	12.21x12.12x14.69
Al/Cu-F1(9000S)	9000	59.88	0.4070	1.1053	12.47x12.25x14.92
Al/Cu-F2(9000S)	9000	66.28	0.3996	1.059	12.36x12.46x14.51
Al/Cu-F3(9000S)	9000	64.08	0.4391	0.9962	12.20x12.12x14.82
Al/Cu-F4(9000S)	9000	62.57	0.4331	1.029	12.21x12.12x14.51

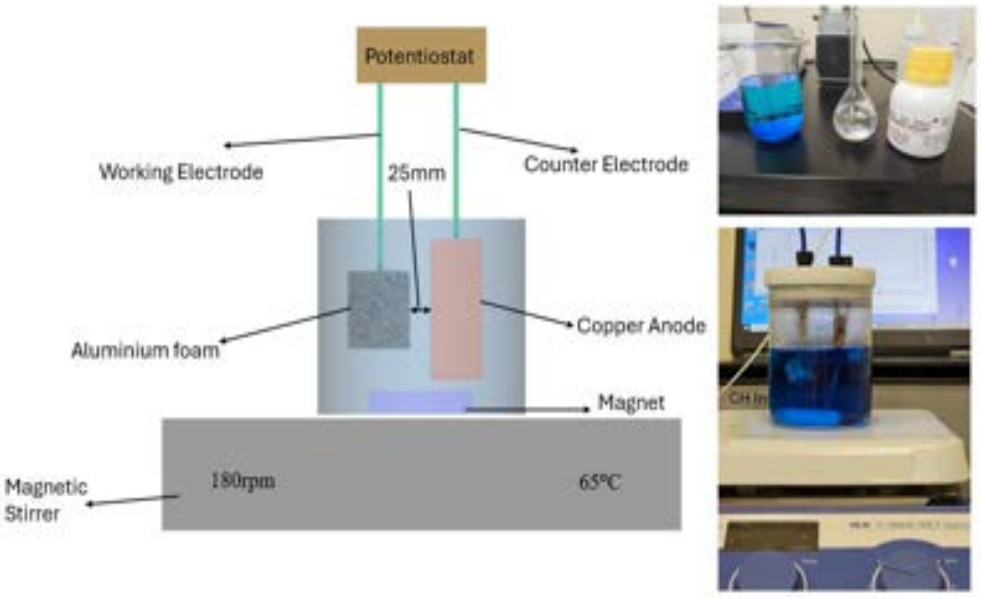

Figure 25: Electrodeposition schematic

For the anode setup, a pure 99% copper plate was attached to a copper wire that was tied to the counter electrode, ensuring high purity of the deposited copper ions. The aluminum foam sample was connected to a copper wire, which was linked to the working electrode with a copper wire. To maintain consistency in the coating results, the distance between the cathode and anode was fixed at 25 mm for all samples. The final samples coated samples, one from each electrodeposition time, and the uncoated samples are shown in Figure 26. It is evident from the color of the samples that there is a variation in the coating thickness, which is due to the variation in the electrodeposition time.

Figure 26: Samples from each coated and uncoated specimen

Post-electrodeposition, the samples were rinsed with ionized water to remove any residual electrolyte, thereby preventing contamination and ensuring the integrity of the

copper coating. The rinsing is essential for maintaining the purity and quality of the coated surfaces, leading to a consistent experimental result.

6.2.4.3 SEM and EDS

SEM was utilized to characterize the coated and uncoated samples. For the coated samples, the surface was polished to expose the contact area between the coating and the substrate. During the electrodeposition process, the distribution of the coating thickness across the thickness of a foam structure inherently exhibits non-uniformity due to the limitations in the current distribution and electrolyte accessibility within the porous medium. At the surface of the foam, where the coating thickness was recorded and tabulated in Table 5, the coating thickness tends to be the highest because this area is mostly directly exposed to the electrolyte and receives the greatest density of the electrical current flow. The ions in the electrolyte have unimpeded access to the surface, which allows for a more concentrated and uniform deposition of the coating material. Figure 27 shows a wide channel image of coated and uncoated samples.

(a) (b)

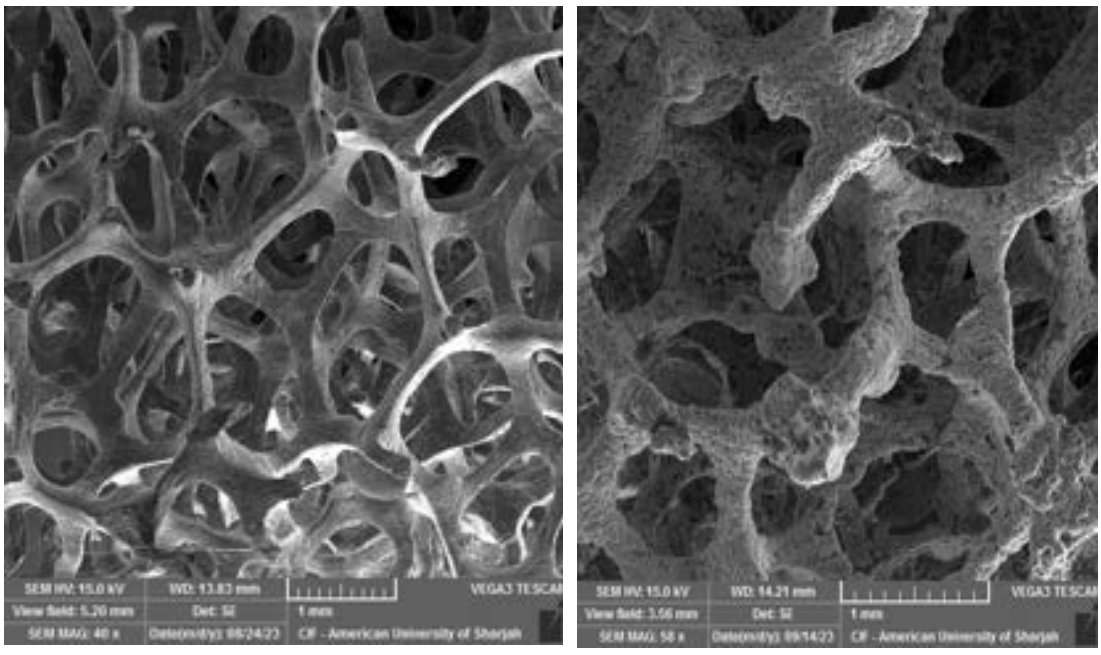

Figure 27: SEM wide channel images of (a) uncoated Al F3 (b) Al/Cu F2 (5000s)

From the uncoated sample, it is evident that the strut thickness is much smaller than the coated sample. Additionally, there are little variations in the pore sizes,

showcasing a homogeneous distribution, which indicates a controlled foaming process despite the stochastic nature of the foam structure. The coated sample shown in Figure 27b shows the uniformity of the coating layer on the struts. Looking deeper into the thickness from the taken image, the coating thickness starts to diminish slowly, which will be shown in further detail in other SEM images. To capture the pore sizes and the strut thicknesses, an SEM image was taken for the uncoated sample, see Figure 28.

As shown in Figure 28, the uncoated samples have a strut thickness of 200 μm, which is consistent across all uncoated samples. Examining the surface morphology of the sample, it is evident that there are various defects within the struts, highlighted within the red circles. Such irregularities and other possible cracks within the struts can directly affect the material properties. The presence of defects within the struts can also influence the coating process. For instance, pores such as the ones highlighted in red can lead to an uneven distribution of the coating thickness, thereby compromising the mechanical properties of the aluminum foam.

Figure 28: Strut thickness and defects in Al F3

Additionally, if these defects are not adequately covered, it could lead to weak points within the strut, which could lead to localized buckling and global reduction in

the stiffness of the sample. Evidently, as shown in Figure 29, such defects can also lead to potential adhesion problems.

The presence of defects in the substrate has led to adhesion problems in the copper coating that was applied, which potentially led to the peeling of the coated layer, thereby reducing the effectiveness and durability of the sample.

Each sample was sectioned four times to assess the variations in coating thickness throughout its depth. Images were captured at specific depths of 0mm, 2mm, 6mm, and 10mm within the average sample height of 14 mm. This methodical slicing and imaging at progressive intervals enabled a deeper understanding of how the coating thickness changes from the surface to the interior. Detailed thickness profiling helps in understanding the uniformity and penetration of the coating process, which is crucial for evaluating the coating's effectiveness and consistency. The thickness profiling for the lowest electrodeposition samples is shown in Figure 30. At 0 mm, surface coating, the coating thickness varies at the edges of the sample when compared to the middle of the sample. Evidently, in the middle of the sample at 0mm, the coating thickness is shown to be uniform along the struts at 39.12 μm, whereas on the surface, the coating is higher at an average of 57.83 μm.

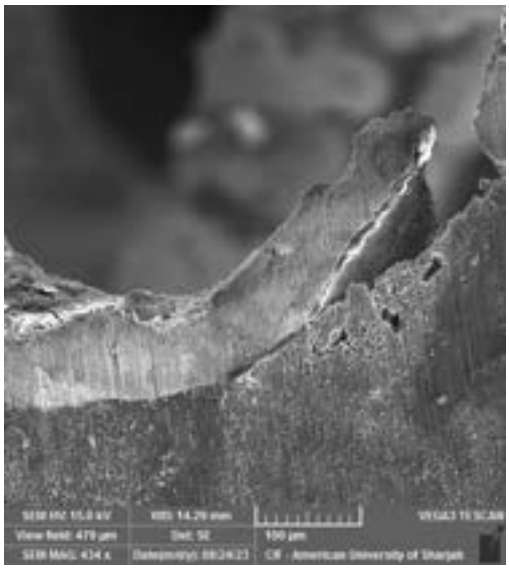

Figure 29: Peeled copper coated layer in Al F1

After a deeper look into the foam structure, it is evident that the accessibility of the electrolyte diminishes, and the path of electric current becomes increasingly

obscured by the already deposited material. The case of diminishing coating thickness, thereby achieving a functionally graded coating through electrodeposition, is evident across all samples with different electrodeposition times.

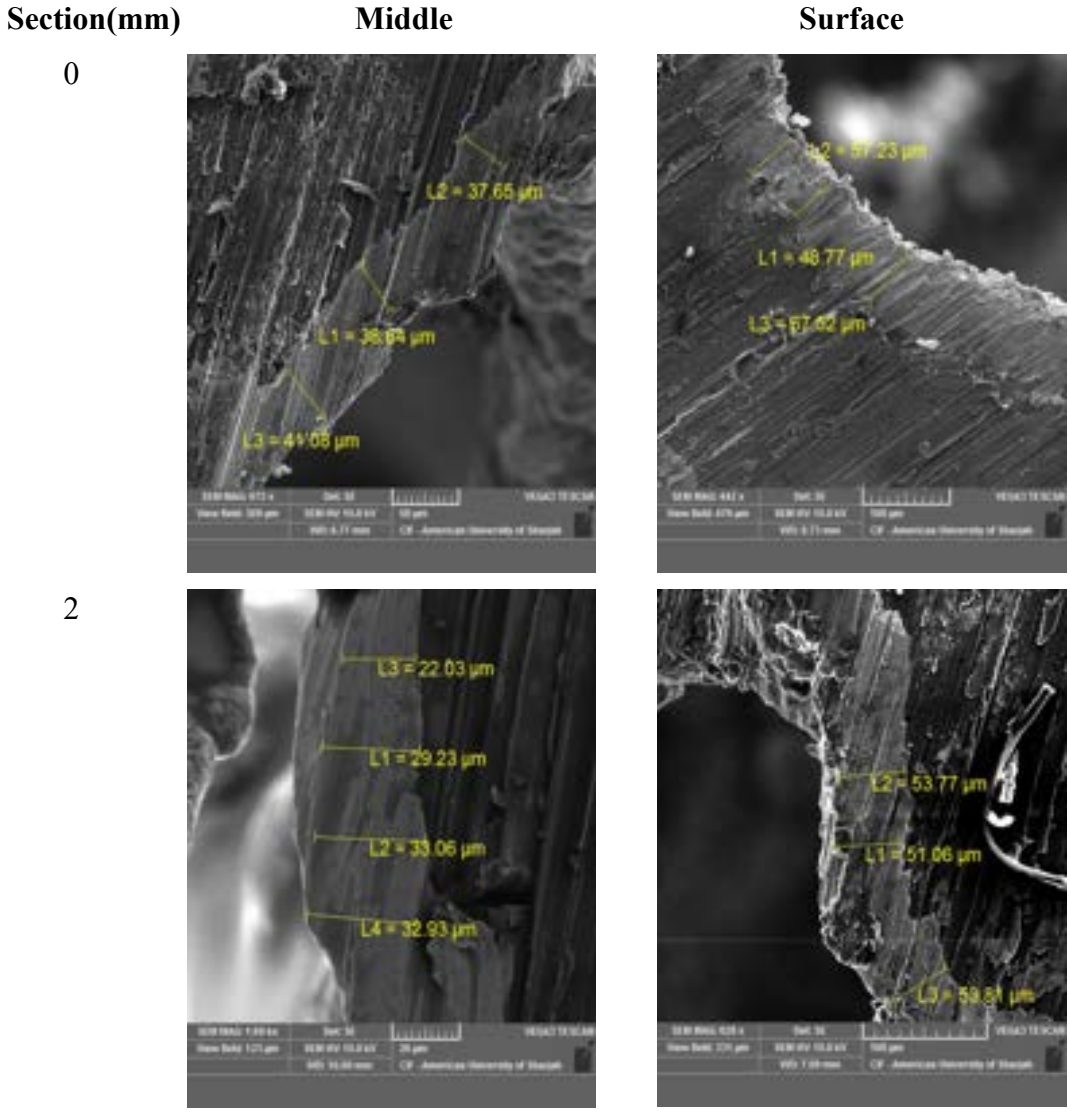

Figure 30: Thickness profiling through SEM images of 3600s Al/Cu specimen

6

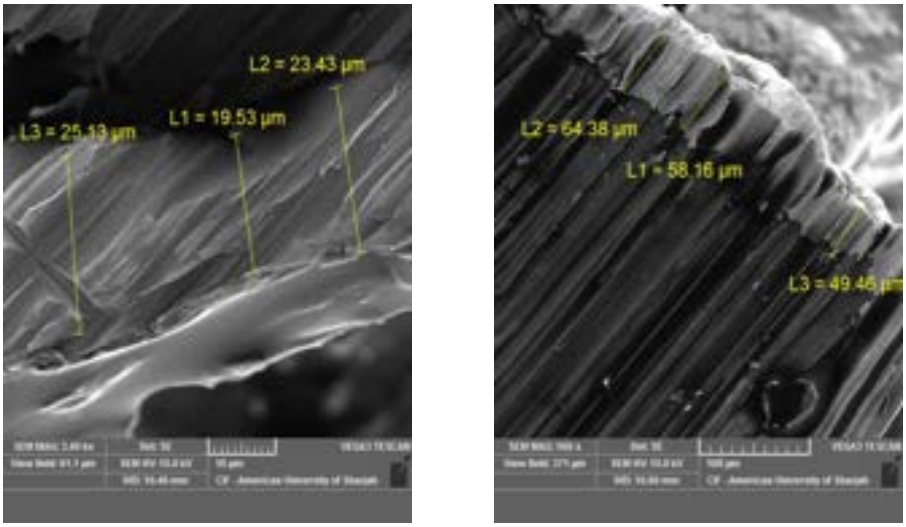

10

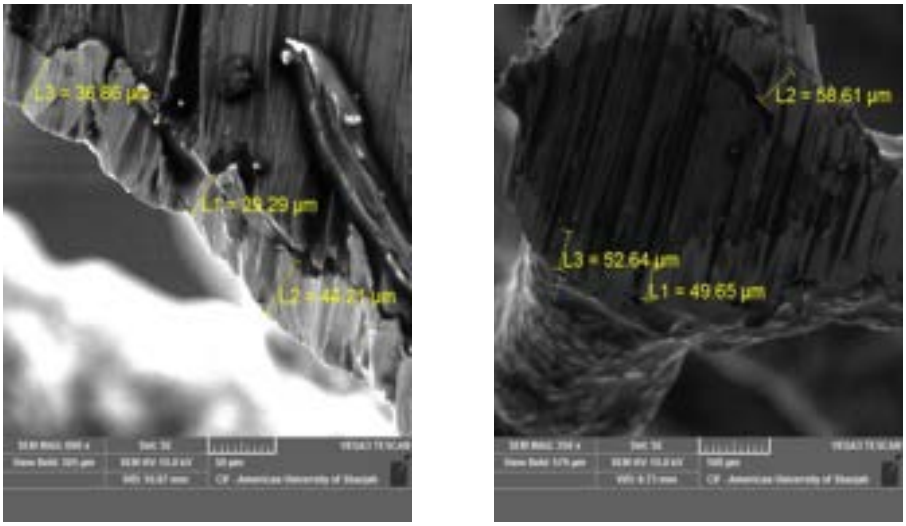

Figure 30: Thickness profiling through SEM images of 3600s Al/Cu specimen (continued)

EDS was used to determine the compositional distribution of the coated and uncoated samples. The highest coated sample was used to showcase the distribution of the copper content in the samples. Figure 31 shows the elemental compositional distribution of Al/Cu F4 that was electrodeposited for 9000 s.

The EDS shows the elemental distribution by showing the characteristics of the X-ray peaks that the elements present. The x-axis shows the energy of the detected X-rays, measured in kiloelectron volts (keV), where each element has a characteristic peak at a specific energy. The y-axis shows the counts per second per electron volt. The intensity of the detected X-rays is recorded, which is proportional to the amount of each element that is present in the sample. Specifically, for this sample, the highest peak was

recorded to be 1.5 keV, which signifies the high presence of aluminum in the foam sample.

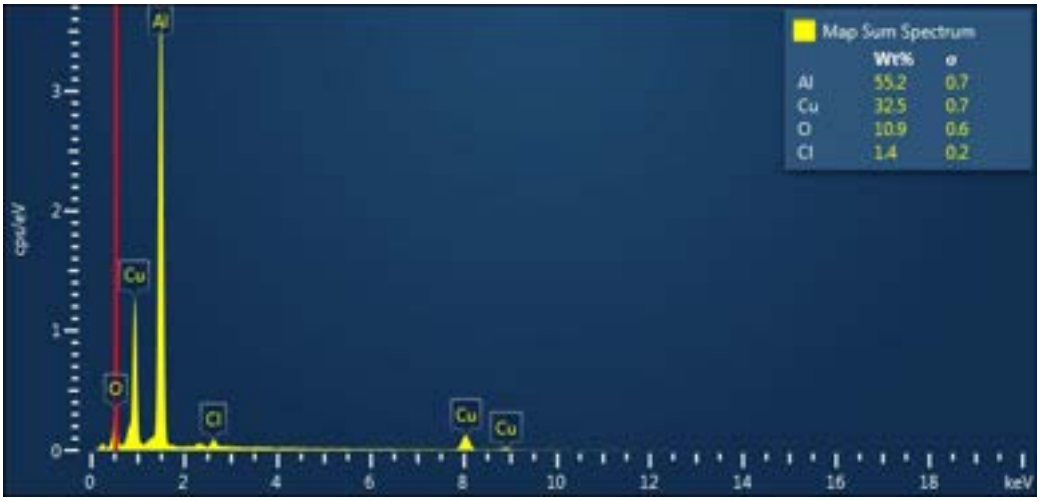

Figure 31: EDS map spectrum showing the elemental distribution of Al/Cu F4 - 9000s

This is justified as the substrate of the foam sample is aluminum. The second-highest peak, observed at around 0.9 keV and 8 keV, shows the presence of the copper coating in the sample. Smaller peaks are also evident in the compositional distribution where 0.5 keV of Oxygen indicates the presence of surface oxidation or defects. Additionally, there is also a small of around 0.15keV, indicating a minor presence of chlorine, suggesting that there remains small containments or residues from the coating process as the presence of the acid in the electrolyte can remain within the sample after the electrodeposition process is done. The legend in the figure shows the weight percentages and the standard deviations of each of the elements. It is evident that the highest element is the substrate element, aluminum, at 55.2%. Copper is the second highest weighted percentage, measured at 32.5%, which is a result of a total of 9000 s. The rest of the distribution is 10.9% oxygen and 1.4% chlorine. Similarly, this was done for the rest of the samples, and the elemental distribution for elements higher than 1% is recorded and shown in Table 6.

Table 6: Elemental distribution of coated samples with EDS

	Elements			
Sample	**Aluminium (Al)**	**Copper (Cu)**	**Oxygen (O)**	**Chlorine (Cl)**
Al Foam	93.7%	0%	6.3%	0%
Al/Cu Foam 3600s	78%	12.8%	8.6%	0.6%
Al/Cu Foam 5000s	66.6%	23.1%	9.5%	0.8%
Al/Cu Foam 9000s	56.7%	31.8%	10.3%	1.2%

The results are averaged over the different types of samples (coated and uncoated), with each of the electrodeposition times. The high electrodeposition time results in higher oxygen and chlorine distribution within the sample, as the presence of the sample for higher times in the electrolyte results in higher chlorine elements residue within the sample. Adding on, the electrodeposition time is directly proportional to the coating thickness and percentage of added copper, as evidenced by both the SEM and EDS. To further show the distribution of copper content on the aluminum substrate, showcasing the uniformity of the coating, the SEM image is captured and analyzed by EDS to show the elemental distribution on the cross-section of a strut. Figure 32 shows the cross-sectional SEM image of a strut from Al/Cu 5000s F3 that was subjected to EDS analysis to show the elemental distribution.

The SEM and EDS images effectively illustrate the elemental distribution on the surface of a copper-coated aluminum foam. The EDS layered image combines the distributions of aluminum (red), copper (blue/cyan), and oxygen (green) with an electron image (gray) showing the overall morphology. The copper coating forms a relatively uniform layer over the aluminum substrate, prominently visible in the middle region of the image. The underlying aluminum is primarily located in the lower part of the image, where the copper layer is absent or thinner.

Oxygen is concentrated around defects and edges of the copper coating, indicating regions more susceptible to oxidation due to exposure. These defects appear as irregularities or discontinuities in the copper layer, where the protective coating is compromised, allowing oxidation to occur. The presence of oxygen around these

defects suggests the formation of oxides, likely aluminum oxide or copper oxide, at these sites.

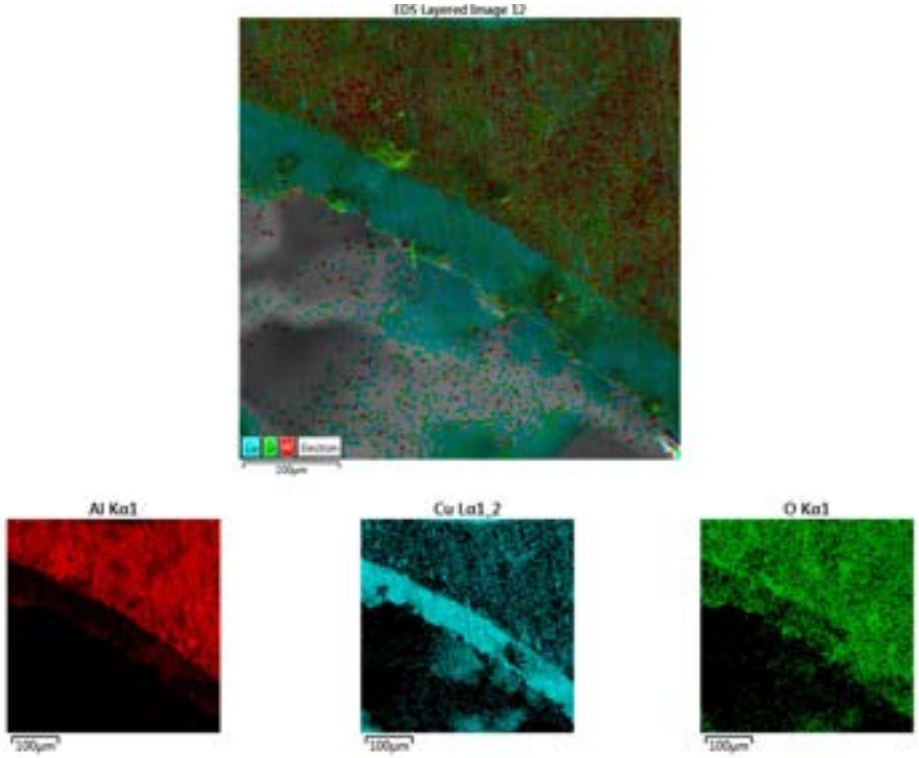

Figure 32: SEM and EDS images of Al/Cu F4 - 5000s

6.2.4.4 Vickers hardness

The Vickers Hardness test is used to evaluate the mechanical properties of the foam's base material, particularly due to its capability to measure the microhardness of the base material. Inhomogeneities in the cell walls, defects, and micro-cracks can significantly affect the material's ability to bear loads and resist deformation. Applying Vicker's hardness test, the hardness number is obtained by calculating the indented surface area, which can reveal the influence of these defects on the foam. Figure 33 shows the hardness test that was conducted on the uncoated aluminum sample. The process involves pressing a diamond pyramid indenter with a square base and an angle of 136° between the opposite faces on the surface of the material under 1.96 N. The indenter is typically held in place for a predetermined amount of time, after which the load is removed, and the impression left by the indenter is measured.

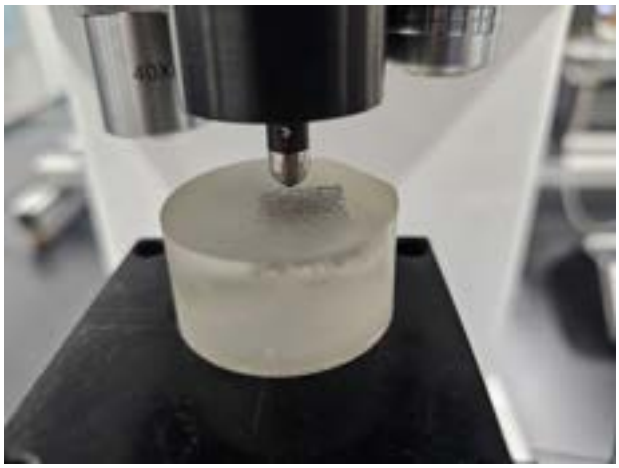

Figure 33: Vickers Hardness mounted sample setup

A smooth and clean surface should be maintained when applying the Vickers test to an aluminum foam, as surface roughness and contamination can affect test results. The aluminum foam was mounted in a resin mold to stabilize the specimen. The foam was embedded in a resin matrix, providing a supportive backdrop that prevents the material from deforming or breaking under pressure, as shown in Figure 33. A total of eight indentations were taken, one of which is shown in Figure 34.

The hardness number was calculated by,

$$HV = \frac{2F \sin\left(\frac{\theta}{2}\right)}{d^2} \tag{42}$$

where F is the applied load in kilograms-force (kgf), θ is the angle between the opposite faces of the diamond pyramid (136° for Vickers), and d is the average length of the diagonals of the indentations. The average hardness number across all eight indentations was computed as 24.5. The average hardness number of Al6101 T6 is approximately 107 [123].

The low hardness value indicates a high concentration of defects within the struts, suggesting a reduction in the material's overall yield stress. This reduction occurs because defects act as stress concentrators, facilitating the initiation and propagation of

micro-cracks under stress, thereby leading to the early onset of yielding on a global level.

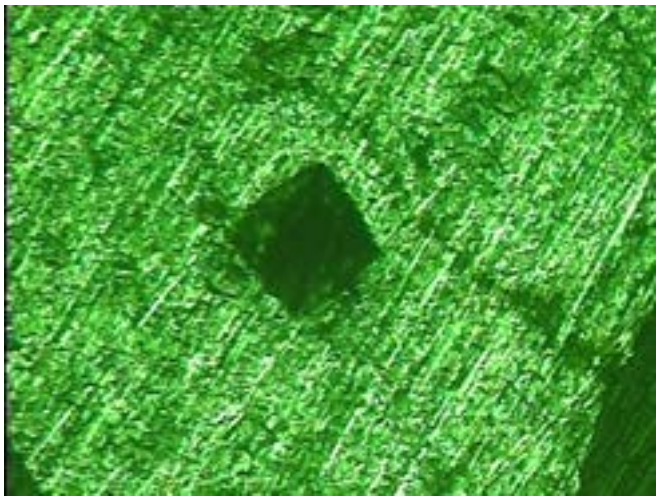

Figure 34: Vickers Hardness test on Al sample

Additionally, the low hardness number is not only a result of the defects but also of the small dimensions of the struts, which influence the material properties. The reduced dimensions can lead to size-dependent characteristics, where thinner struts exhibit lower mechanical properties compared to thicker ones due to surface effects and microstructural constraints [87].

6.2.4.5 Quasi-static compression

Both coated and uncoated aluminum foam samples were tested using quasi-static compression to determine their mechanical properties, namely their Young's modulus, plateau stress, and densification strain. The measured properties are used to assess the effect of the coatings. The quasi-static compression tests were conducted at a constant rate of 2 mm/min.

Force-displacement plots were recorded from the compression tests and converted to stress-strain curves. Loaded surfaces of all samples were polished before performing the compression tests. This process ensured the removal of any surface irregularities that might produce unnecessary noise, specifically at the start of the loading process. Surface imperfections can lead to misleading high initial stiffness measurements by causing an uneven distribution of the applied load. By polishing the

surfaces, the contact between the testing machine and the sample is ensured to be uniform, thereby minimizing the external variables that can affect the accuracy of the test results. From the stress-strain curves, Young's modulus and plateau stress were calculated. The plateau stress is determined at the point where the stress remains approximately equal while the strain is increasing. The densification strain is calculated at which point the plateau stress no longer remains relatively constant, specifically when it exceeds 100% of the initial onset of yielding that was recorded after the linear elastic phase. The densification strain can also be determined when the pores of the foam collapse completely. The energy absorption is calculated during the plateau phase (30-70% strain) and is compared to the energy absorbed during the last portion of the plateau phase (50-70% strain). The latter assists in evaluating the effectiveness of the coating at different stages of deformation.

Chapter 7: Results and Discussion

7.1 Results: Application of Metallic Coating on Metallic Foams

7.1.1 Numerical simulations on uniformly graded copper-coated aluminum foams – static and thermal

The computational methodology discussed above is used to obtain the effective elastic modulus, yield strength, and thermal conductivity of 20 hybrid copper-coated aluminum foam models. The models were generated by coating aluminum foams having 5 different relative densities (20%, 15%, 10%, 7%, 4%) using 4 coating configurations (no coating, 30 μm, 50 μm, and 100 μm thick copper coatings). The elastic and thermal properties of the aluminum and copper used in the models are listed in Table 4. Obtained elastic, yield, and thermal conductivity results are shown and discussed in the following.

7.1.1.1 Effective elastic, yield, and thermal conductivity experimental results

The effective elastic modulus of the hybrid foam models corresponding to aluminum foam substrates with the relative densities of 20%, 15%, 10%, 7%, and 4% are shown in Figure 35. The axis of abscissas in Figure 35 uses the relative density of the substrate aluminum foam (uncoated foam) to simplify the comparison. However, it should be noted that the relative density of the hybrid foams would be different (i.e., higher) than that of their aluminum substrate foam.

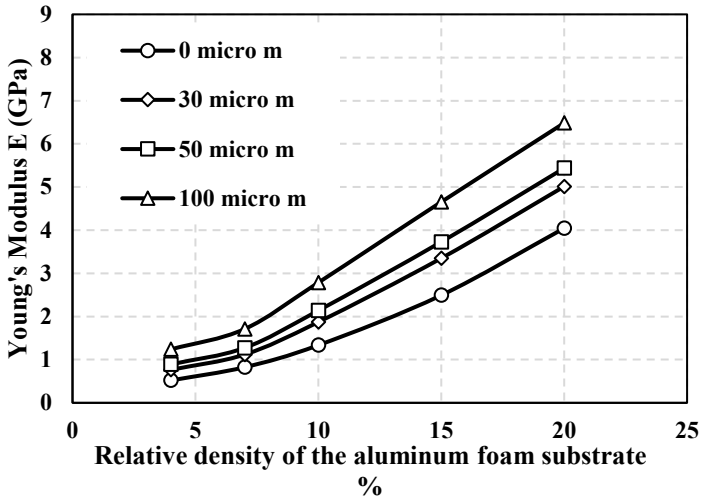

Figure 35: Effective elastic modulus of hybrid copper-coated foams, showing the effect of coating aluminum foam substrates having relative densities of 4, 7, 10, 15, and 20% with 30, 50, and 100 μm thick copper coatings

A strong positive correlation can be seen in Figure 35 between coating thickness and the stiffness of the hybrid foams, demonstrating the potential for increasing the stiffness of aluminum foams by coating them. The results show that the stiffness of copper-coated aluminum foams is more than two times that of uncoated aluminum foams in some cases. However, data in Figure 35 shows that the effectiveness of the applied coatings in increasing the stiffness of the hybrid foams is higher at lower relative densities. For instance, the stiffness of the hybrid foam with 30 μm thick coating is 47% and 23% higher than that of its aluminum substrate foam at 4% and 20% relative densities, respectively.

Similarly, the stiffness of the hybrid foam with 100 μm thick coating is 138% and 60% higher than that of its aluminum substrate foam at 4% and 20% relative densities, respectively. Coatings are more effective at lower relative densities as the surface area-to-volume ratio, which mathematically correlates with the reciprocal of the ligament's diameter, of the cylindrical ligaments comprising the substrate aluminum foam is higher at lower relative densities. Thus, the contribution of coatings to the overall stiffness response is higher at lower relative densities. With respect to coating thickness, thicker coatings result in higher stiffness values. For instance, at 4% and 20% relative densities, the increase in stiffness due to applying the 100 μm coating, as compared to the without coating case, is 2.93 and 2.52 times that caused by the 30 μm coating, respectively.

These results demonstrate that applying a coating, which is not difficult for metals and can be realized through simple electro-deposition processes, can potentially be used to tailor the elastic modulus of commercially available aluminum or metallic foams in general. This, in principle, agrees with the conclusions drawn in the literature [82], [90]. However, following this path to tailor the properties of aluminum foams involves a downside that cannot be ignored. Adding copper coatings or metallic coatings, in general, increases the overall weight and relative density of hybrid-coated foams. For instance, in the analyzed models, applying the 30 μm coating to the aluminum foams with relative densities of 4% and 20% increased their weight by 66% and 30%, respectively. On the other hand, applying the 100 μm coating to the aluminum foams with relative densities of 4% and 20% increased their weight by 221% and 99%, respectively. Evidently, the increase in weight and relative density associated with applying coatings is significant and should be considered in the design process of coated hybrid foams. If the open-cell foam was coated with an additional aluminum layer

instead of the applied copper coating, the enhancement in Young's Modulus would remain evident as the additional layer enhances the stiffness. However, the Young's Modulus of copper as a constituent material, as modeled from the properties shown in Table 4, is 1.72 times higher than that of aluminum, which suggests a higher enhancement in the stiffness of the open-cell foam at the expense of the added weight between copper and aluminum. To this end, Figure 35 is re-plotted in Figure 36 after normalizing the stiffness values by the hybrid foam's mass. Accordingly, Figure 36 represents the specific stiffness of the hybrid foam models.

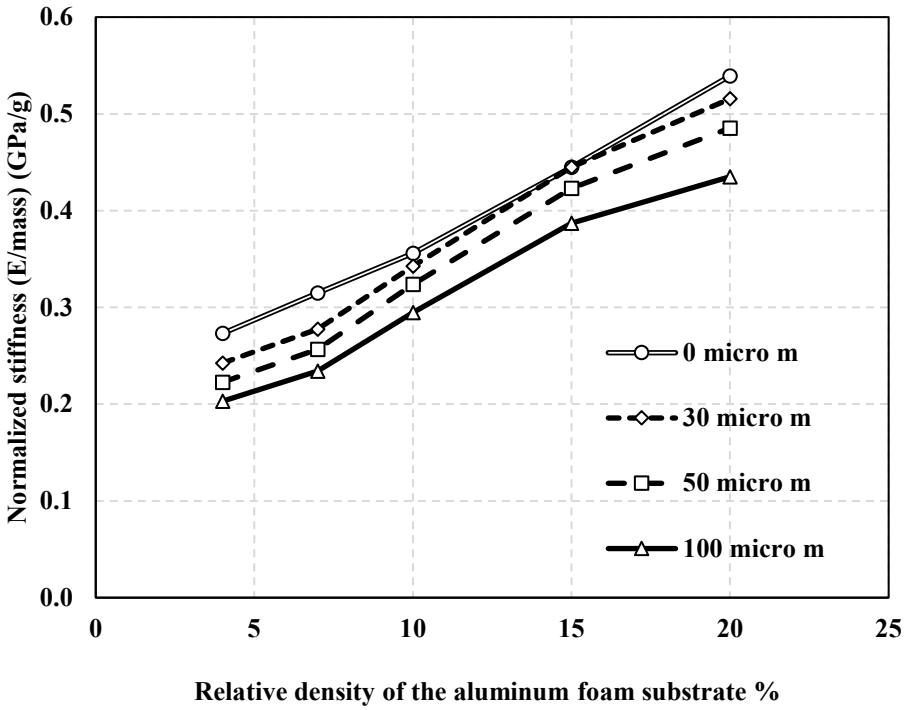

Figure 36: Normalized elastic modulus of hybrid copper-coated foams, showing the effect of adding coating on the stiffness-to-mass ratio

Applying thicker coatings, according to Figure 36, generally results in a lower stiffness-to-weight ratio. Such behavior can be perceived negatively by industries and applications that aim to minimize weight. Copper coatings increase the stiffness-to-weight ratio as copper's stiffness is approximately 1.6 times that of aluminum, but its density is approximately 3 times that of aluminum. So, copper coatings represent reinforcements that are marginally stiffer but significantly heavier than aluminum. Specific stiffness lines in Figure 36 almost follow a linear monotonous trend, indicating

that, within the investigated range of relative densities, applying a coating will always be associated with a decrease in the stiffness-to-weight ratio.

Similar to stiffness, applying the copper coatings increased the yield strength of the hybrid foams, but to a lesser extent than stiffness. Yield strengths obtained from the analyzed hybrid foam models are shown in Figure 37.

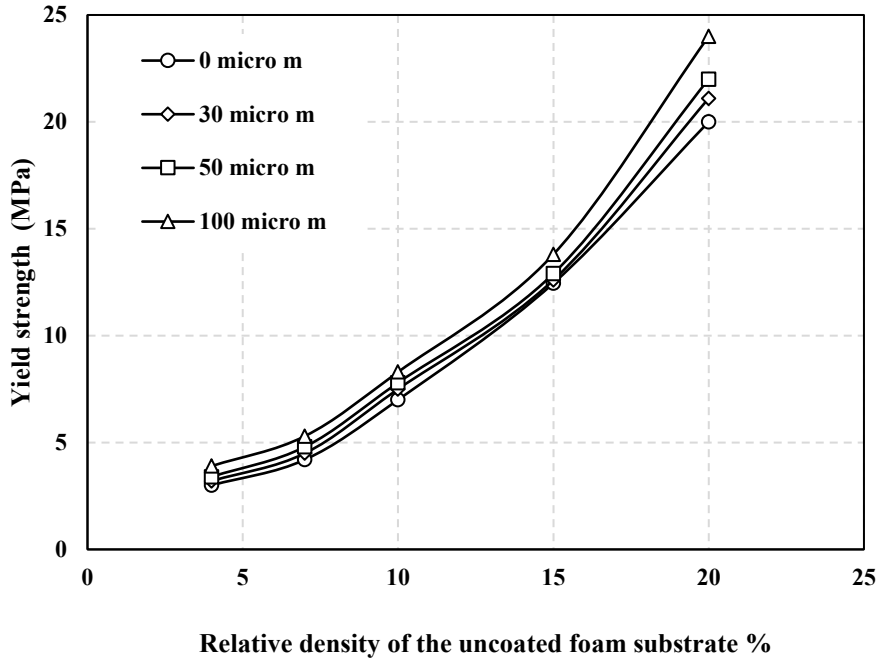

Figure 37: Yield strength of the hybrid copper-coated aluminum foams, showing the effect of coating aluminum foam substrates having relative densities of 4, 7, 10, 15, and 20% with 30, 50, and 100 µm thick copper coatings

Compared to the case without coating, the absolute yield strength values of the hybrid foams are slightly higher. In terms of relative change, the effect of coating is generally more pronounced at lower relative densities. For example, the yield strength of the hybrid foam with 100 µm coating is 30% and 20% higher than that of its aluminum substrate foam at relative densities of 4% and 20%, respectively. Similar to stiffness, according to Figure 37, hybrid foams with thicker coatings exhibit higher yield strengths. For instance, at 4% and 20% relative densities, the relative increase in yield strength due to the 100 µm coating, as compared to the case without coating, is 4.5 and 3.6 times that caused by the 30 µm coating, respectively. To evaluate the effectiveness of the coatings in increasing the yield while accounting for the associated

weight cost, the normalized yield strength (i.e., yield normalized by mass) data is plotted in Figure 38.

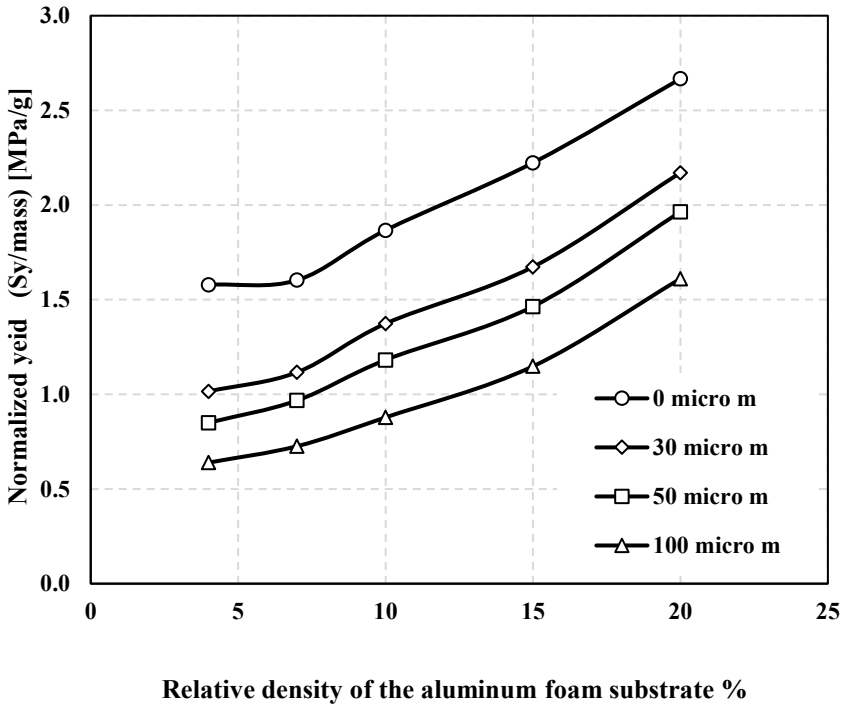

Figure 38: Normalized yield strength of the hybrid copper-coated foams, showing the effect of adding coating on the yield strength-to-mass ratio

According to Figure 38, the hybrid copper aluminum foams, as compared to their aluminum substrate foams, have substantially lower yield-to-weight ratios. This is evident at all used relative densities and coating thicknesses. The normalized yield lines of the hybrid models in Figure 38 increase approximately in a monotonic manner with increased relative density, and they shift downward, almost uniformly, with increased coating thickness. The largest relative drop in the yield-to-mass ratio is observed when the thickest copper coating is applied to the aluminum foam with the lowest relative density. The yield-to-mass ratio of the hybrid foam with 100 μm copper coating and aluminum foam with a relative density of 4% is 59.5% lower than that of its aluminum foam substrate.

The thermal conductivity values of the hybrid copper aluminum models are shown in Figure 39. Due to the superior heat conductivity of copper as compared to aluminum, hybrid foams exhibit higher thermal conductivities that increase with increasing coatings' thickness. The addition of copper coatings enhanced the thermal conductivity by more than twofold compared to uncoated aluminum foams. For

instance, at the lowest relative density considered (4%), the thermal conductivity of the hybrid foams with 30, 50, and 100 µm thick coatings is higher than that of their aluminum substrate foam by 60%, 99%, and 196%, respectively. Conducting a similar assessment at the highest relative density considered (20%) shows that the thermal conductivity of the hybrid foams is higher by 16%, 27%, and 53% than the thermal conductivity of the uncoated aluminum foam. So, the best improvement was observed at 4% relative density with 100 µm thick coating, while the lowest improvement was observed at 20% relative density with 30 µm coating.

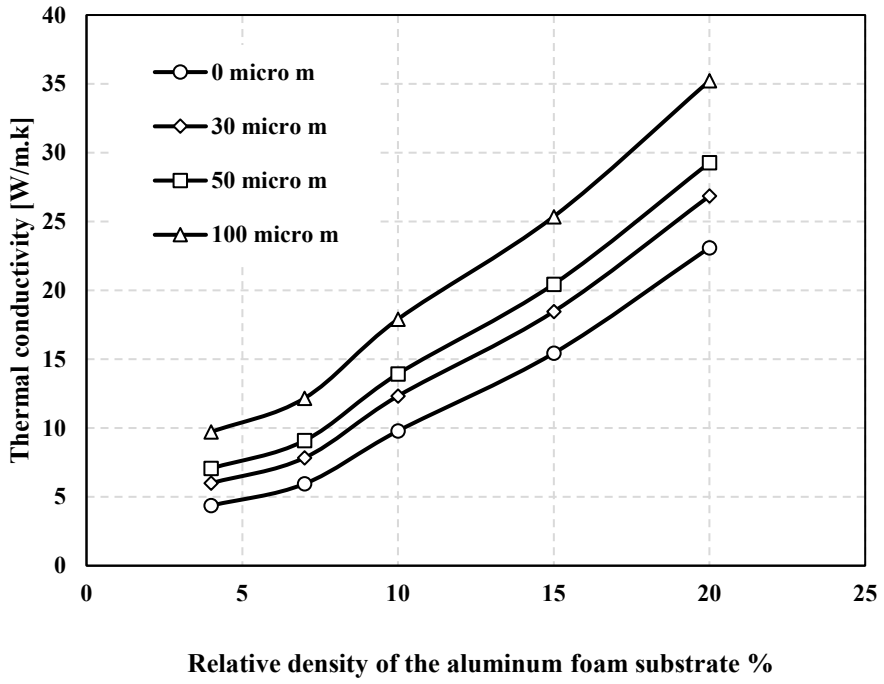

Figure 39: Thermal conductivity of hybrid copper-coated aluminum foams, showing the effect of coating aluminum foam substrates having relative densities of 4, 7, 10, 15, and 20% with 30, 50, and 100 µm thick copper coatings

These results support the feasibility of the efforts aiming to exploit copper coatings to tune and improve the thermal conductivity of commercially available open-cell aluminum foams [90]. To account for the weight drawbacks associated with adding copper coatings, the normalized thermal conductivities of the hybrid foams are calculated and plotted in Figure 40.

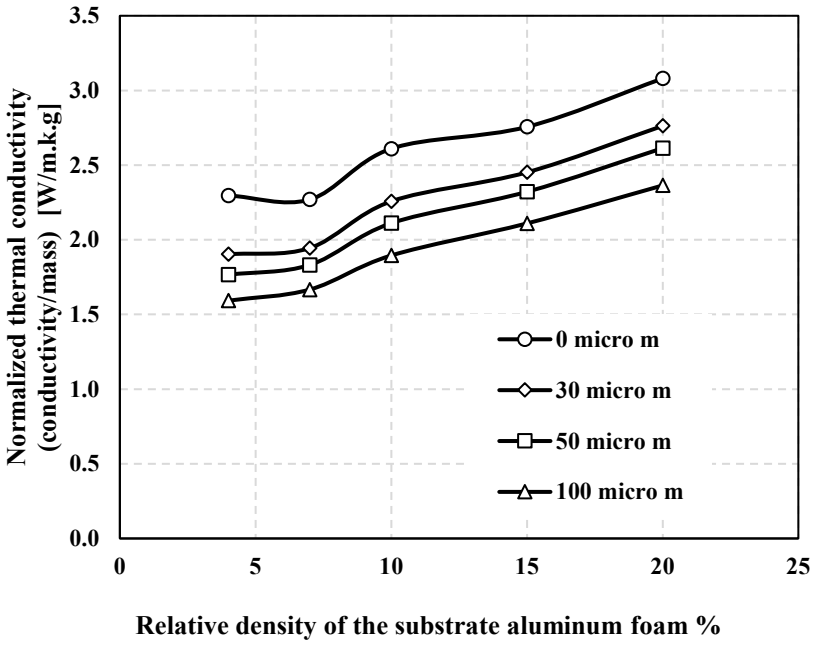

Figure 40: Normalized thermal conductivity of hybrid copper-coated aluminum foams

Figure 40 demonstrates that, though adding coatings improves the hybrid foams' thermal conductivity, increasing coating thickness systematically decreases the thermal conductivity-to-mass ratio. This means that the relative increase in thermal conductivity caused by a specific coating thickness is less than the accompanying relative increase in the foam's weight. The weight increase drawback is most observed at the lowest relative density considered. For instance, at the 4% relative density, applying 30, 50, and 100 μm thick coatings decreased the normalized thermal conductivity-to-mass ratio as compared to the uncoated specimen by 17, 23, and 30%, respectively. On the other hand, at the 20 % relative density, applying 30, 50, and 100 μm thick coatings decreased the normalized thermal conductivity-to-mass ratio as compared to the uncoated specimen by 10, 15, and 23%, respectively.

It is constructive to look at the aforementioned results from two perspectives: first, realizing tunable and improved elastic, yield, and thermal properties, and second, the cost associated with achieving tunable properties. Results support the efforts in the literature that proposed using hybrid copper aluminum foams to construct foams with tailored stiffness, yield, and, most importantly, thermal conductivity. The hybrid foams in this work exhibited a stiffness range of 0.52~6.48 GPa, a yield range of 1.08~14 MPa, and a thermal conductivity range of 1.73 and 35.22 W/m.k. These ranges are

much larger than those delivered solely by aluminum foams. Applying the copper coatings not only increases the range of achievable properties but also allows for tuning the properties by tuning the coating thickness. Tuning the latter is possible through controlling the current and time during electro-deposition processes [82]. By covering a wide range of relative densities and coating thicknesses, results provide an opportunity for optimizing the hybrid copper-aluminum foam tunable properties.

The primary cost associated with improving and tuning the elastic, yield, and thermal properties using coatings is the reduction in the hybrid foam-specific properties with increased coating thickness. However, the added weight can be justified for many applications. For instance, copper foams can provide higher thermal conductivity coefficients than aluminum foams, but they are heavier, more expensive, less commercially available, and exhibit smaller yield strengths. So, tuning the behavior of widely available aluminum foams using copper coatings can be more economically effective than using pure copper foams.

The results of this work can readily guide designers in selecting the parameters (i.e., the relative density of the aluminum foam substrate and coating thickness) required to realize a hybrid foam with certain stiffness, yield, or thermal conductivity. However, to maximize the benefits of this work, results are used in the next section to create semi-empirical models that can predict the behavior of hybrid copper-aluminum foams in specific and hybrid foams in general. These models can aid designers in selecting the parameters of copper-aluminum hybrid foams. Moreover, they can be used to predict the properties of hybrid foams made from different constituents (e.g., other than the copper or aluminum alloys considered in this work). The latter would shorten the development cycle of hybrid foams in general by minimizing the number of expensive simulations and experiments needed to determine their properties.

7.1.1.2 Empirical predictive models

7.1.1.2.1 Effective stiffness

To derive an empirical model capable of predicting the effective elastic modulus of hybrid foams, this work draws on established models that used tetrakaidecahedral cells to approximate the behavior of open-cell foams. Stochastic open-open cell foams bear great resemblance to tetrakaidecahedral tessellated structures, and therefore, they have been frequently represented by them in theoretical and computational-based studies [110], [124]. Predicting the effective elastic modulus of hybrid foams starts by

predicting their relative density. For tetrakaidecahedral foams with cylindrical struts, their relative density (R) can be defined as [124]

$$R = \frac{3}{8}\frac{\pi}{\sqrt{2}}\left(\frac{D^2}{L^2}\right) \tag{43}$$

where D and L are the struts' diameter and length, respectively. This equation can be reformatted as

$$\left(\frac{L}{D}\right)^2 = \frac{3}{8}\frac{\pi}{\sqrt{2}R} \tag{44}$$

Extending this equation to stochastic open-cell foams requires accounting for their randomness. To this end, Equation (44) is rewritten as

$$\left(\frac{L}{D}\right)^2 = \frac{B}{R} \tag{45}$$

here, B is a randomness-sensitive proportionality constant. This assumes that the nature of the relation between relative density and the average L/D ratio for stochastic foams is similar to that of tetrakaidecahedral foams; they only differ in the proportionality constant. The stiffness of tetrakaidecahedral foams ($\bar{E}$) with cylindrical struts were reported as [124]

$$\frac{1}{\bar{E}} = \frac{1}{6\sqrt{2}}\left[\frac{12L^2}{EA} + \frac{L^4}{EI}\right] \tag{46}$$

where E, L, and I are the modulus, length, cross-sectional area, and second moment of inertia of the struts, respectively. As the dominant deformation mechanisms in stochastic and tetrakaidecahedral foams are similar [1], [63], Equation (45) is expected to apply to stochastic foams. However, the constants in this equation, which relate to strut lengths and angles, should be recalibrated to account for the randomness of stochastic foams. To this end, Equation (46) is rewritten as

$$\frac{1}{\bar{E}} = \left[\frac{aL^2}{EA} + \frac{bL^4}{EI}\right] \tag{47}$$

where a and b are randomness-sensitive proportionality constants. Accordingly, the constants a and b can differ from sample to sample due to randomness. Still, the principal features in the equation, which relate to the dominant deformation

mechanisms in foams, remain unchanged. For the uncoated foam with cylindrical struts, the effective stiffness equation simplifies to

$$\frac{1}{\bar{E}} = \left[\frac{4a}{E\pi}\left(\frac{L}{D}\right)^2 + \frac{64b}{E\pi}\left(\frac{L}{D}\right)^4\right] \tag{48}$$

Using Equation (46) in Equation (48) results in

$$\bar{E} = \frac{\pi E R^2}{4a^* R + 64\pi b^*} \tag{49}$$

such that $a^* = aB$ and $b^* = bB^2$. Fitting Equation (49) to the data in Figure 35 (i.e., foam stiffness) results in $a^* = 1.496$ and $b^* = 0.01579$. The coefficient of determination for this fit is 0.9972. The quality of the obtained fit is shown in Figure 41. This figure shows excellent agreement between the effective stiffness obtained from the finite element models of the uncoated aluminum foam and Equation (49).

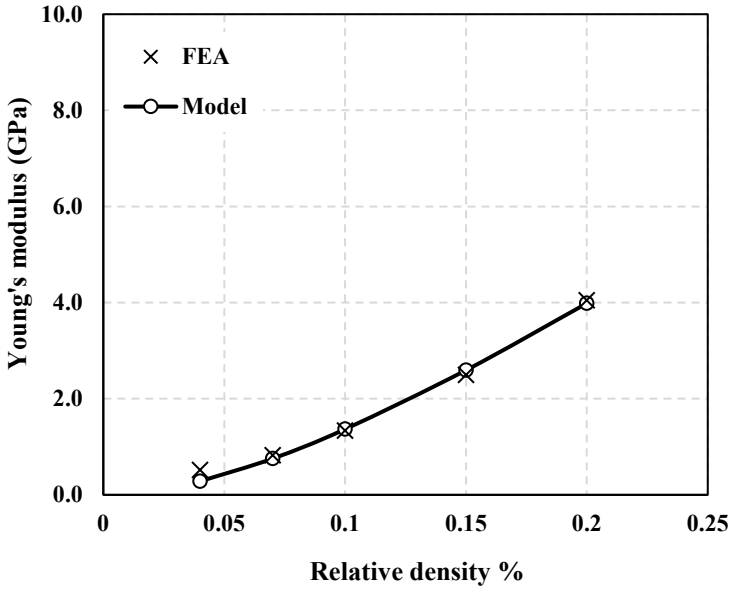

Figure 41: Effective stiffness of aluminum foam, showing a comparison between finite element analysis results (FEA) and Equation (49) (Model)

As the stochastic structure of both coated and uncoated foams are identical, the semi-empirical model Equation (49) can be extended using mechanics of materials principles to describe the stiffness of the hybrid copper-coated aluminum foams. Following mechanics of materials approach for handling composite cross-sections

[125], the coated cross-sections of the struts comprising the hybrid foams are converted to representative homogeneous ones.

This involved replacing the coating with an equivalent aluminum layer. For axial loading, the equivalent aluminum coating has an area of $f\pi Dt_c$, where f is the ratio of copper's modulus to that of aluminum (E_c/E_{al}) and t_c is the coating thickness. For bending, the equivalent aluminum coating has an elliptical shape as the coating is scaled by *f*, but only along the directional parallel to the applied moment. Applying Equation (48) to predict the effective stiffness of the coated foams leads to

$$\frac{1}{\bar{E}} = \left[\frac{aL^2}{EA_{composite}} + \frac{bL^4}{EI_{composite}}\right] \tag{50}$$

where E is the stiffness of aluminum. $A_{composite}$ and $I_{composite}$ are described as $A_{composite} = \frac{\pi D^2}{4} + f\pi Dt_c$ and $I_{composite} = \frac{\pi}{4}\left(\frac{D}{2} + t_c\right)^3\left(\frac{D}{2} + ft_c\right)$. If the coating thickness is defined in terms of the struts' diameter through a proportionality constant (k) as $t_c = kD$, then Equation (50) simplifies to

$$\frac{1}{\bar{E}} = \left[\frac{B}{\pi ER}\frac{a}{c} + \frac{bB^2}{E\pi mR^2}\right],$$

$$such\ that\ m = \frac{1}{64}(1+2k)^3(1+2fk)\ and\ c = \left(\frac{1}{4} + fk\right) \tag{51}$$

The values of k corresponding to the used coating thicknesses for all relative densities are listed in Table 7. Using a^* and b^* defined in Equation (49) to represent aB and bB^2 in Equation (51), respectively, simplifies Equation (51) to

$$\bar{E} = \left[\frac{cE\pi mR^2}{cb^* + mRa^*}\right] \tag{52}$$

This equation can describe the effective modulus of the coated hybrid foams using the empirical constants determined by simulating the behavior of uncoated specimens. The effect of coatings is accounted for through mechanics principles. Equation (52) was used to predict the effective modulus of all coated specimens investigated in this work. Predictions of Equation (52) are compared to the results obtained using finite element simulations in Figure 42.

Table 7: The values of thickness parameter k corresponding to coating thicknesses of 30 μm, 50 μm, and 100 μm.

		k		
Relative density of the aluminum substrate, R (%)	**Diameter, D (mm)**	$t_c = 30\ \mu m$	$t_c = 50\ \mu m$	$t_c = 100\ \mu m$
4	0.6	0.0500	0.0833	0.1667
7	0.705	0.0426	0.0709	0.1418
10	0.85	0.0353	0.0588	0.1176
15	1.06	0.0283	0.0472	0.0943
20	1.26	0.0238	0.0397	0.0794

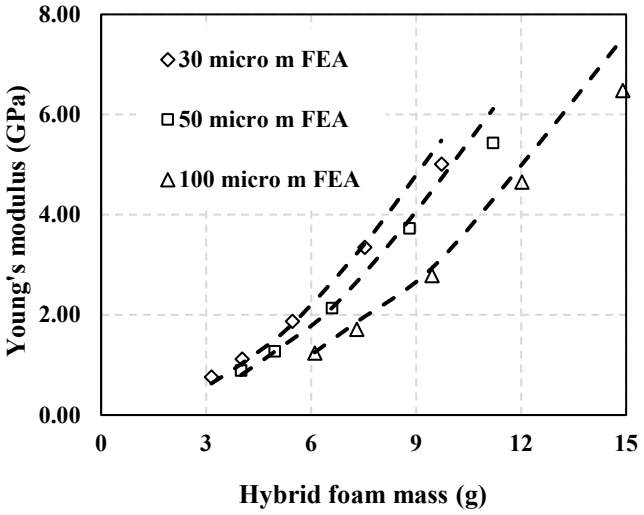

Figure 42: Predicted effective stiffness of hybrid copper aluminum foams, showing comparisons between finite element data (FEA) and predictions of Equation (51) (dashed lines)

In Figure 42, the predicted effective stiffness values, which are presented using dashed lines, are in good agreement with the finite element data, particularly at relative densities below 0.3 (equivalent to 12 g of mass). At higher relative densities, predictions of Equation (52) deviate slightly from the finite element data. The deviation can be traced back to the primary model Equation (46) adapted to derive Equation (52). This model assumes the deformation mechanisms of the struts to be driven completely by

bending and uniform axial internal loads. However, at higher relative densities, transverse shear and non-uniform loadings might affect strut deformation [126].

As Equation (52) does not account for transverse shear, it will be less accurate at higher relative densities (>0.3). However, from a practical point of view, this limitation wouldn't arise frequently as foams used in practical applications are of small relative densities (<0.15) [127].

7.1.1.2.2 Effective yield strength

To establish an empirical model capable of predicting the effective yield strength of hybrid foams, this work builds on the cubic cell-based yield model of open-cell foams [110]. The cubic cell model assumes deformation in the struts of open-cell foams to be dominated by bending. This assumption was shown experimentally [126] and numerically [63], [72] to be accurate at small relative densities (i.e., <20%).

Yielding of open-cell foams is assumed to occur when a plastic hinge is formed in their struts. Multiple hinges could co-exist at the moment of macroscopic yield (i.e., when the foam's stress-strain response shows yielding behavior).

The relation between the effective yield strength of an open-cell foam ($\bar{\sigma}_y$) and the cross-sectional critical bending moment (Mp) at the onset of plastic hinge formation in its struts is related according to the cubic cell model [110] as

$$\bar{\sigma}_y \, \boldsymbol{\alpha} \, \frac{M_p}{L^3} \tag{53}$$

where L is the struts length. This equation states that the macroscopic yield of open-cell foams is proportional to the plastic hinge internal moment. For the uncoated foam, the plastic hinge bending moment, assuming the strut constitutive behavior can be approximated as perfect elastic-plastic, can be computed as [110]

$$M_p = \int S_y^{al} \, y \, dA \tag{54}$$

such that S_y^{al} is the yield strength of the struts' constituent material, which is aluminum in this work, and y is the distance from the neutral axis.

Assuming a perfect elastic-plastic response is practical as it simplifies the derivation. In addition, it is sufficiently accurate as the relative change in the yield stress due to plastic hardening for both materials used in this work at small plastic strains is negligible. For a circular cross-section with a diameter (D), Equations (53) and (54) result in

$$\bar{\sigma}_y \, \boldsymbol{\alpha} \, S_y^{al} \left(\frac{D}{L}\right)^3 \tag{55}$$

Using Equation (44) in the previous equation leads to

$$\bar{\sigma}_y \, \boldsymbol{\alpha} \, S_y^{al} R^{1.5} \;\text{ or }\; \bar{\sigma}_y = A \, S_y^{al} R^{1.5} \tag{56}$$

The proportionality constant *A*, which is equal to 0.8025, is determined by fitting Equation (56) to the finite element-based yield data of the uncoated aluminum foams.

A comparison between the resulting fit and the finite element data is shown in Figure 43, which demonstrates excellent agreement. The R^2 value of the fit shown in Figure 43 is 0.998.

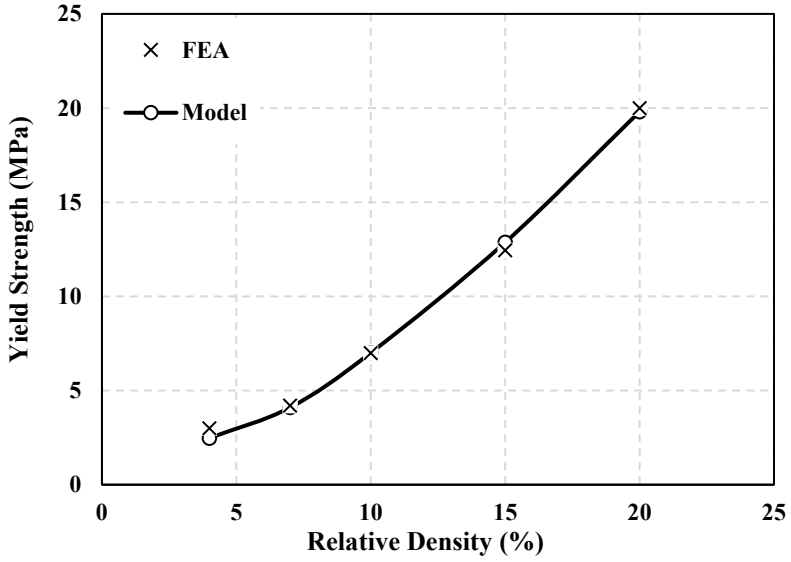

Figure 43: Yield strength of open-cell aluminum foams, showing a comparison between finite element data (FEA) and the semi-empirical model (Model) represented by Equation (56)

As the deformation mechanism and randomness of the coated foams are similar to those of their parent aluminum substrate, Equation (56) is extended to describe hybrid foams using mechanics principles. To this end, the integration performed to determine M_p is partitioned into two components to account for the composite cross-section of the struts comprising hybrid foams.

$$M_p = \int_{A_{al}} S_y^{al} \, y \, dA + \int_{A_{cu}} S_y^{cu} \, y \, dA \tag{57}$$

here, A_{al} and A_{cu} are the cross-sectional areas of the aluminum and copper phases, respectively. S_y^{al} and S_y^{cu} are the yield strength of the aluminum and copper phases,

respectively. Evaluating Equation (57), in conjunction with Equations (53) and (44), results in Equation (58), which is equivalent to Equation (56) but applies to hybrid foams.

$$\bar{\sigma}_y = A\left(S_y^{al} + S_y^{cu}[(1+2k)^3 - 1]\right)R^{1.5} \qquad (58)$$

The thickness parameter *(k)* appearing in this equation is defined in Table 7. The proportionality constant *(A)* is assumed to be identical to the one associated with uncoated foams Equation (56) as both coated and uncoated foams share the same stochastic properties.

To evaluate the effectiveness of Equation (58), the effective yield of the hybrid foams is calculated and compared to the finite element results in Figure 44.

The comparison shows good agreement, particularly at a relative density smaller than 0.3 (mass <12g). This is consistent with the inherent assumptions made in deriving Equation (58).

At large relative densities, deformation modes such as transverse shear accompany the dominant bending deformation mode. These additional deformation modes, though small, affect the foam's deformation and internal stress distribution and cause its behavior to deviate from that predicted by Equation (58). Nevertheless, the aforementioned deviations do not cause concern as most foams used in practical applications have small relative densities.

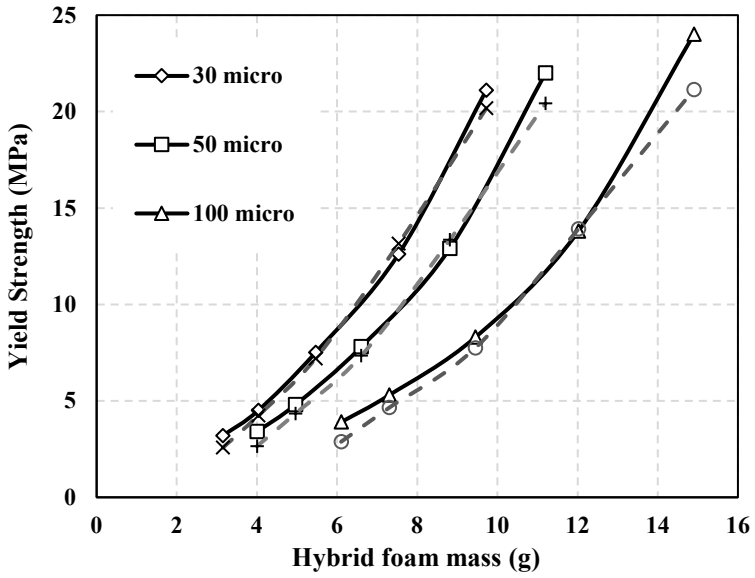

Figure 44: Predicted effective yield strength of hybrid copper aluminum foams, showing comparisons between finite element data (FEA) and predictions of Equation (58)(dashed lines)

7.1.1.2.2 Effective thermal conductivity

Estimating the effective thermal conductivity (ETC) of metallic foams, in particular for open-cell foams as they are used as heat exchangers in thermal management systems [23], [128], has acquired significant attention. This attention is exemplified by the numerous studies that established relationships between ETC of open-cell foams and their porosity, topological aspects of their inter-connected ligaments, constituent material, and fluid filling or flowing through their pores [129], [130], [131].

Such relationships are instrumental for designing and optimizing open-cell foams used in thermal management solutions. Developing mathematical models for predicting ETC of open-cell metallic foams mostly comprises three steps [85], [129], [130], [131], [132], [133]: identifying representative unit cells (e.g., tetrakaidecahedron or cubic), deriving a semi-empirical model through analyzing the thermal response of the unit cell, and calibrating the semi-empirical model using computational or experimental results.

The latter step is particularly important in accounting for the stochastic features corresponding to different types of open-cell foams. Most of the semi-empirical ETH models of open-cell foams (e.g., [131], [132]), which are derived using the aforementioned approach, can simplify algebraically to linear or quadratic porosity-dependent correlations of the following form if heat is assumed to transfer through them purely due to conduction.

$$k^{effective} = k_s \emptyset(\varepsilon) \tag{59}$$

Such that $k^{effective}$ is the ETC of the foam, k_s is the thermal conductivity of its constituent material, ε is the porosity, and $\emptyset(\varepsilon)$ is a weight that ranges between 0 and 1. The weight takes the form of a linear or second-order function. Applying Equation (59) to the results of the uncoated aluminum foams investigated in this work while using $k_{aluminum}$ for k_s, shows that a second-order weight function is sufficient to capture the response. The second-order weight is determined as

$$\emptyset(\varepsilon) = 1.318\varepsilon^2 - 1.812\varepsilon + 1.5062 \tag{60}$$

The correlation coefficients here account for the stochastic aspects of the modeled geometry. The R^2 value associated with the second-order fit is 0.998. Extending Equation (59) to capture the response of hybrid foams requires two modifications. First,

k_s should be represented by the homogenized heat conduction coefficient of the foam ligaments. Assuming heat transfer through the copper and aluminum layers comprising each ligament satisfy the parallel heat conduction criterion, then the homogenized heat conduction coefficient can be determined using the rule of mixture as

$$k_s = k_{aluminum}\frac{1}{(1+2k)^2} + k_{copper}\frac{(1+2k)^2-1}{(1+2k)^2} \tag{61}$$

where $k_{aluminum}$ and k_{copper} are the heat conduction coefficients of aluminum and copper, respectively, while k is the thickness coefficient defined in Table 7. Second, the porosity parameter in Equation (59) should account for the reduced porosity caused by the applied coatings. This can be achieved by using the common definition of porosity as one minus the volume ratio of the solid phase to total volume (i.e., cube in this work). For the cases with coatings, the aforementioned definition of porosity is simplified to

$$\varepsilon = 1 - R(1+2k)^2 \tag{62}$$

such that R is the relative density of the aluminum foam substrate and k is the thickness parameter defined in Table 7. Predicted ETC of the hybrid foams with 30, 50, and 100 μm thick coatings using Equation (59), along with Equations (60) ~ (62), are presented in Figure 45.

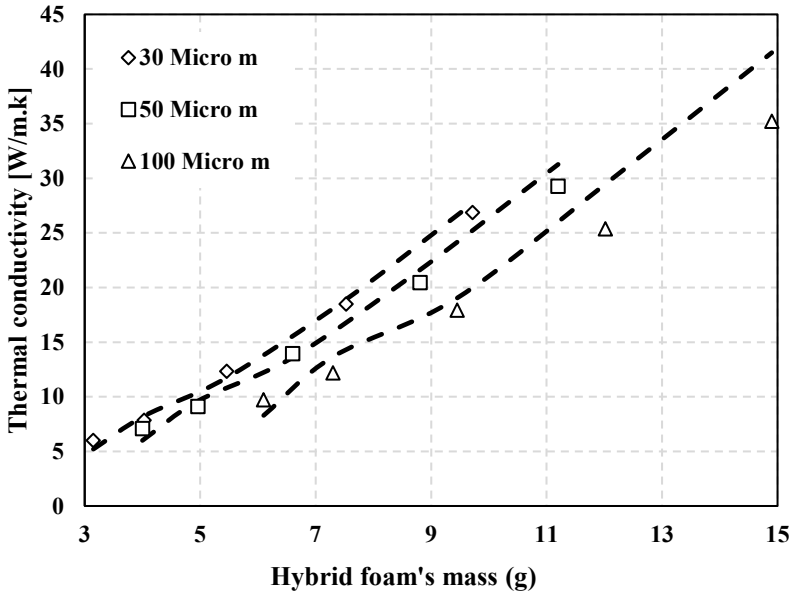

Figure 45: Effective thermal conductivity of hybrid foams, showing comparisons between finite element data (FEA) and predictions of Equation (58) (dashed lines)

Figure 45 shows good agreement between the ETC values predicted by Equation (59) and their counterparts determined using the finite element models. The deviation between the finite element results and ETC predictions is only visible in the case of 100 μm coating and at the largest aluminum foam relative densities (i.e., 0.15 and 0.2), which correspond to a total mass exceeding 11 g. In the latter case, the empirical model overestimated the ETC as it overlooks the effect of vertices at which the ligaments connect. The models consider the foam as a network of interconnected cylindrical ligaments that equally contribute to heat propagating across the foam. However, at higher relative densities and thicker coatings, a larger portion of the applied coating would be concentrated at the vertices. This portion would not participate in conducting heat as the model would anticipate.

The semi-empirical models of effective stiffness, yield, and heat conduction coefficients of open-cell hybrid-coated foams are simple and powerful. They can be calibrated using uncoated foams and subsequently used to predict the behavior of coated foams. This can substantially help in designing coated foams with application-tailored properties. Moreover, the semi-empirical models are independent of the constituent materials of both substrate and coating. Therefore, they can be applied to hybrid-coated foams comprising other constituents.

7.1.2 Numerical simulations on uniformly copper-coated aluminum foams – mechanical dynamic testing

The behavior of foams and cellular solids under dynamic crushing loads involves three phases: linear, plateau, and densification phases [1]. During the plateau phase, two mechanisms are present: localization and micro-inertia. Localization is related to the concentration of deformation in particular ligaments that eventually, due to excessive deformation, change their shape. As the excessively deformed cell walls move laterally or rotate, they induce resistive microinertia forces that increase in magnitude at higher deformation rates. Due to micro-inertia forces, the plateau strength of foams can increase at higher loading rates, even for foams made from a rate-insensitive constituent material. The plateau stage ends with densification, which is caused by the collapse of cell walls. Densification causes a sudden jump in the observed stresses. Results obtained in this work are consistent with the aforementioned behavior. Stress-strain curves obtained from the finite elements models using 30 μm, 50 μm, and 100 μm thick copper coatings are shown in Figure 46. The stress-strain curves clearly

show the commonly observed three deformation phases (i.e., elastic, plateau, and densification). Results show substantial improvements in the plateau strength. Adding a 100 µm thick copper coating almost doubled the plateau strength. However, to make the comparison more meaningful, the stress in Figure 46 should be normalized by the overall density of the corresponding model. This normalization is important to account for the increase in mass due to applying a coating. In principle, one would aim to realize higher strength-to-weight ratios by applying coatings. Normalizing the stress by the density of the foam resulted in the specific stiffness.

Increasing the copper thickness changes the average spacing between cell walls and increases the foam's relative density. Adding 30 µm, 50 µm, and 100 µm thick copper coatings increased the mass of the composite foam from 5.6 g to 7.53 g, 8.81 g and 12.02 g, respectively. Comparing the mass of the foam post-coating to its pre-coating mass shows a substantial increase in mass. 100 µm almost doubles the mass of the pre-coated foam.

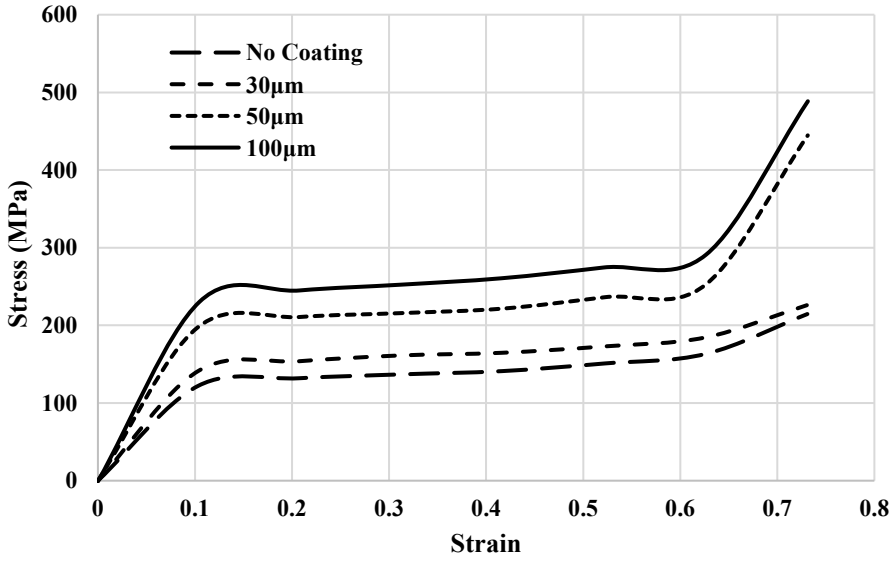

Figure 46: Stress-strain curves of coated open-cell aluminum foam, showing the effect of increasing coating thickness

The substantial increase in mass is related to the high density of copper, which is roughly 3 times that of aluminum. So, to capture the effect of copper coating, specific mechanical properties are of interest. Results shown in Figure 46 are normalized by

dividing the stress by the corresponding foam density. Resulting specific stress-strain curves are presented in Figure 47.

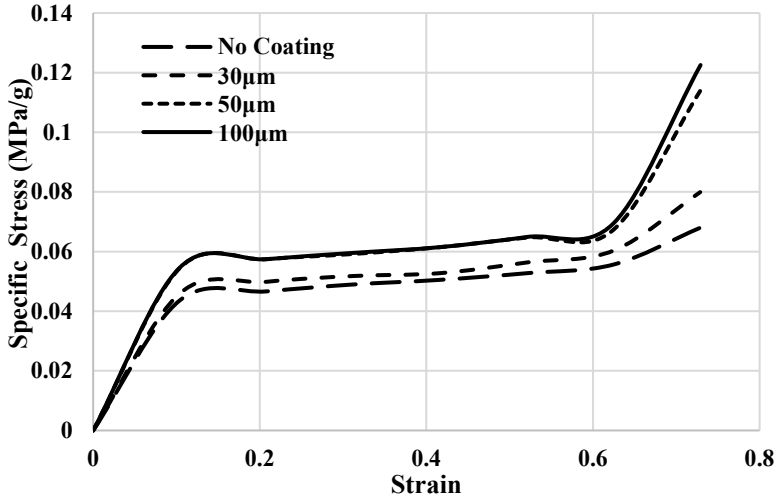

Figure 47: Specific stress-strain curves of coated open-cell aluminum foams, showing the effect of increasing coating thickness

Contrary to Figure 46, Figure 47 shows that applying a coating does not always improve the plateau strength. For instance, applying a 30 µm copper coating decreased the specific plateau stress slightly. On the other hand, Figure 47 shows that using 50 µm and 100 µm thick copper coatings improved the specific plateau stress by the same amount (10%). Thus, using 50 µm thick copper coating would be better than using 100 µm thick copper coating; 50 µm coating would result in less cost and weight.

So, if the density of the foam post-coating is not taken into account, the relationship between the plateau stress and coating thickness would appear proportional. To further analyze the mechanical properties, the energy absorption and energy absorption per density (i.e., specific absorbed energy) were calculated by numerically integrating the area under the stress-strain curves of Figure 46 and Figure 47, respectively. Integration was performed using the trapezoidal rule of integration. Both energy absorption capacity and specific energy absorption capacity are shown in Figure 48.

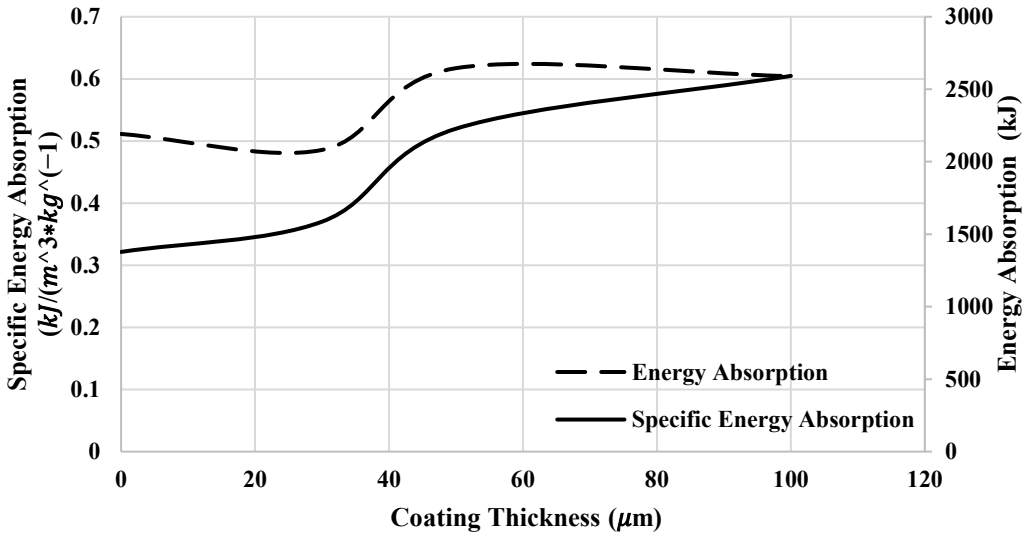

Figure 48: Coating thickness effect on energy absorption capacity and specific energy absorption capacity

As energy absorption is defined as the area under the stress-strain curve, it increases with both increasing the overall deformation (i.e., densification strain) and increasing the plateau strength. Applying copper coatings did not affect the densification strain substantially but affected the plateau strength. So, coatings are expected to affect the foam's overall energy absorption capacity. Figure 48 shows that adding coatings increased the energy absorption capacity of the composite foam.

However, in terms of specific absorbed energy, adding a 30 μm thick coating decreased the foam's ability to absorb energy. On the other hand, 50 μm and 100 μm coatings increased the specific absorbed energy capacity of the foam by the same level.

Based on the range of coating thickness used, 50 μm coating delivers the maximum enhancement; it maximizes the specific plateau stress and the specific energy absorption capacity. Copper-coating porous structures can be used as a tool to tailor specific mechanical properties of the foam without having to compromise on the degree of porosity. To shed light on the deformation patterns in the cell walls of the coated foams, the stress contours were obtained from the simulations and are presented in Figure 49.

The stress contours and deformed shapes are presented at the strains of 0%, 20%, 40% and 70%. The stress contours show that applying the copper coatings reduced the

stress concentrations observed in the pre-coated foam. Moreover, the deformation mechanisms driving the plateau stress are evident at 20% and 40% strain levels.

Here, localization and cell collapse are evident. Finally, at 70% strain, densification is observed in all cases, as shown in Figure 49. However, at all strain levels, applying a coating reduced the maximum observed stresses. Thus, one can delay ligament failure or rupture by applying coatings.

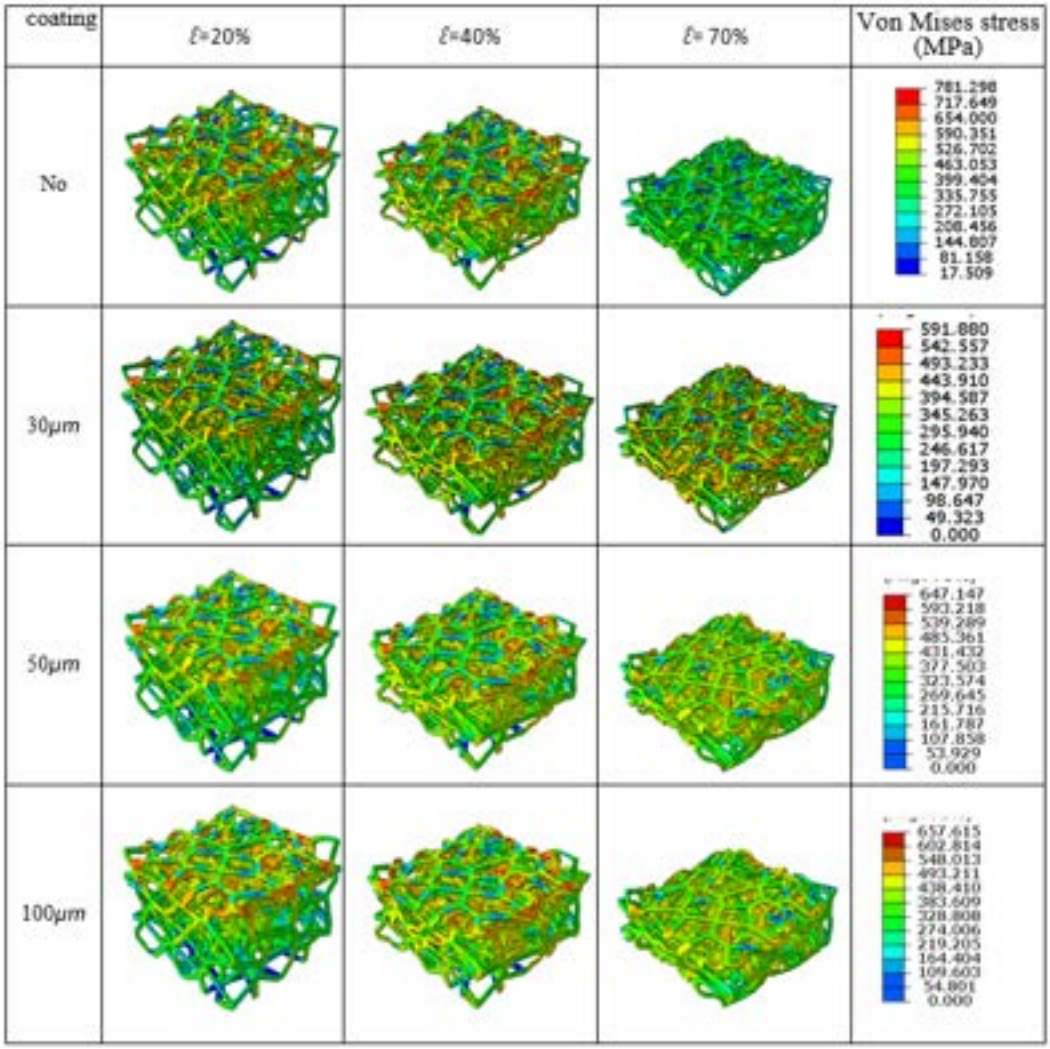

Figure 49: Deformation and stress contours of coated open-cell aluminum foam at different strain levels

7.1.3. Experimental testing on functionally graded copper-coated aluminum foam – static testing

The coated foam samples, electrodeposited at different times, were subjected to uniaxial compression, and the stress-strain diagrams for all samples are shown in Figure 50. The uncoated aluminum samples show slight variation in Figure 50a as the samples were not subjected to different electrodeposition times. On the other hand, the samples that were electrodeposited for 3600 s and 9000 s show the highest variations, while the samples with 5000 s electrodeposition time show the least variation.

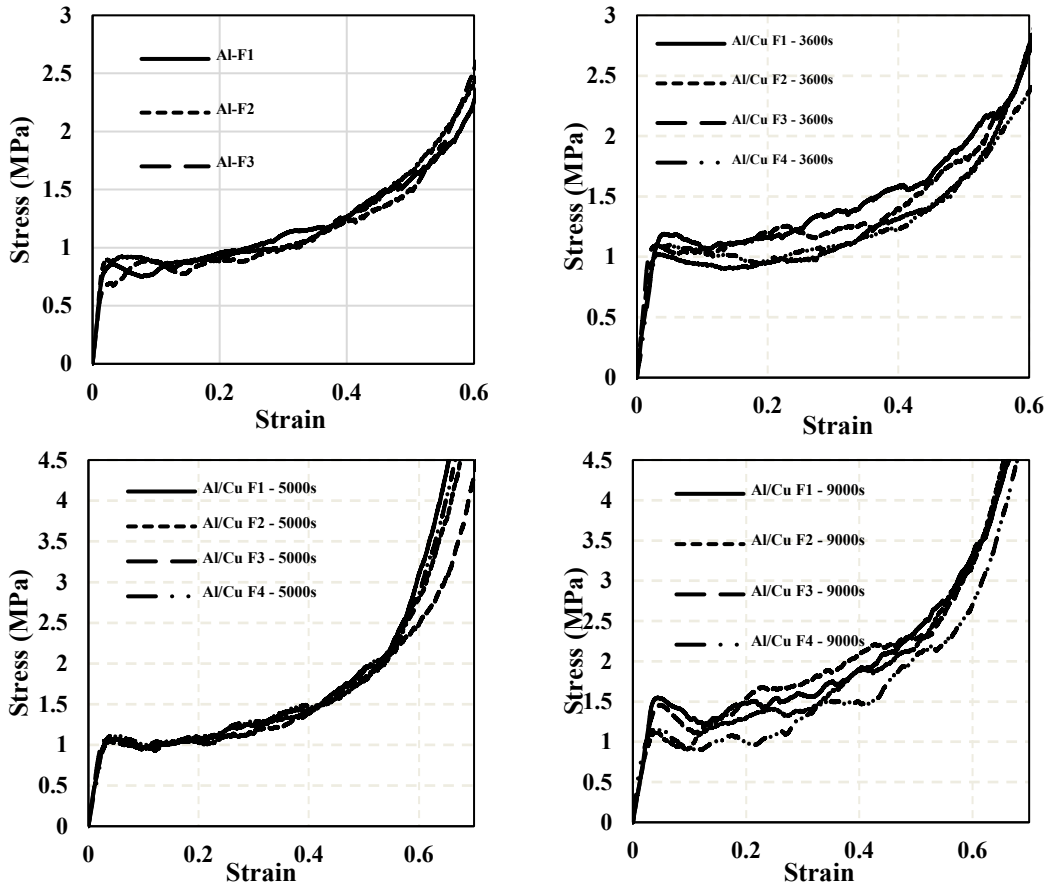

Figure 50: Stress-strain plots of coated and uncoated samples

Four samples were coated at different times to ensure the repeatability and reliability of the coating process. The low variability among these samples within each set (3600 s, 5000 s, and 9000 s) indicates that the copper coating significantly enhances the mechanical properties of the aluminum foam, and the process produces consistent results. To properly assess the reliability and consistency of the obtained results, Table

8 shows the percentage difference between samples of the same set based on the yield stress.

From the percentage difference in the plateau stress for each set of samples, it is evident that the least variation occurs in the uncoated samples, showcasing the high degree of repeatability. The percentage difference is relatively small, where the highest percentage difference is recorded between F1 and F3 at -4.74%. This consistency suggests that the manufacturing process of the obtained foam samples is reliable and produces samples of consistent mechanical properties across different samples. However, when the samples are coated, there is a change in the variability of the mechanical results.

The percentage difference increases up to 25.67% for samples coated for 3600 s, showing the variability in the mechanical properties of coated samples. These variations can be attributed to several factors, including the interactions of the electrodeposition process with the stochastic foam nature. Similarly, the samples that were coated for 9000 s show a variability in the yield stress up to -27.82%. On the contrary, the 5000 s set of samples shows a maximum of 6.39% difference in the yield stress, indicating a reliable and consistent electroplating process for the samples coated for 5000 s. The inherent randomness of stochastic foam structures contributes significantly to the observed variations. The obtained foam samples are characterized by irregular and random pore sizes, shapes, and distributions. This randomness affects the electroplating process for each sample, thereby leading to variation in the coating distribution. Even though the experimental setup remains consistent, the unique morphology coupled with aluminum defects on the struts results in a slight variation in the mechanical properties after coating.

Despite the inherent complexity of achieving consistent coating results with electrodeposition, the variation in the yield stress between the samples is not excessively high. The percentage difference within each indicates reasonable repeatability and reliability in the electroplating process. For instance, for the 5000 s coated samples, the percentage difference is low, such as -3.34% between F1 and F2. Similarly, for the 9000 s coated samples, the difference between F1 and F1 is just 1.13%, and for the 3600s set, the difference between F1 and F3 is 6.13%.

Table 8: Percentage difference of yield stress between samples of the same set.

Set	Comparison	Percentage Difference (%)
Uncoated Samples	F1 vs F2	1.08
	F1 vs F3	-3.71
	F2 vs F3	-4.74
3600s	F1 vs F2	20.83
	F1 vs F3	6.13
	F1 vs F4	-10.20
	F2 vs F3	-12.16
	F2 vs F4	-25.67
	F3 vs F4	-15.39
5000s	F1 vs F2	-3.34
	F1 vs F3	-2.43
	F1 vs F4	2.84
	F2 vs F3	0.94
	F2 vs F4	6.39
	F3 vs F4	5.39
9000s	F1 vs F2	-14.98
	F1 vs F3	1.13
	F1 vs F4	-26.99
	F2 vs F3	18.94
	F2 vs F4	-14.14
	F3 vs F4	-27.82

Key mechanical properties that govern the behavior of cellular material are calculated, which include the densification strain, plateau stresses, energy absorption between 0 and 70% strain, and 30 to 70% strain. The results from each set are then averaged out to provide a comprehensive view of the impact of functionally graded coatings on the mechanical properties of stochastic foams.

7.1.3.1 Elastic modulus

The elastic modulus of the coated and uncoated sample is presented and analyzed in this section. A total of four samples were coated for each set of electrodeposition times to ensure repeatability and reliability of the achieved results. The elastic modulus

is calculated from the stress-strain plots shown in Figure 50 and was averaged to provide a single representation value for each electrodeposition time in Figure 51. The error bars in the chart reflect the standard deviation, highlighting the variability within each set of samples. From the obtained results, the uncoated samples exhibited the highest average elastic modulus of 51.66 MPa. It is evident from the uniaxial compression tests that as the electrodeposition time increases, the average elastic modulus decreases. Specifically, at 3600 s, the average elastic modulus was calculated to be 46.5 MPa. This is then followed by a further decrease for the 5000 s and 9000 s samples, where the elastic modulus decreased to 41.91MPa and 46.25MPa, respectively.

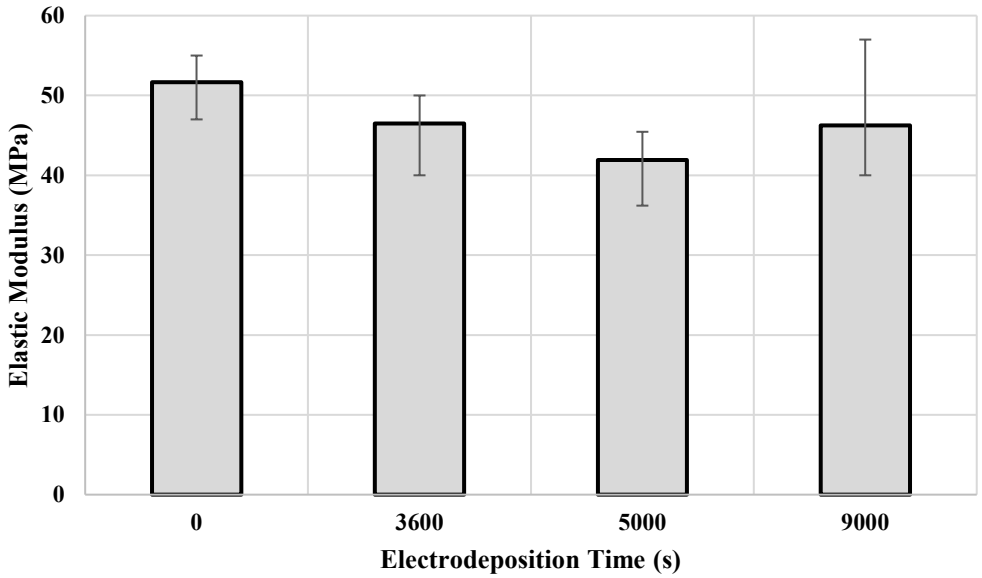

Figure 51: Effect of functionally graded copper-coated aluminum foam on elastic modulus

While the 9000 s set of samples showed a slight increase as compared to the 5000 s set of samples, the uncoated samples remained with the highest stiffness. This observed decrease in the elastic modulus with increasing electrodeposition time can be attributed to several factors, which include features related to the nature of the coating process as well as the overall morphological feature of the aluminum foam.

The higher electrodeposition time results in thicker copper coatings, resulting in higher yield stresses and increased hardness. Higher electrodeposition times also introduce significant defects and irregularities. Such defects introduce special nodes

that act as stress concentrators, which reduces the overall stiffness of the foam structure. On a microstructural level, the increased coating thickness introduces the accumulation of defects within the coatings. Such defects include dislocations, voids, and micro-cracks. The formation of such dislocations during the prolonged period of electrodeposition in an acidic solution is a response to the internal stresses generated within the material. Such stresses can arise due to the difference in the thermal expansion coefficient between the copper coating and the aluminum substrate, as well as the residual stresses from the electrodeposition process itself.

As the dislocation density increases with longer electrodeposition time, dislocations pile up at grain boundaries and other obstacles within the aluminum substrate. These pileups lead to localized stress concentrations, which reduces the ability of the material to deform elastically. This phenomenon of decreasing elastic modulus with increased electrodeposition times has been observed in other studies. For instance, in a study by Devivier et al. [82], the authors observed a decrease in the elastic modulus of nickel-coated aluminum foam due to the introduction of additional defects.

7.1.3.2 Plateau stress

The plateau stress is another critical parameter that is used to evaluate the mechanical performance of cellular materials, especially foams under compressive loads. The plateau stress is the region of the stress-strain curve in which the material undergoes significant deformation with minimal change in the stress. This parameter directly contributes to the energy absorption capabilities of the structure, which is important in applications of impact protection and cushioning, where the material needs to absorb energy efficiently while maintaining structural integrity. The plateau stress is calculated for each set of samples (0 s, 3600 s, 5000 s, 9000 s) and averaged out across all the specimens for each set, shown in Figure 52. The plateau stress values were averaged out to provide a representative value for each electrodeposition time, and similar to the elastic modulus bar graph, the error bars indicate the standard deviation, reflecting the variability within each set.

From Figure 52, the uncoated samples exhibited the lowest average plateau stress at 0.902 MPa. Contrary to the elastic modulus, the plateau stress observed a significant increase with increased electrodeposition time, where the average plateau stresses were calculated to be 0.995 MPa, 1.067 MPa, and 1.276 MPa for electrodeposition times of

3600 s, 5000 s, and 9000 s, respectively. The higher copper coating thickness results in a higher load-bearing capacity of the foam, thereby increasing the plateau stress.

On a microstructural level, while the defects are present in the aluminum foam, the electrodeposition process can aid in microstructural reinforcement. The deposited copper fills in surface irregularities and defects, which creates a more uniform structure. This uniformity improves the foam's ability to withstand compressive loads, resulting in higher plateau stresses. On a mesoscale level, the added copper layer increases in the second moment of inertia of the reinforced ligaments, which further enhances their load-bearing capacity through flexural yielding. The enhanced moment of inertia results in higher bending resistance, thereby leading to higher plateau stresses.

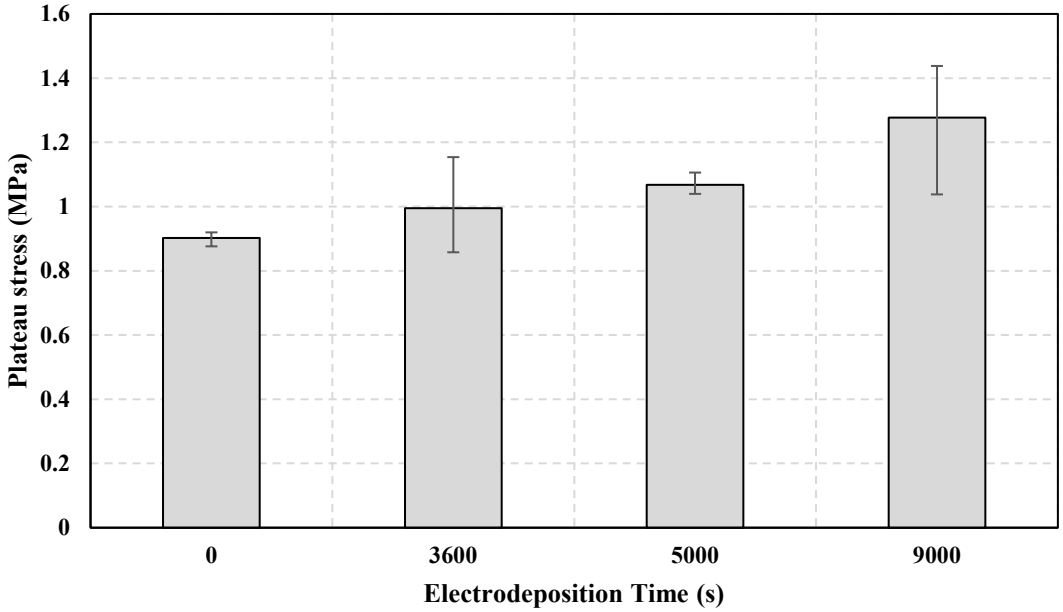

Figure 52: Effect of functionally graded copper-coated aluminum foam on plateau stress

7.1.3.3 Energy absorption

The higher plateau stresses observed in Figure 52 directly result in higher energy absorption capabilities. The plateau stress represents the stress level during the plateau region in the stress-strain curve, where the material undergoes significant deformation at minimal changes in the stress. This plateau region is important to the energy absorption capabilities as it indicates the material's ability to absorb energy through plastic deformation without collapsing. The area under the stress-strain curve, up to a certain strain level, represents the energy absorbed by the material. Therefore, a higher

plateau stress results in a larger area under the curve, thus a greater energy absorption. To properly assess the energy absorption capabilities of all the samples and analyze the effect of copper coating on aluminum foam, the energy absorption is calculated between strains of 0% to 70% and 30% and 70%. In the 0-70 phase, shown in Figure 53, this portion of deformation includes the initial elastic region, the plateau region, and the onset of densification, thereby highlighting the comprehensive measure of the material's capacity to absorb energy throughout the entire deformation process. The energy absorption between 30% and 70% strain, shown in Figure 54, isolates the energy absorption primarily in the plateau region, excluding the initial elastic response and early stages of plastic deformation. It is important to distinguish between both plots to understand the material's behavior under sustained loading conditions and its ability to absorb energy efficiently during prolonged deformations.

From Figure 53, the energy absorption increases significantly as the electrodeposition time. Specifically, the energy absorption increases from 1.0266 MJ/m^3 to 1.072 MJ/m^3, 1.21733 MJ/m^3, and 1.414 MJ/m^3 for electrodeposition times of 3600 s,5000 s, and 9000 s, respectively. On the other hand, when looking at the energy absorption between 30% and 70% strain, the energy absorption increases from 0.766 MJ/m^3 to 0.785 MJ/m^3, 0.911 MJ/m^3, and 1.050 MJ/m^3 for electrodeposition times of 3600 s, 5000 s, and 9000 s, respectively. The energy absorbed during the plateau phase is the highest region of energy absorption during the deformation process. The thickness and uniformity of the copper coating lead to substantial improvements in the energy absorption capabilities.

While there is a drop in the elastic modulus, as shown in Figure 51, the initial elastic phase deformation does not significantly contribute to the overall energy absorption capabilities. The percentage increase in energy absorption when comparing uncoated samples to coated samples is calculated to be significantly close, where the energy absorption up to 70% results in an increase of 4.42%, 18.58%, and 37.75% for 3600 s, 5000 s, and 9000 s coated samples respectively, as compared to the increase of 2.48%, 18.0% and 37.09% for 3600 s, 5000 s, and 9000 s coated samples, respectively.

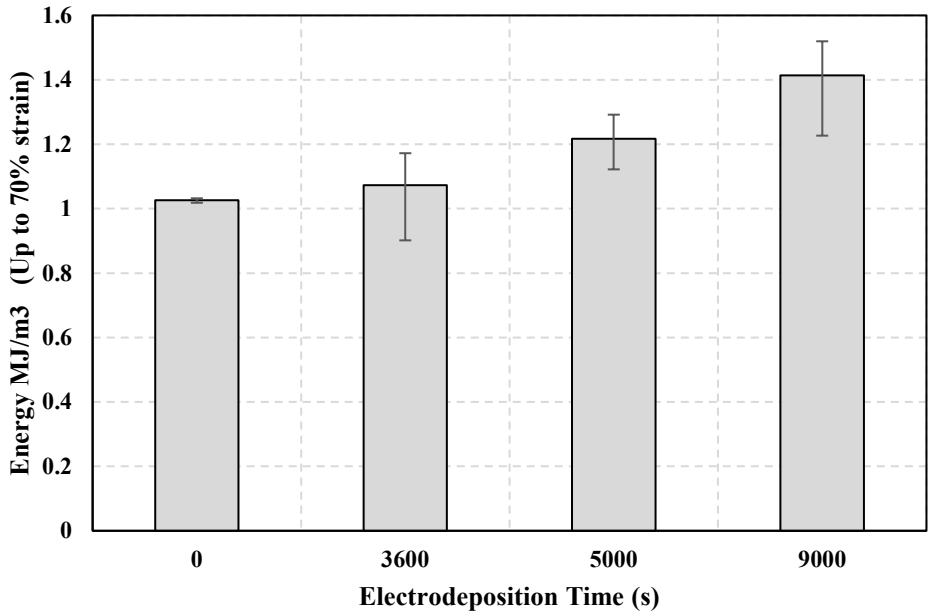

Figure 53: Effect of functionally graded copper-coated aluminum foam on energy absorption from 0% to 70% strain

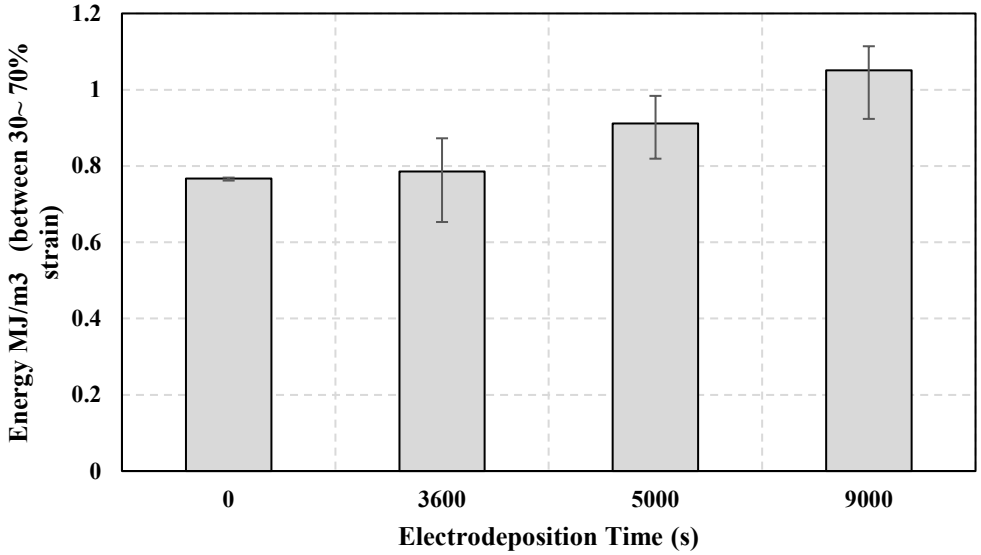

Figure 54: Effect of functionally graded copper-coated aluminum foam on energy absorption from 30% to 70% strain

There is a negligible difference between the percentages of enhancement in the two plots, which showcases that the initial elastic phase region does not significantly contribute to the overall energy absorption capabilities of the copper-coated aluminum samples.

Adding on, the energy absorption capabilities of the copper-coated aluminum foams are significantly influenced by the nature of the applied coating, which is thicker at the surface and gradually decreases as we move deeper into the sample. This gradient in coating thickness, across all dimensions (x,y,z), creates a functionally graded material where the properties vary continuously from surface to core. The outer regions of the foam, where the copper coating is thickest, contribute significantly to the initial energy absorption. Particularly, in the plot showing the energy absorption up to 70% strain, the thick coating at the surface enhances the initial resistance to deformation.

The gradient in coating thickness also allows for better load distribution as the deformation progresses. The thicker outer coating layer bears the most load initially, while the gradually thinner inner coating layers help to distribute the stresses more uniformly. This improved load distribution results in enhanced energy absorption capabilities in the plateau region, particularly in the region between 30% and 70% strain. In the 30% to 70% strain region, the energy absorption is due to plastic deformation, in which the functionally graded coating supports sustained deformation without high-stress concentrations. The transition from a thicker surface coating to a thinner coating creates a gradient that mitigates sudden changes in the mechanical properties, which reduces the likelihood of fracture, thereby contributing to higher plateau stresses under higher strain regions.

7.1.3.4 Densification strain

The densification strain is calculated for all sets of samples, which refers to the strain at which the material transitions from the plateau region, where the stress is nearly constant, to a region where the stress increases rapidly. This occurs when the cell walls of the foam completely collapse, and the material is compacted, increasing the relative density and, thereby, the stress. The region marks the end of effective energy absorption in the foam, where beyond this point, the material no longer efficiently absorbs energy but instead undergoes densification. In this region, the material's volume decreases significantly. The densification strains were determined as the point where the plateau stress exceeds 100% of the yield stress. This method ensures a consistent and objective measure of when the material transitions from the plateau region to the densification region. The densification strains are shown in Figure 55 for all sets of coated samples.

A high densification strain indicates that the material can absorb more energy before reaching densification, which is advantageous for applications where maximum energy absorption is required. A higher densification strain implies that the foam maintains the plateau stress over a larger deformation range.

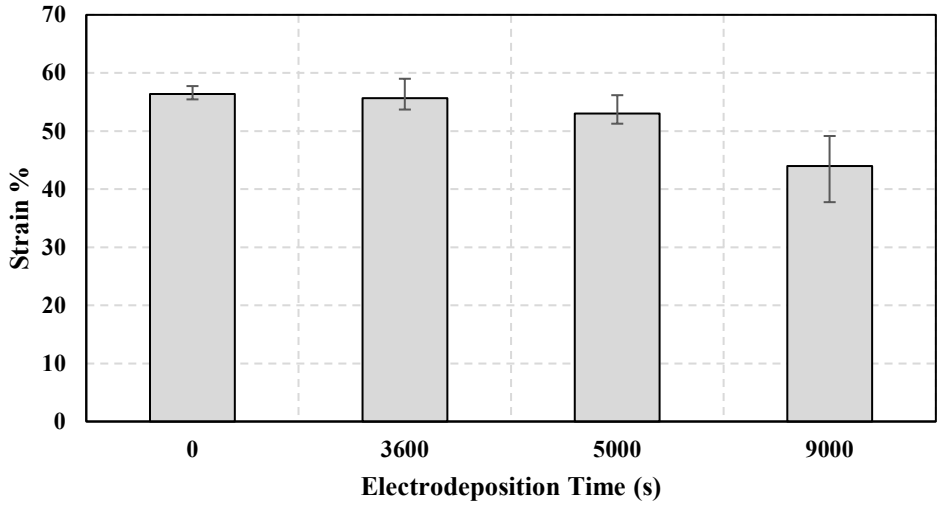

Figure 55: Effect of functionally graded copper-coated aluminum foam on densification strain

From Figure 55, the densification strains for the uncoated samples were calculated to be at 56.396% as compared to 55.675%, 53.031%, and 43.971% for electrodeposition times of 3600 s, 5000 s, and 9000 s, respectively. These values indicate a decreasing trend in the densification strain with increasing electrodeposition time. From a macroscale perspective, the addition of copper coatings, particularly in longer electrodeposition time (5000 s and 9000 s), results in earlier densification compared to uncoated samples. The increased overall rigidity, earlier portrayed in Figure 51, is due to the thicker copper coating that affects the foam structure, which can only sustain deformation up to a certain point before beginning to compact. The copper coating reinforces the foam's cell walls, thereby increasing their resistance to buckling.

For instance, in samples with shorter electrodeposition time (3600 s), the reinforcement contributes to a slight decrease in the densification strain due to enhanced structural support. However, with increased coating thickness, the enhanced stiffness strut leads to a more brittle response, resulting in an earlier transition to densification.

The functionally graded coating thickness, where the outer regions of the foam have higher coating thickness, results in stiffer outer layers that fail to deform plastically. Accordingly, the inner, less coated regions exhibit more localized deformation and reach their densification points faster, leading to overall lower densification strains.

The observed reduction in the densification strain with increased electrodeposition time suggests that while the coated samples were able to absorb energy effectively, they beings to compact and densify sooner. The earlier onset of densification in thicker coatings indicates that this higher plateau stress, achieved by higher coating thicknesses, is not sustained over larger deformation. This results in a trade-off between initial load-bearing capabilities and the ability to absorb energy over extended deformations.

7.2 Altering Topological Features of Honeycombs by Introducing Sinusoidal Perturbations

7.2.1 Out-of-plane compressive response

Under out-of-plane loadings, aluminum honeycomb cores fail mainly by yielding, elastic-buckling, or plastic-buckling. The large length-to-thickness ratio of their cell walls renders honeycomb cores prone to buckling instabilities and failure. However, their failure mode also depends on the loading area size and the number of cell walls carrying the load. Increased load sharing is associated with subjecting a larger area to the out-of-plane load (e.g., impact with larger objects), which lessens the probability of buckling and increases yielding. Therefore, before superposing perturbations to the conventional honeycomb core, it is essential to characterize its failure modes and their dependence on loading area size represented by the loading scenarios: 1 wall, 3 walls, 1 cell, and 3 cells. A simple procedure is used to determine the failure mode in the honeycomb core. This procedure compares the maximum local stress in the walls of the loaded honeycomb to the out-of-plane force applied. It aims to determine whether the onset of local yielding precedes the onset of buckling, which typically manifests as a softening in the out-of-plane load-displacement curve.

Figure 56 compares the local and structural behavior of the unperturbed honeycomb for the four loading scenarios representing loading area size. The applied out-of-plane force and the resulting out-of-plane displacement (i.e., displacement of nodes subjected to the out-of-plane force) are presented in Figure 56a. The local

response represented by the evolution of the maximum normalized stress observed in the cells of the unperturbed honeycomb is shown in Figure 56b. The maximum normalized stress is defined as the ratio between the maximum Von Mises stress and the yield strength of the cell walls' constituent material. The maximum normalized stress attains a value of 1 at the start of cell wall yielding.

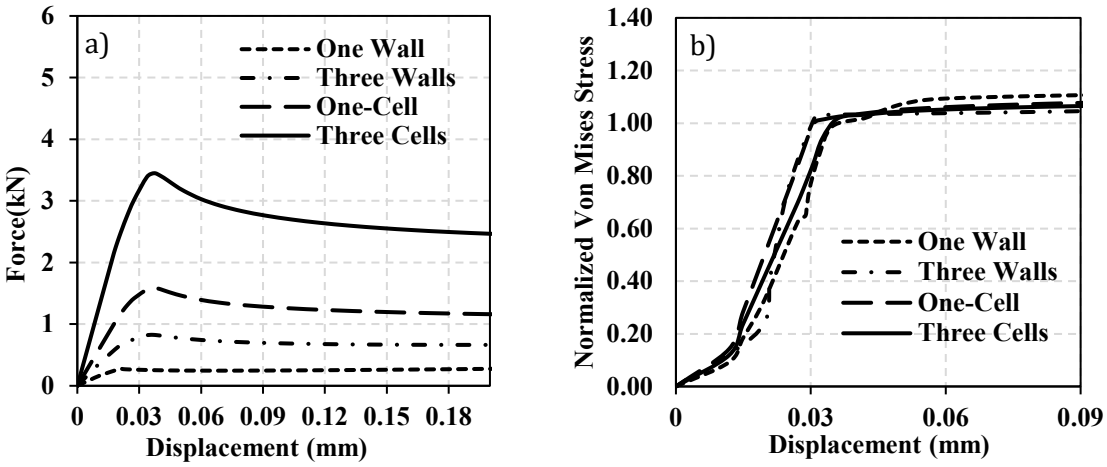

Figure 56: Out-of-plane response of the unperturbed conventional honeycomb core, showing a) its out-of-plane force-displacement response and b) the maximum stress observed in its cell walls

Based on Figure 56a, the onset of softening in the out-of-plane load occurs at an out-of-plane displacement between 0.035mm and 0.4mm for the loading scenarios of three walls, one cell, and three cells and occurs at the ~0.02 mm displacement mark for the loading scenario of one wall. However, the maximum normalized stress presented in Figure 56b demonstrates that local yielding, regardless of the impact area size, commences at a displacement between 0.03 mm and 0.035 mm. Accordingly, for the single wall-loaded scenario, elastic buckling preceded yielding. In contrast, for the rest of the loading scenarios, local yielding coincided with or preceded the onset of softening, highlighting a plastic buckling failure mode. Accordingly, only highly concentrated out-of-plane loads (i.e., concentrated on a single wall) can give rise to elastic buckling in the considered honeycomb core.

Imposing perturbations significantly affected the honeycomb's force-deflection response, failure characteristics, and load-carrying capacity. To highlight this effect, Figure 57 compares the global force-deflection response to the local stress evolution at the cell wall level for the case with the perturbation parameters of A = 0.33 mm and n = 4, which is the case with the highest perturbation amplitude and frequency. According

to Figure 57a, load softening is not observed in all loading scenarios, and the load transitions from a linear phase to a plateau phase in a smooth manner, suggesting the absence of elastic or plastic buckling and highlighting the effectiveness of the superposed perturbations in driving the cell walls to yield rather than buckle. The local behavior shown in Figure 57b shows monotonic behavior that starts with a linear phase and transitions smoothly to a plateau phase. Accordingly, load softening in the perturbed case was not observed in its behavior at the local (i.e., cell walls) and global (i.e., force-displacement) length scales. Figure 57b shows that local plastic deformation in cell walls commences slightly after the 0.03 mm displacement mark, which is consistent with the results presented in Figure 56b. Cell walls in the case with the least concentrated force, i.e., three cells are loaded, started yielding at a higher displacement and load as the stress in the cells was more uniform. Comparisons similar to the ones conducted in Figure 56b and Figure 57b were performed for each perturbation configuration.

All comparisons concluded that local plastic deformation in cell walls commences slightly after the 0.03 mm mark, except for the cases with three loaded cells. This conclusion indicates that axial loading and stress uniformity drive initial plastic deformation in cell walls. Superposing the perturbations with the highest amplitude and frequency increased the honeycomb core's mass and cross-sectional area by 11.8%. This slight increase did not considerably affect the axial stress arising from the out-of-plane loading. Therefore, initial yielding in cell walls appeared around the same out-of-plane displacement, regardless of the level of applied perturbation. The superposed perturbations improved the peak load by a percentage that exceeded the percentage increase in mass. For instance, the three cell-loaded cases exhibited a ~28.5% improvement in peak load, which is 141% higher than the increase in mass.

The transition from buckling-based to yielding-based deformation, caused by the superposed perturbations, is linked to changes in the deformation and stress fields within cell walls. Figure 58 demonstrates these changes by comparing the deformation and stress fields in the unperturbed case with those of the highest perturbed case (A = 0.3 mm and n = 4) at the cores' peak loads. Figure 58 uses the single-loaded cell as an illustrative case, as all load scenarios exhibited relatively consistent trends.

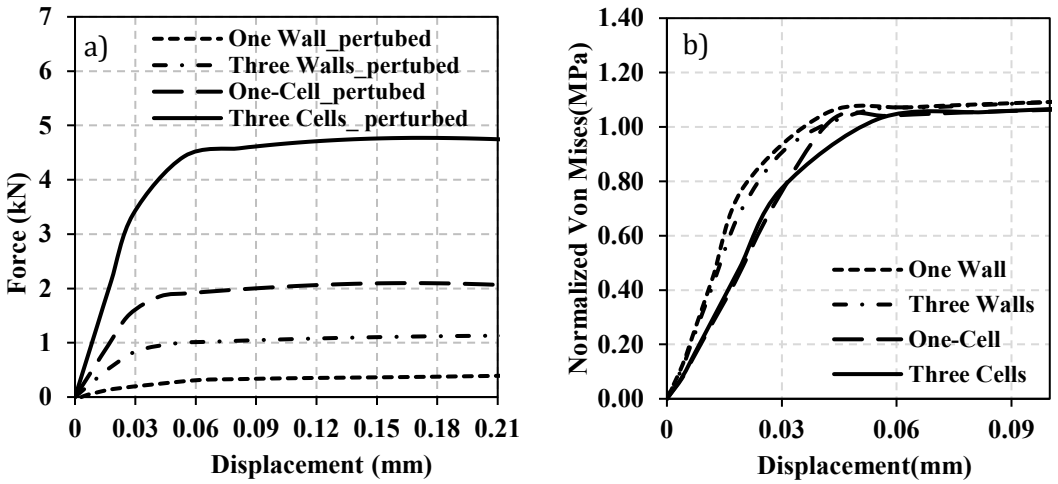

Figure 57: Out-of-plane response of a honeycomb core after superposing a perturbation with an amplitude of 0.3 mm and a frequency of 4, showing a) its out-of-plane force-displacement response and b) the maximum stress observed in its cell walls

According to Figure 58a, deformation at peak load in the unperturbed core has a significant lateral component (i.e., vertical to the walls), indicating buckling-based deformation. Superposing perturbations makes the deformation more uniform and minimizes lateral deformations, see Figure 58b.

Moreover, this figure indicates that deformations are mainly in the form of axial strain along the axis of the cell. Stress in the case of the unperturbed core is heterogeneous, with concentrations near locations of pronounced lateral deformations and near connections with neighboring cells, see Figure 58c. Introducing perturbations, as seen in Figure 58d, transforms the stress distribution to be more uniform along the walls' length direction. After applying the perturbations, the highest stresses became localized near the loaded edges and diminished as one moved farther from the loaded regions. The latter stress distribution underscores a yielding-based deformation, where normal deformations and strains along the axis of the cells dominate the deformation mechanisms.

The discussion above underscored the effect of large perturbation frequencies and amplitudes (i.e., the extreme case). However, to highlight the impact of the perturbation level, the force-deflection response corresponding to every perturbation scenario used is analyzed.

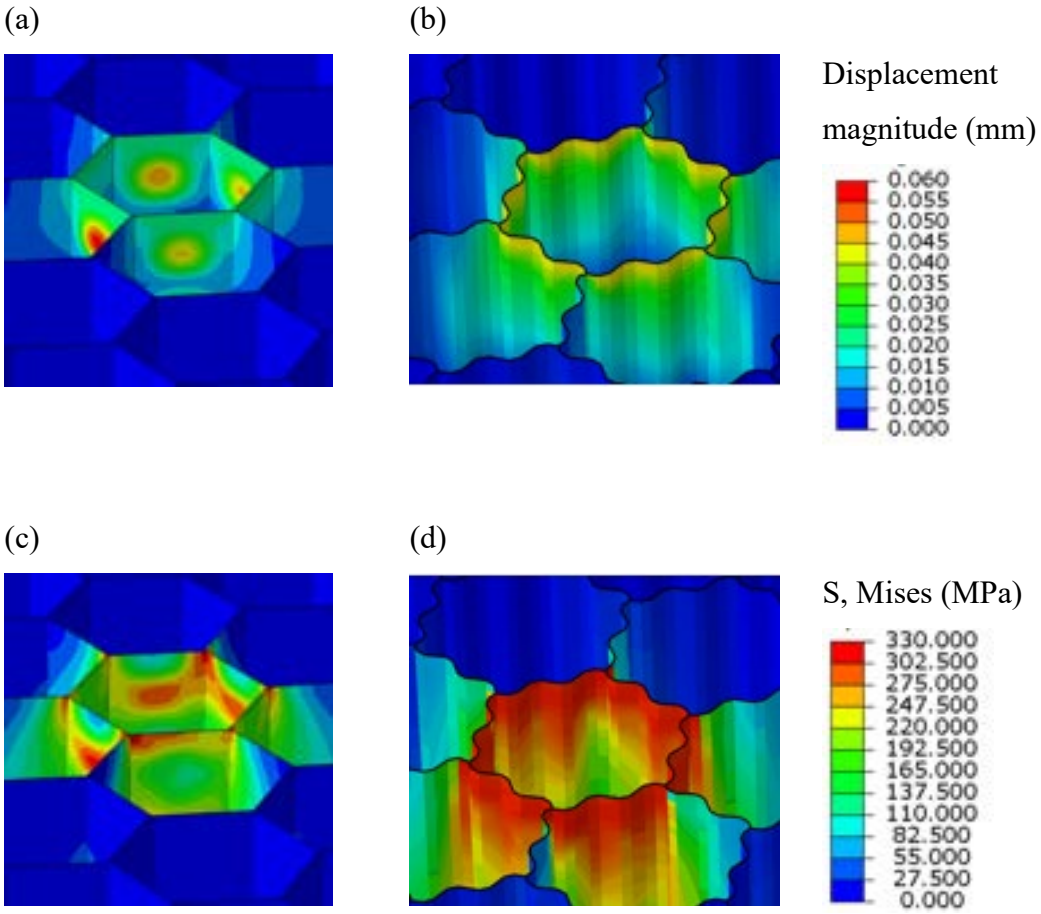

Figure 58: Effect of perturbation on deformation and stress fields in cell walls at peak load, showing a) deformation field in unperturbed, b) deformation field in perturbed, c) stress in unperturbed, and d) stress field in perturbed cores

Figure 59 shows the force-deflection response of the perturbed honeycomb cores due to the most concentrated loading (i.e., load acts on a single cell wall). This figure demonstrates a gradual change in the force-deflection characteristics with increased perturbation frequencies. At the lowest imposed frequency, see Figure 59a, a softening behavior appears after the peak load observed at the end of the linear force-displacement phase. This softening behavior is also observed in the unperturbed case.

The softening behavior gradually disappears with increased perturbation frequency (e.g., Figure 59b) and is replaced by a hardening behavior at high perturbation frequencies (e.g., Figure 59c and Figure 59d). By diminishing the softening phase, increased perturbation frequencies increase the smoothness of the transition between the elastic and plastic deformation phases.

Imposed perturbations also affected the initial failure mode. Loading a single cell in the unperturbed honeycomb core, as seen in Figure 56, led to an initial elastic buckling failure before the 0.03 mm displacement mark.

Imposing perturbation frequencies of 2, 3, and 4 eliminated the elastic buckling failure mode and substituted it with plastic yielding that occurs at higher out-of-plane loads. These loads increased with the increase in perturbation frequency. However, imposing a perturbation frequency of 1, as seen in Figure 59a, shifted the peak load to the 0.03 mm mark, which corresponds to the stage at which cell walls start to yield. Accordingly, plastic buckling rather than elastic buckling controls the initial failure in the case of a perturbation frequency of 1.

Overall, the force-deflection behavior presented in Figure 59 shows that the load-carrying capacity of the perturbed honeycomb gradually increased with each increase in perturbation frequency. Moreover, the force-deflection behavior showed stronger sensitivity to perturbation amplitude at higher perturbation frequency. Figure 59 shows that the force-displacement curves corresponding to different perturbation amplitudes relatively overlap at small perturbation frequencies, while they diverge at higher perturbation frequencies.

The analysis applied above to the case with a single loaded cell wall is applied to the rest of the loading cases. The force-displacement curves of the cases with loading applied on three walls, one cell, and three cells are presented in Figure 60, Figure 61, and Figure 62, respectively. These figures demonstrate that the effect of the perturbation on the load-displacement behavior is generally similar to that observed in the case of loading applied on one cell wall, shown in Figure 59. Increasing the frequency of the superposed perturbations gradually eliminated the post-buckling softening phase, eliminated plastic buckling failure mode, smoothened the transition between the elastic and plastic deformation phases, and increased the load-carrying capacity of the core.

In addition, force-displacement curves in all load cases showed more sensitivity to perturbation amplitude at higher frequencies. Higher sensitivity manifested as increased divergence between the force-displacement curves at higher frequencies. In general, results suggest that a perturbation amplitude of 0.3 mm and perturbation frequency of 4 is sufficient to eliminate the softening behavior after the elastic phase.

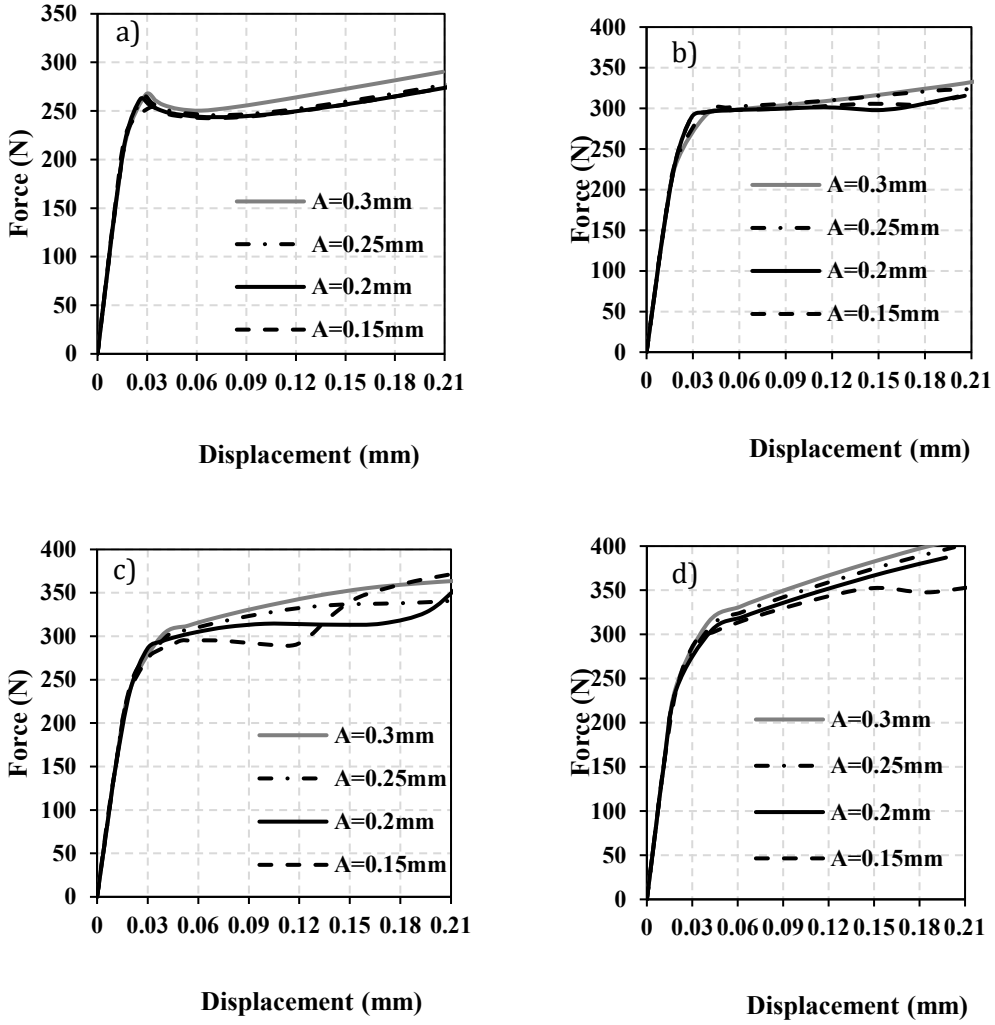

Figure 59: Out-of-plane force-deflection response of perturbed honeycomb core subjected to concentrated loading on one cell wall, showing the response corresponding to the perturbation frequencies (n) of a) 1, b) 2, c) 3 and d) 4

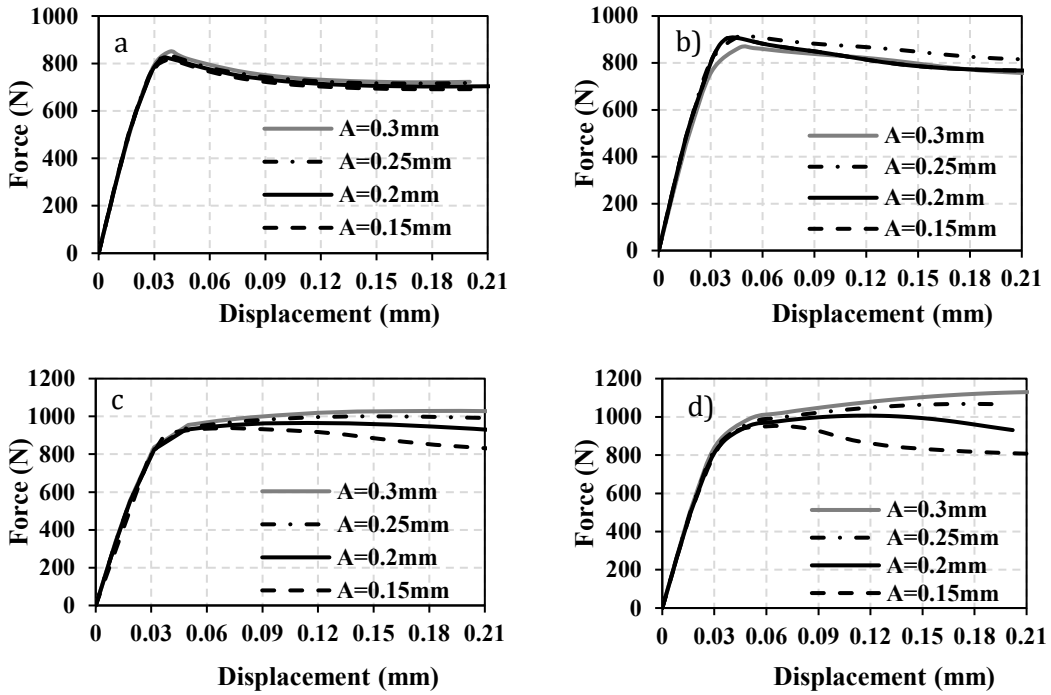

Figure 60: Out-of-plane force-deflection response of perturbed honeycomb core subjected to concentrated loading on three walls, showing the response corresponding to the perturbation frequencies (n) of a) 1, b) 2, c) 3 and d) 4

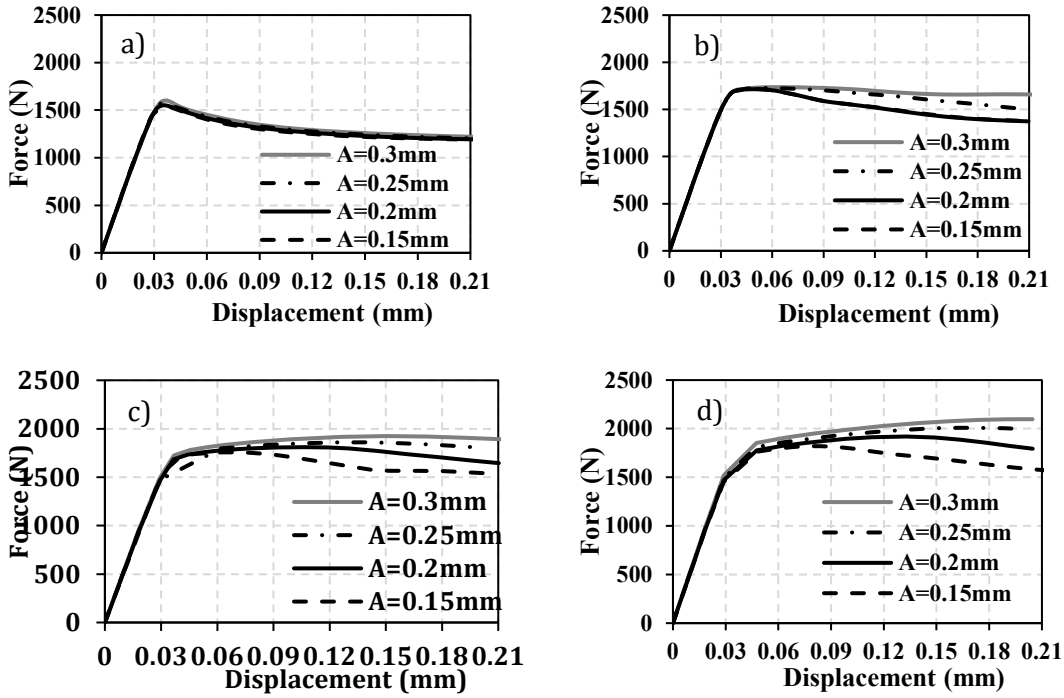

Figure 61:Out-of-plane force-deflection response of perturbed honeycomb core subjected to concentrated loading on one cell, showing the response corresponding to the perturbation frequencies (n) of a) 1, b) 2, c) 3 and d) 4

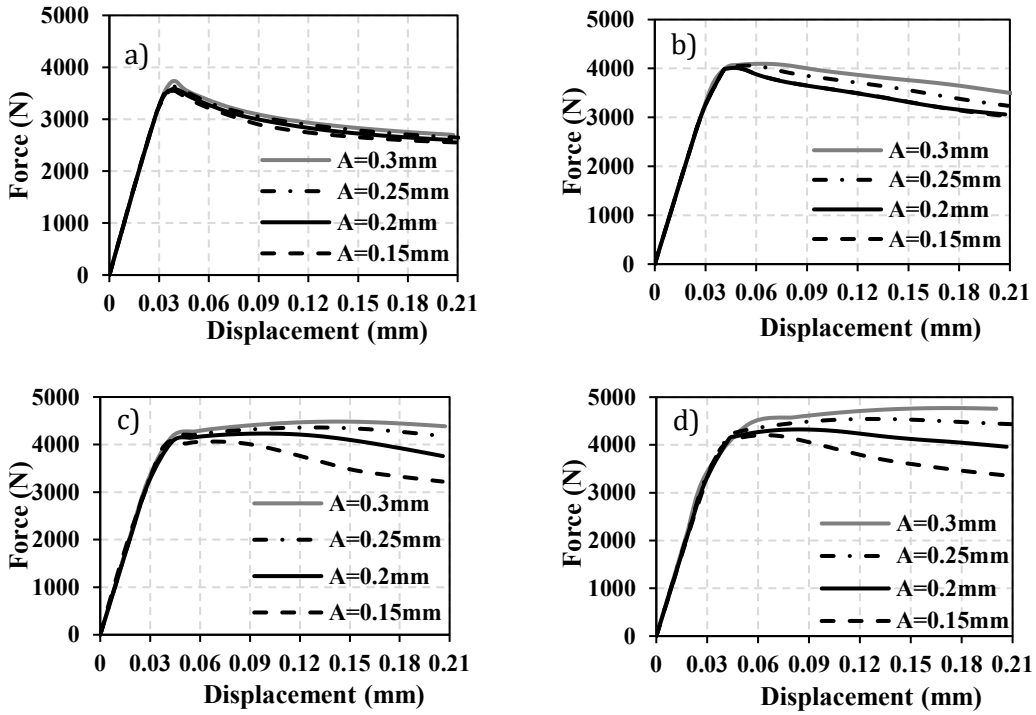

Figure 62: Out-of-plane force-deflection response of perturbed honeycomb core subjected to concentrated loading on three cells, showing the response corresponding to the perturbation frequencies (n) of a) 1, b) 2, c) 3, and d) 4

7.2.2 In-plane response

The effect of the superposed perturbations on the in-plane compressive response of the honeycomb core is demonstrated in Figure 63. In particular, this figure illustrates the perturbation effect on the honeycomb's elastic and plastic properties. Both properties are important as they affect the core's capacity to carry flexural and transverse shear loads. Figure 63 shows that the stress-strain curves of the perturbed cores relatively coincide in the elastic deformation phase, indicating a perturbation-insensitive behavior. However, at the highest perturbation amplitude, perturbations commence to affect the core's elastic behavior by reducing its elastic stiffness, as seen in Figure 63d. Although the latter observed drop in elastic stiffness is negligible, it may grow with a further increase in perturbation amplitude. The peak stress at the end of the elastic phase for all perturbation conditions coincided at ~0.084 MPa, as seen in Figure 63, demonstrating the insensitivity of the initial yielding to perturbation.

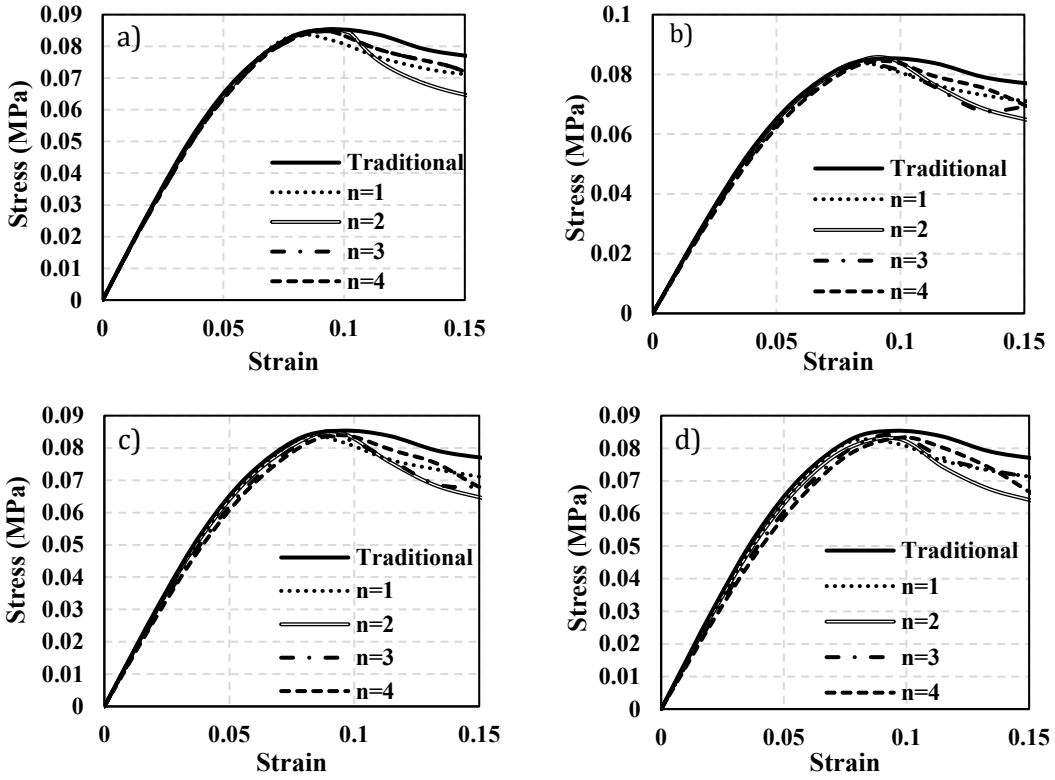

Figure 63: In-plane compressive response of the perturbed honeycomb lattices, showing the insensitivity of the in-plane stiffness and yield of hexagonal double-wall honeycombs to the perturbation amplitudes of a) 0.15, b) 0.2, c) 0.25 and d) 0.3

Unlike the elastic and initial yielding behavior, the post-yielding behavior exhibited sensitivity to perturbation. After the peak stress, the stress-strain curves, as seen in Figure 63, diverge and scatter, indicating a perturbation-sensitive plastic behavior. Diverging stress-strain curves showed more sensitivity to frequency rather than amplitude. The effect of amplitude is almost negligible. Perturbed cores generally exhibited more significant post-yield softening and lower post-yield load-carrying capacity than the unperturbed core. At the maximum strain shown in the figures (i.e., 15%), the maximum drop in the post-yield load-carrying capacity is ~16%. The latter occurred at a perturbation frequency of 2. Results indicate that the relation between the decrease in the post-yield strength and perturbation frequency is nonmonotonic.

Superposing the sinusoidal perturbations should increase the second moment of inertia of the modified cell walls, which, in turn, should theoretically increase their resistance to out-of-plane buckling instabilities and bending [125], [134]. The out-of-plane second moment of inertia of the perturbed cell wall shown in previous figures can be computed as:

$$I = \int_0^L u(x)^2 dA = t \int_0^L u(x)^2 \sqrt{\left(\frac{du}{dx}\right)^2 + 1}\, dx \quad (63)$$

such that L and t are the length and thickness of the cell wall, respectively, and $u(x)$ is the perturbation function. Numerically evaluating this equation shows that the second moment of inertia of the perturbed wall is 13 times (lowest perturbation frequency and magnitude) to 57 times (highest perturbation frequency and magnitude) higher than that of the unperturbed cell wall. Moreover, the results of Equation (63) showed that the second moment of inertia is sensitive to the perturbation magnitude and insensitive to frequency. Changing the frequency from 1 to 4 does not change the out-of-plane second moment of inertia by more than 6%.

The significant increase in the second moment of inertia drove but did not directly correlate with the improvement in the resistance of the perturbed cores to failure under out-of-plane loads. To illustrate this point, the peak loads observed at the end of the linear phase are extracted from Figure 59, Figure 60, Figure 61, and Figure 62 and plotted in Figure 64. The offset method commonly used to define yield strength was used for cases that do not show a clear peak load, mainly at high perturbations. However, a 0.13% strain offset was used instead of the widely used 0.2%. The latter overestimated the peak load in cases with a clear peak load. To determine the strain offset, the strain was computed by dividing the displacement by the height of the honeycomb core. It is worth reminding that the 0.2% offset is not a standard and was proposed for metals, so using a different value is not uncommon. The peak load in this work represents the strength of the honeycomb core at the early stages of deformation before progressive collapse and densification.

Figure 64 shows that a frequency of 1 results in a negative effect, where the peak load of the perturbed cores is lower than that of the unperturbed core. At frequencies higher than 2, perturbations induced a strengthening effect. The increase in the peak load at the highest perturbation frequency and magnitude, compared to the unperturbed case, is in the range of 14% to ~28.5%, depending on the loading scenario size. These values are moderate compared to the calculated increase in the second moment of inertia. The lack of direct correlation can be attributed to the existence of multiple deformation modes, load sharing and support at the vertices, and the warping of cell walls at large loads.

Accordingly, cell walls carry complex loads at the peak load, not simple axial and bending loads as theoretical models assume. Interestingly, Figure 64 shows that peak

load increases with frequency more than it increases with perturbation magnitude. This behavior contrasts with that of the second moment of inertia, indicating the existence of nonuniform deformations. Higher perturbation frequencies introduce increased resistance to multiaxial nonuniform bending deformations. To establish a comparative viewpoint, one can liken the high-frequency perturbations to the bends and contours imprinted onto sheet metal, aiming to enhance its resistance to bending, as commonly seen in the automotive industry. The methodology section mentioned that four loading scenarios are used to overcome the uncertainty regarding the size and location of the localized impact area. Impacting objects during low-velocity impact engage different numbers of cell walls; therefore, the resistance experienced by each impacting object could be different. Accordingly, using a single loading scenario to investigate the response of a structure or study the effect of a geometric parameter can be misleading. This concept is demonstrated in Figure 64. The effect of imposing perturbations on the peak load depends on the loading scenario. For instance, the highest enhancement in the peak load of the perturbed cores was ~14%, ~19.8%, 16.6%, and ~28.5% for the loading cases of one wall, three walls, one cell, and three cells, respectively. Accordingly, the same perturbation settings resulted in different improvements, demonstrating the need to utilize multiple loading scenarios to better understand the effect of special geometric features. Collectively, the four scenarios underscore the positive effect of the introduced perturbations on the peak load of the perturbed cores.

The added perturbations eliminated the post-peak softening and introduced a mild hardening response in some cases. To evaluate their effect on the post-peak response, the areas under the force-displacement curves, representing toughness, were computed and are presented in Figure 65. Figure 65 demonstrates a positive correlation between toughness and increased perturbation frequency or amplitude. Like peak load, the area under the force-displacement curves is sensitive to frequency more than amplitude. The highest areas are observed at the highest perturbation frequency and amplitude. At the highest perturbation settings, the area under the force-displacement curves increased, compared to the unperturbed honeycomb, between 34.8% and 56.7%, depending on the loading scenario. Thus, the four loading scenarios underscore the effectiveness of the superposed perturbations in enhancing the post-peak behavior. Accordingly, results confirm that the superposed perturbations can improve the load-carrying capacity of honeycomb cores under out-of-plane loads.

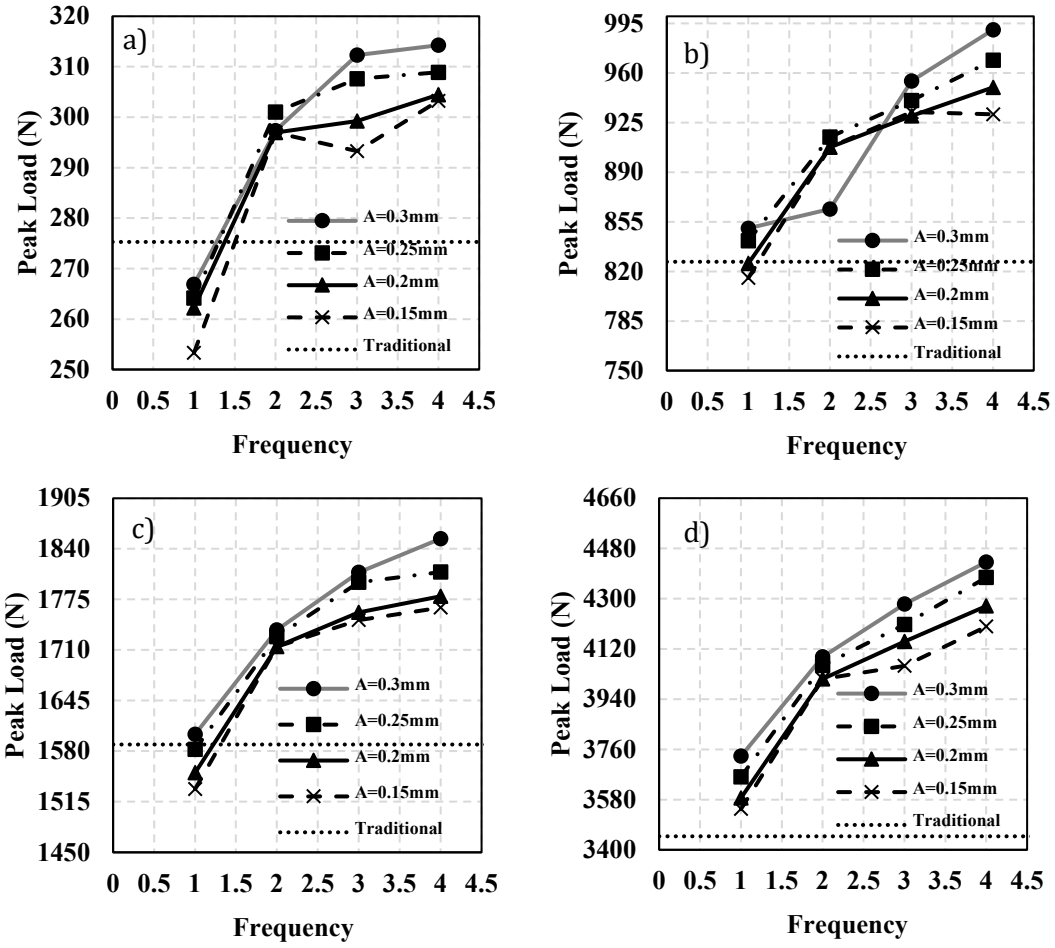

Figure 64: Effect of perturbations' amplitude and frequency on the peak out-of-plane load for a) one cell wall, b) three cell walls, c) one cell, and d) three cells

The effect of the superposed perturbations on the in-plane response was illustrated in Figure 63 as negligible. Such behavior is consistent with the analytical models developed to describe the stiffness and yielding of regular honeycombs [110], [135]. These models assume cell wall bending is the dominant deformation mode in regular honeycombs subjected to uniaxial compressive loads. The bending moment driving cell wall bending in regular honeycombs depends on their cell wall length. As the superposed perturbations do not relocate the parent cores' vertices, the effective cell wall length, i.e., the distance between vertices, remains similar to that of the parent regular honeycomb. Therefore, the underlying deformation mechanism under uniaxial compressive loading in the perturbed and unperturbed parent honeycomb are identical, resulting in the insensitivity of the in-plane compressive stiffness and yield response to perturbations.

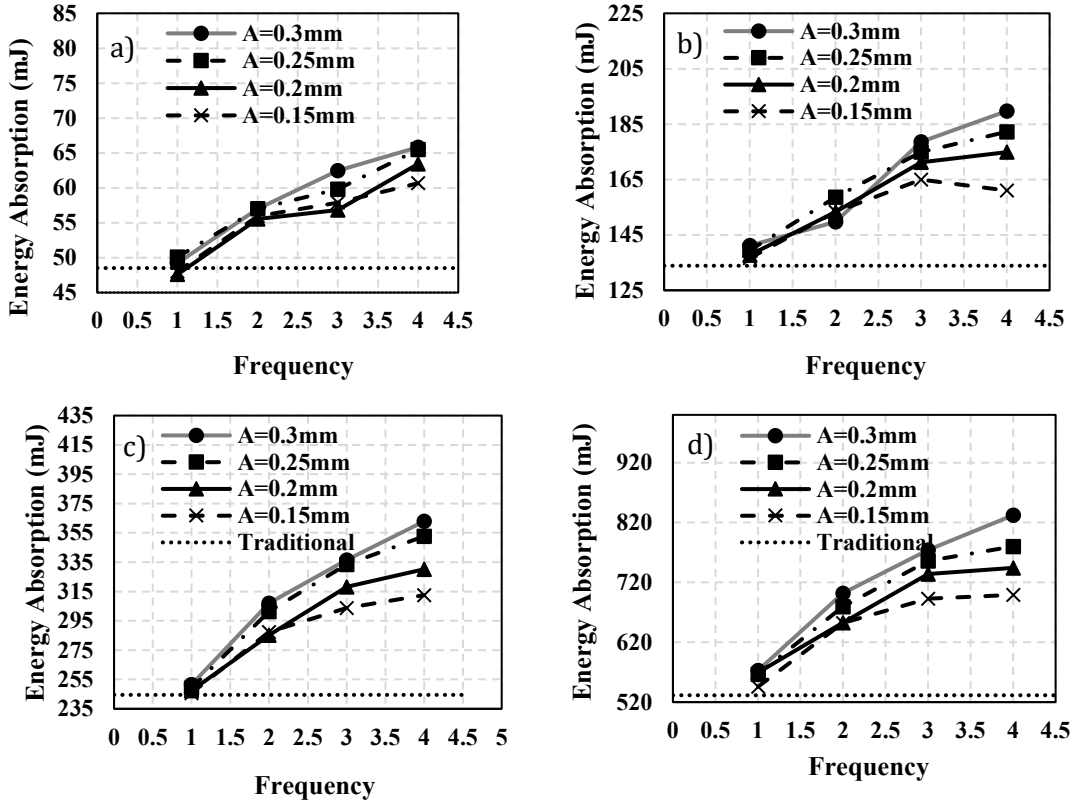

Figure 65: Effect of perturbations' amplitude and frequency on the area under the force-displacement curve during localized out-of-plane loading on a) one cell wall, b) three cell walls, c) one cell, and d) three cells. The dashed line represents the response of the response of the unperturbed parent honeycomb core.

7.2.3 Low-velocity impact

To assist in generalizing the results of this work, it is essential to discuss the dependence of the results on boundary conditions and cell walls' constituent material. The objective here is to shed light on whether the effectiveness of the introduced perturbations is limited to the employed boundary conditions and constituent material. The boundary conditions used to model the out-of-plane behavior of the cores align with those associated with cores serving in sandwich structures. The boundary conditions used are referred to as fixed-fixed conditions in the context of buckling. The epoxy at the core-composite sheet interface constrains cell walls' lateral and rotational motion.

Without the presence of the composite sheets, the core's out-of-plane loading would be accompanied by translational and rotational deformations at the edges of the loaded cell walls. In such loading conditions, the perturbations investigated in this work are expected to enhance the out-of-plane structural performance but to a different extent than observed in the investigated fixed-fixed loading case. To shed light on the

effectiveness of the introduced perturbations in out-of-plane loading scenarios beyond those covered in the methodology, indentation simulations are performed on 8×8 honeycomb core models whose top edges are allowed to rotate and move laterally (i.e., the core is not in a sandwich structure configuration).

Two models are considered: one represents the unperturbed parent core, while the other represents the perturbed core with a frequency of 4 and a magnitude of 0.3 mm. The cores' bottom edges were fixed. A 9.5 mm diameter cylindrical rigid indenter, i.e., the same size as the core's cell, was used to generate the out-of-plane loading. Contact interaction was defined at the indenter-core interface and assigned a friction coefficient of 0.2. Abaqus explicit was used to simplify the simulation process because it involves contact interactions. The indenter was displaced at a rate of 0.2 mm/s (0.72 km/h). Accordingly, the models represent a localized low-velocity impact (i.e., indentation) scenario. Figure 66 shows the schematics of the low-velocity out-of-plane loading scenario.

The finite element software calculated the force applied to the impactor to generate the prescribed displacement. The load-displacement curves corresponding to the perturbed and unperturbed cores are shown in Figure 67. The results of the indentation simulations confirm the superiority of the perturbed core. Moreover, the results follow the trends observed in the fixed-fixed loading conditions. Nevertheless, under impact conditions without lateral and rotational constraints at the top edges, the perturbed and unperturbed cores exhibit peak loads that are 20% and 34% lower, respectively, compared to the fixed-fixed loading condition. The lower peak load is expected due to the lack of translational and rotational restrictions.

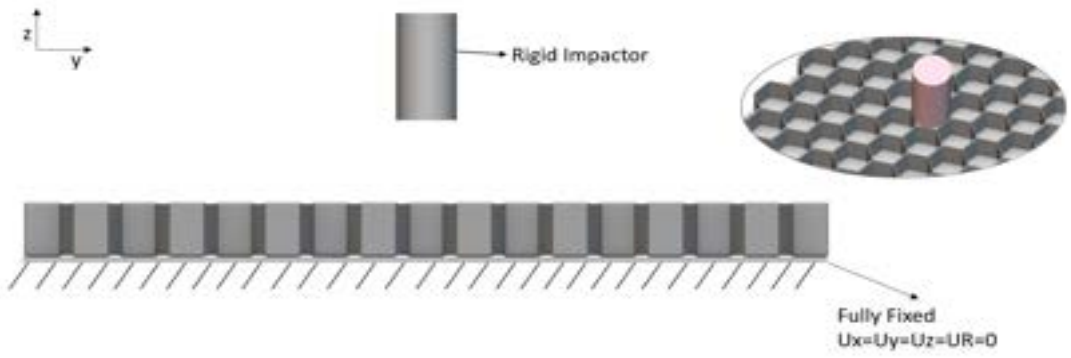

Figure 66: Schematics of low-velocity localized impact loading

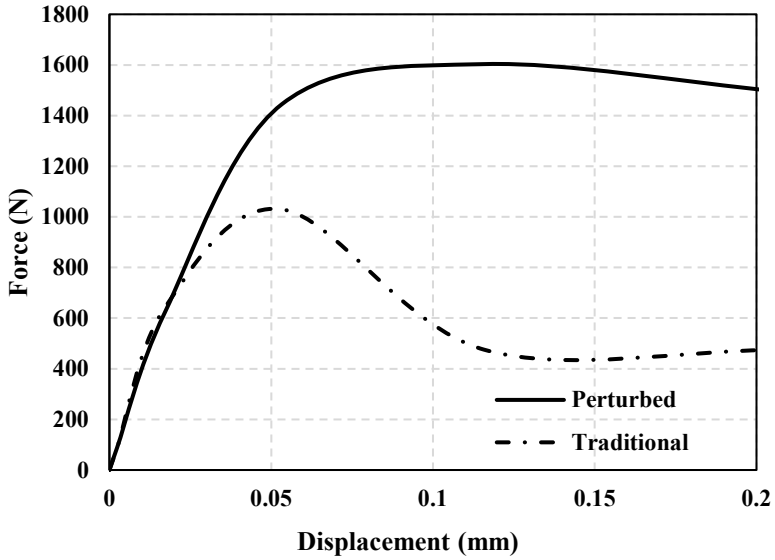

Figure 67: Force-displacement response under out-of-plane low-velocity impact, showing the response of the unperturbed and the highly perturbed core (n=4, A=0.3)

Based on the impact simulation results, which can be considered a case study, it can be argued that the superposed perturbations enhance honeycomb cores' strength and load-carrying capacity under out-of-plane loads in general. However, the magnitude of enhancement depends on the boundary conditions associated with the out-of-plane loading. Similarly, using a different cell wall constituent material is anticipated to affect but not diminish the effectiveness of the introduced perturbations. In particular, constituent materials with lower yield strengths are expected to be less enhanced by the perturbations as they are more prone to plastic buckling. In such cases, higher perturbations would be needed to transform the underlying deformation mechanism from buckling to yielding.

7.2.4 Flexural response

The flexural response of the perturbed cores is illustrated in Figure 68 through their moment-rotation response. Imposing sinusoidal perturbations reduced the flexural stiffness of the core. The unperturbed core delivered the highest flexural stiffness and peak bending moment (507 N.mm). The peak bending moment is the largest moment realized by a moment-rotation curve, followed by a plateau at the peak moment and then a gradual decrease in the moment as the rotation increases. The slope of the moment-rotation curve during its initial linear phase represents the flexural stiffness. The lowest flexural stiffness and peak moment corresponded to a perturbation

frequency and amplitude of 4 and 0.3, respectively. The peak moment of the largest perturbed case is ~45% lower than that of the unperturbed case. The reducing effect of perturbations on the flexural response appears to be approximately monotonic.

The flexural stiffness and peak moment decreased with increasing perturbation frequencies or amplitudes except in a few cases. For instance, at a perturbation frequency of 2, increasing the perturbation amplitude from 0.15 mm to 0.2 mm increased the peak load from 348.9 N.mm to 368.5 N.mm. Overall, the results demonstrate a softening effect of perturbations on the flexural response. The flexural response appears to follow a linear behavior at the highest perturbation frequencies. This behavior is indicative of increased compliance by the structure and is supportive of a gradual and controlled loading pattern.

There are no sudden spikes in the moment in all cases. Such behavior is sought after, for instance, in impact energy mitigation applications. The change in slope in the traditional cases during the linear phase can be indicative of a higher flexural stiffness within the traditional core. In perturbed cases, this flexural stiffness is reduced due to the alteration of the second moment of inertia induced by sinusoidal perturbations.

The cellular core degree of softening is altered as the sinusoidal perturbations are introduced as a result of changing the load-bearing characteristics of the unit cell, and any nonlinearity introduced by the material properties or geometry is diminished by the effects of the perturbations.

7.2.5 Transverse shear loading

The effect of the superposed perturbations on the transverse shear response of the honeycomb core is presented in Figure 69. The figure shows the average transverse shear force-displacement curves resulting from loading a sheet comprised of 8×1 cells by a transverse load, as discussed in the methodology section. Figure 69 illustrates a softening effect of the superposed perturbations on the transverse shear response. The slope of the shear force-displacement curves in the linear range is representative of the transverse shear stiff of the perturbed core, and a reduced slope indicates reduced stiffness.

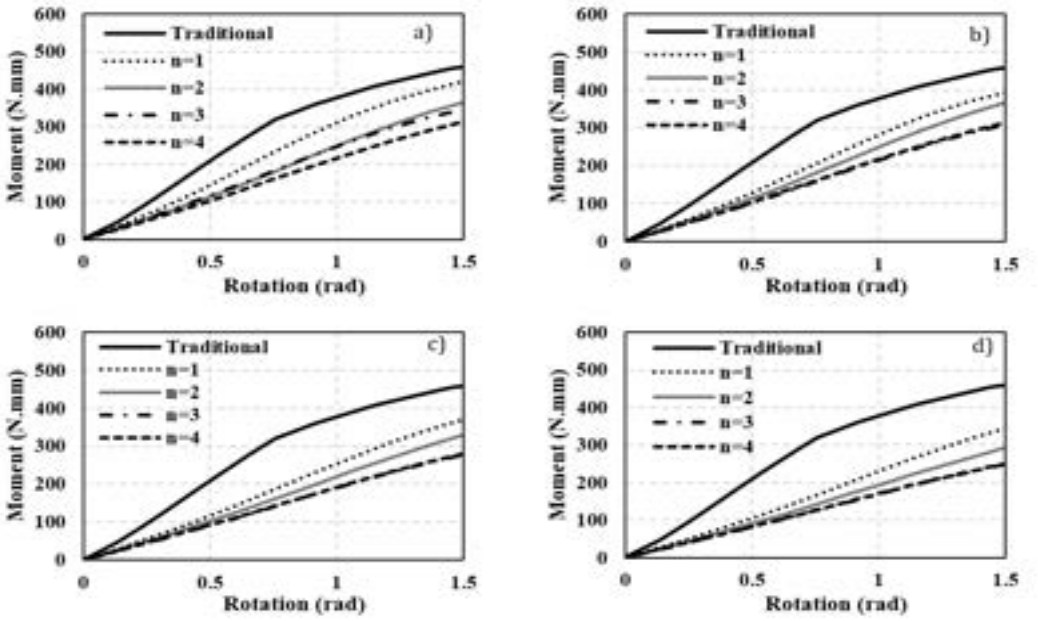

Figure 68: Flexural response of the perturbed honeycomb lattices, showing the sensitivity of the moment-rotation curves to perturbation at the perturbation amplitudes of a) 0.15, b) 0.2, c) 0.25, and d) 0.3

Generally, increasing the perturbation frequency or amplitude decreased the transverse shear stiffness of the perturbed cores. The only exception to this trend appeared at the perturbation amplitude of 0.15 mm, where the shear stiffness at the frequencies of 3 and 4 was slightly higher than at a frequency of 1. The incremental reduction in stiffness, defined as the decrease in stiffness between two consecutive frequencies, decreased with increasing frequency. Thus, the frequencies of 3 and 4 resulted in overlapping transverse shear force-displacement responses.

Moreover, Figure 69 shows that the effect of perturbation frequencies is amplified at higher perturbation amplitudes. For instance, the incremental decrease in stiffness between the cases with perturbation frequencies of 3 and 4 is higher at a perturbation of 0.3 than at the perpetuation of 0.25. The reduction in stiffness caused by superposing the sinusoidal perturbations is accompanied by a decrease in the core's ability to resist permanent deformation and yielding. The onset of yielding at the cores' structural level can be defined as the stress level at which the transverse shear force-displacement curve transitions from the linear phase to the nonlinear phase. Similar to the flexural loading case, increasing the perturbation level increased the structure's compliance, and an approximately linear shear force-displacement response was observed at the highest perturbation levels. Such behavior supports smoother loading profiles, which is favored in impact load mitigation applications. Imposing the sinusoidal perturbations on the

honeycomb lattice significantly influences its flexural and transverse shear properties. The sinusoidal perturbations introduced geometric imperfections in the cores' structure, prompting the development of nonuniform and localized stresses, as shown in Figure 70 (units in MPa).

The straight cell walls in the unperturbed honeycombs serve as the force transmission paths for the in-plane forces induced by flexural and transverse loads. The unperturbed cell walls have the best load-bearing ability as straight lines. In the perturbed cores, the force transmission paths for the in-plane forces pass through curved cell walls, which offer lower load-bearing ability than their straight counterparts. Accordingly, the curved cell walls are more prone to developing nonuniform and localized stresses.

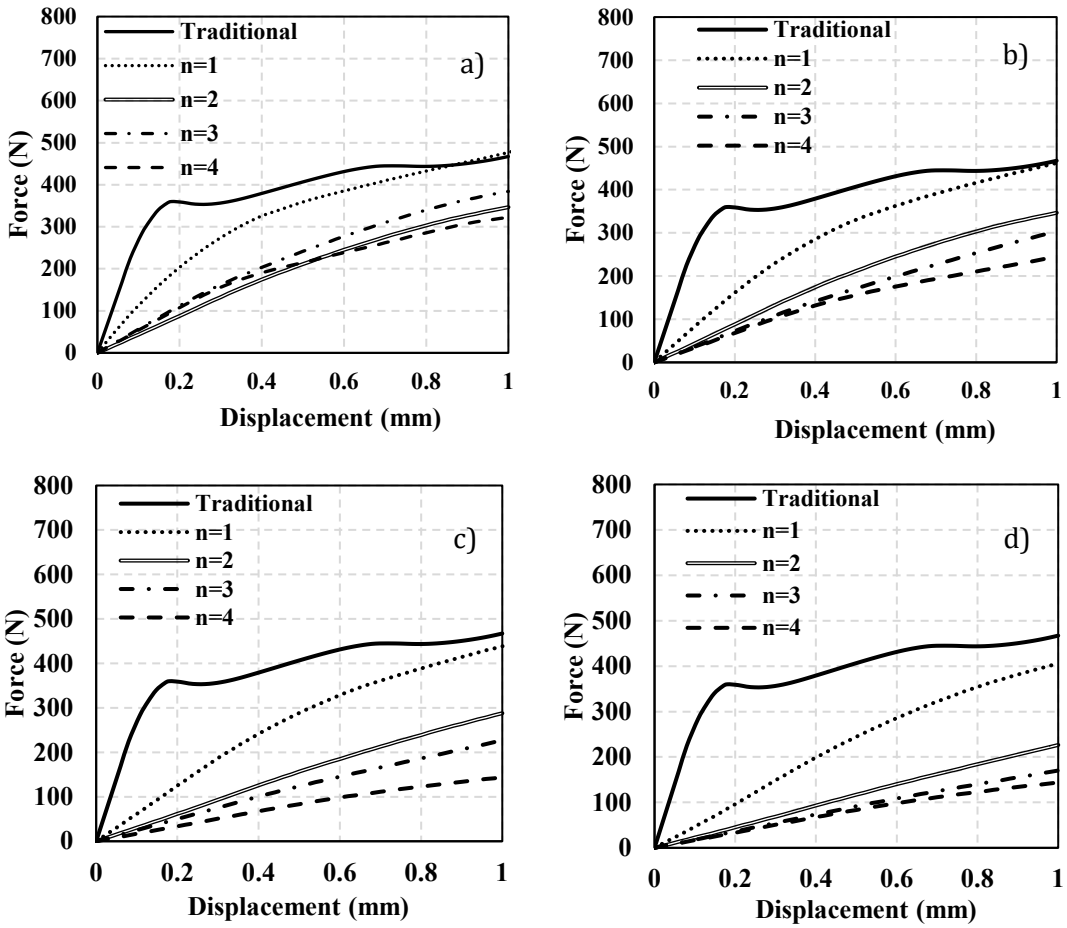

Figure 69: Response of the perturbed honeycomb lattices to transverse shear force, showing the sensitivity of the transverse force-displacement curves to perturbation at the perturbation amplitudes of a) 0.15, b) 0.2, c) 0.25, and d) 0.3

The softening behavior driven by the development of localized stresses provides a smoother loading response that gives rise to a slowly rising resistance to deformation. From a structural integrity perspective, such behavior can be concerning. However, from the standpoint of mitigating impact energy, such behavior is appealing, as it would allow for the gradual dissipation of impact energy, thereby avoiding sudden shocks or overloading of a protected person, structure, or device.

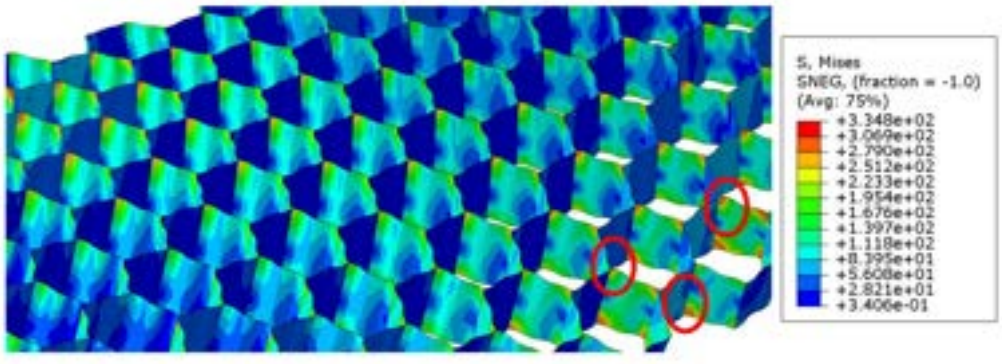

Figure 70: Stress contour plot of perturbed honeycomb panel under pure bending

7.2.6 Three-point bending

The deformation modes, peak loads, and specific energy absorption are reported for the sandwich structures corresponding to the 5 different cores considered, i.e., 4 perturbed and 1 traditional. The average macroscopic deformation of the 5 sandwich structures is similar. Figure 71 represents the typical observed deformed shape of the modeled sandwich structures. As the load is applied at the middle of the panel, a narrow indentation forms under the indenting roller. The figure also shows the local deformations at the point of contact. The face sheet thickness plays a crucial role in distributing the local forces and deformations.

The load-displacement curves of the 5 sandwich structures considered are shown in Figure 72. To validate the finite element model's accuracy, the force-displacement result corresponding to the sandwich structure with the traditional honeycomb core is compared to that of a similar panel that was experimentally tested [116]. The result of this work agrees well with the experimental results; a maximum difference of 3% is observed.

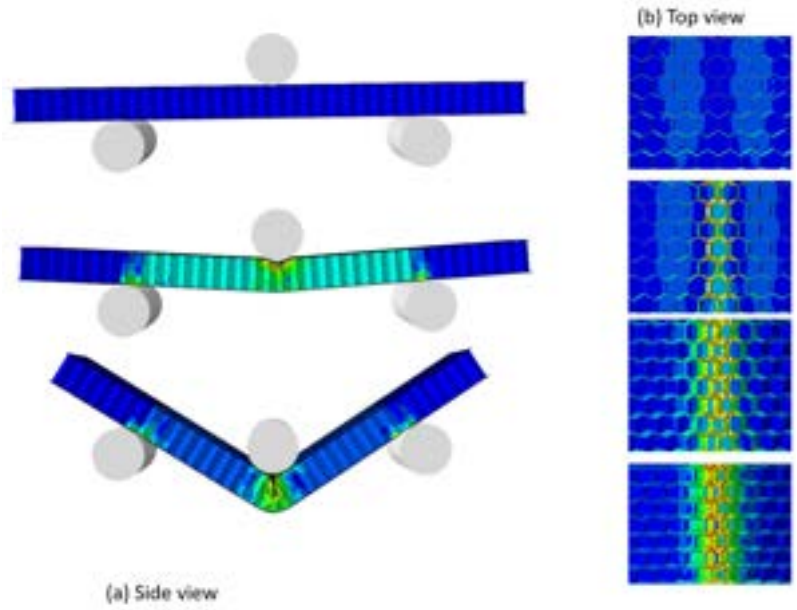

Figure 71: Deformation of a sandwich structure under 3-poing bend loading, showing localized

According to Figure 72, the peak load realized by the sandwich structure comprising a traditional honeycomb core is 2.17 kN. However, replacing the conventional honeycomb core with a perturbed one can increase the peak load to 2.95 kN. This increase is related to the increased second moment of inertia and improved stiffness. The perturbed cores are 0.3% higher in weight than their traditional counterparts, and this increase in weight is negligible compared to the increase in peak load which reached 36%.

Figure 72 shows that the perturbation effect is more relevant in the loading phase. Once the peak load is reached, the force-displacement curves of all sandwich structures showed an exponential decay, and they relatively overlapped once the load decreased below the 1 kN mark. This behavior suggests that once the honeycomb cores start to crumble, the introduced perturbations no longer contribute to the overall flexural strength of the sandwich structure. After the applied force crushes the cells, the perturbed and unperturbed honeycomb cells behave similarly; thus, the final load for all panels is identical.

To further understand the effect of modifying hexagonal honeycombs using sinusoidal perturbations, the flexural stiffness and specific energy absorption are calculated for the sandwich structures comprising perturbed cores.

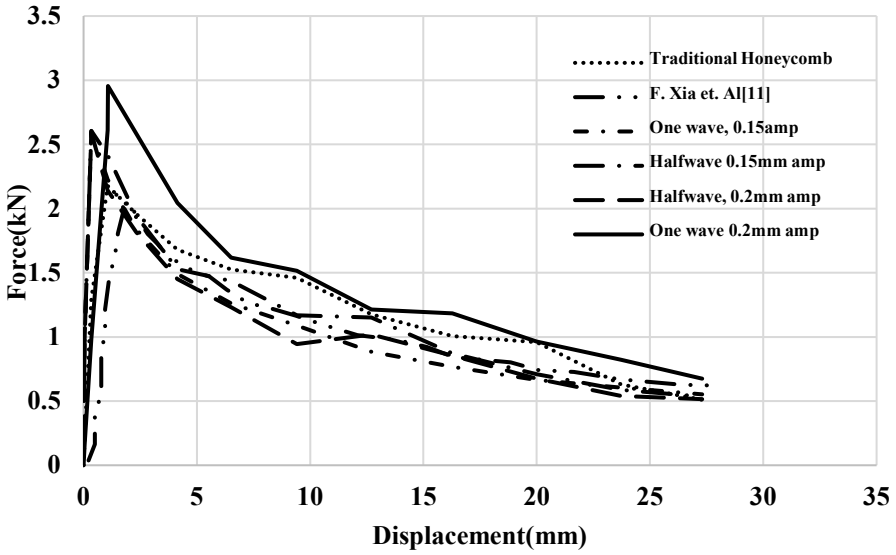

Figure 72: Deformation of a sandwich structure under 3-point bend loading, showing localized

Figure 73 shows the flexural stiffness of the sandwich structures. This figure also compares the results from the sandwich structures with perturbed honeycomb to those of sandwich structures with traditional honeycomb. Figure 73 shows that, in general, an increase in amplitude or frequency increases flexural stiffness. The sandwich structure with the highest frequency and amplitude, namely one wave and an amplitude of 0.2 mm, showed a 35.7% higher flexural stiffness than that of the sandwich structure with the traditional honeycomb. A lower perturbation frequency, namely 0.5 waves per cell wall, did not result in similar substantial improvements. Results suggest that the relationship between frequency, amplitude, and flexural stiffness is non-linear.

Figure 74 shows the specific energy absorbed by the sandwich structures comprising perturbed and unperturbed honeycomb cores. Specific energy absorption is calculated by integrating the area under the force-displacement curve and normalizing the outcome by the mass of the sandwich structure. Figure 74 shows a general trend; the specific energy absorption increases as the perturbation amplitude and frequency used are increased. However, since the imposed sinusoidal perturbations do not contribute to the structural stiffness after the honeycomb starts to collapse, i.e., after peak load, they have a lower enhancing effect on the specific energy absorption as compared to their effect on peak load.

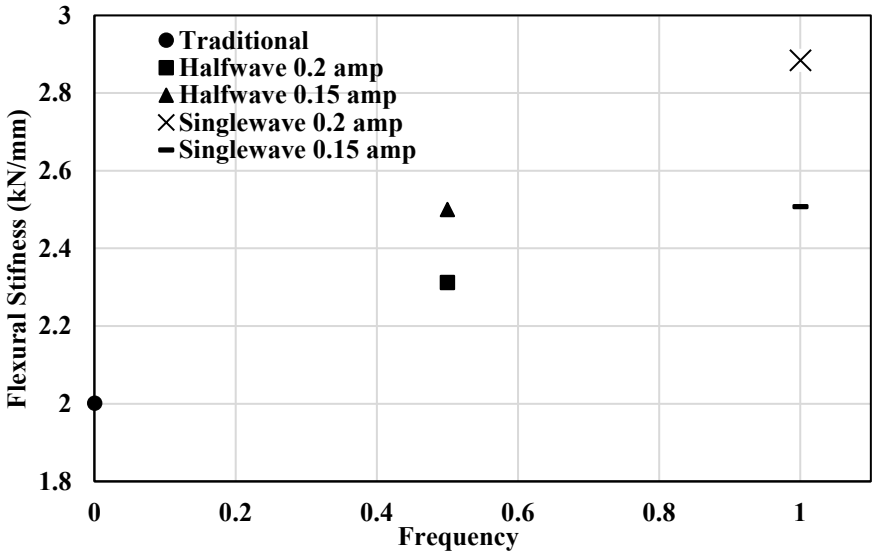

Figure 73: Flexural stiffness of sandwich structures comprising perturbed honeycomb cores

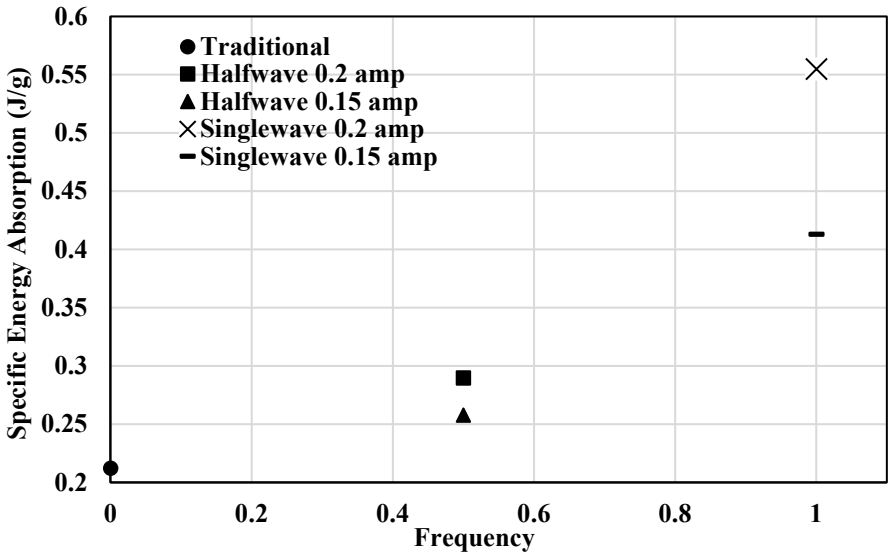

Figure 74: Specific energy absorption of sandwich structures comprising perturbed and unperturbed honeycomb cores

For instance, the specific energy absorption of the sample with the highest perturbation frequency and amplitude is 26% higher than that of the sample with a traditional honeycomb. This increase, though substantial, is less than that exhibited by peak load. Accordingly, unlike the flexural stiffness and peak load, the specific energy absorption considers the phase where the perturbated and traditional honeycomb cores behave similarly.

Chapter 8: Conclusion and Future Recommendations

This dissertation aims to comprehensively explore the different mechanisms that can be utilized to enhance the mechanical and thermal features of cellular solids. The study investigated the effects of copper coating aluminum foam on their mechanical performance. Numerical and experimental techniques were utilized to achieve this goal. FEA was used to perform numerical analysis, while electrodeposition, SEM, EDS, and uni-axial compression tests were used to assess the effect of coatings experimentally. Analytical models were developed to predict the behavior of the coated foams. The models help in tailoring the required coating thickness to achieve the required mechanical properties. The simulations revealed that the stiffness of uniformly copper-coated aluminum foam significantly enhances the stiffness. For instance, the stiffness of foams with 100µm thick coating can be 138% higher than uncoated foams at 4% relative density. As for the yield strength, an enhancement of 30% was recorded at 4% relative density compared to uncoated foams. The thermal conductivity was also significantly enhanced, where the most pronounced effect was recorded at lower relative densities, with up to 196% increase at 4% relative density for 100µm copper coating. Despite the mechanical and thermal benefits, the addition of copper coating significantly increases the overall weight and relative density of the foams. For instance, 100µm coating increases the weight by 221% at 4% relative density. To further assess the effect of added weight, mechanical and thermal properties were normalized by the weight to find the optimum coating thickness.

A unique solution was proposed to efficiently tackle the issue of increased weight in uniformly coated aluminum samples, which introduced functionally graded coating. Functionally graded copper coatings were developed with the aid of an electrodeposition process. Samples were subjected to various characterization techniques to assess the coating quality. This includes the use of SEM and EDS, which show the variation in the coating thickness across the depth of the specimen. The results show close agreement with the numerical simulations where the energy absorption was enhanced up to ~30% with the addition of functionally graded coatings. However, there was a notable difference between the functionally graded coatings and the uniform coatings, which is the elastic modulus. The uniform coatings in the numerical simulations showed significant improvement in the stiffness, whereas the functionally graded coatings resulted in decreasing stiffness.

Finally, this dissertation aimed to enhance the mechanical properties of cellular solids, particularly honeycombs, by introducing sinusoidal perturbations to the honeycomb walls. Numerical simulations were used throughout this research goal to analyze the effect of perturbations on the mechanical properties, specifically the use of FEA. The mechanical features that were investigated include out-of-plane and in-plane compressive responses, as well as their behavior under low-velocity impact, flexural, and transverse shear loading. The introduction of sinusoidal perturbations significantly enhanced the out-of-plane compressive response. The primary result includes a shift in the failure criteria, where the introduction of sinusoidal perturbations resulted in yielding rather than buckling. The perturbations increased the peak load out of plane compression capacity by up to 28.5%, particularly under highly concentrated loads. It was concluded that by increasing the frequency and amplitude of the sinusoidal perturbations, higher enhancement can be achieved. As for the in-plane response, the effect of sinusoidal perturbations was negligible. The flexural response and transverse shear response showed a decrease in the pure bending stiffness and shear stiffness with increased frequency and amplitude.

Overall, various techniques can be utilized to enhance the mechanical and thermal properties of cellular solids. Through altering the topological features or the introduction of metallic coatings, researchers aim to tailor the mechanical and thermal properties to achieve the required properties.

Future research should focus on the recently developed lattice structures (e.g., TPMS) and aim to enhance their mechanical and thermal properties by introducing sinusoidal perturbations in three dimensions with the aid of FEA and CAD. Adding on, limited research has been done on copper-coated aluminum honeycombs, which have been widely used in the industry. The electrodeposition process has been proven to be cost-effective in terms of mechanical and thermal properties. Future research should also aim to investigate the effects of copper-coated aluminum honeycomb on static and dynamic mechanical properties for energy absorption applications.

References

[1] L. Gibson J. and M. Ashby F., *Cellular Solids: Structure and Properties*. 1997.

[2] L. J. Gibson, "Cellular solids," *MRS Bull*, vol. 28, no. 4, pp. 270–274, 2003.

[3] L. Jing, K. Liu, X. Su, and X. Guo, "Experimental and numerical study of square sandwich panels with layered-gradient foam cores to air-blast loading," *Thin-Walled Structures*, vol. 161, p. 107445, 2021.

[4] M.-Y. Yang and J.-S. Huang, "Numerical analysis of the stiffness and strength of regular hexagonal honeycombs with plateau borders," *Compos Struct*, vol. 64, no. 1, pp. 107–114, 2004.

[5] N. B. Dahiwale, S. K. Panigrahi, and K. Akella, "Numerical analyses of sandwich panels with triangular core subjected to impact loading," *Journal of Sandwich Structures & Materials*, vol. 17, no. 3, pp. 238–257, 2015.

[6] F. Usta, H. S. Türkmen, and F. Scarpa, "High-velocity impact resistance of doubly curved sandwich panels with re-entrant honeycomb and foam core," *Int J Impact Eng*, vol. 165, p. 104230, 2022.

[7] D. J. Sypeck, "Cellular truss core sandwich structures," *Applied Composite Materials*, vol. 12, pp. 229–246, 2005.

[8] W. H. Meeks III, "The theory of triply periodic minimal surfaces," *Indiana University Mathematics Journal*, pp. 877–936, 1990.

[9] A. P. G. Castro, R. B. Ruben, S. B. Gonçalves, J. Pinheiro, J. M. Guedes, and P. R. Fernandes, "Numerical and experimental evaluation of TPMS Gyroid scaffolds for bone tissue engineering," *Comput Methods Biomech Biomed Engin*, vol. 22, no. 6, pp. 567–573, 2019.

[10] N. Novak *et al.*, "Development of novel hybrid TPMS cellular lattices and their mechanical characterisation," *journal of materials research and technology*, vol. 15, pp. 1318–1329, 2021.

[11] I. Kaur and P. Singh, "Flow and thermal transport characteristics of Triply-Periodic Minimal Surface (TPMS)-based gyroid and Schwarz-P cellular materials," *Numeri Heat Transf A Appl*, vol. 79, no. 8, pp. 553–569, 2021.

[12] A. Okabe, B. Boots, K. Sugihara, and S. N. Chiu, *Spatial tessellations: concepts and applications of Voronoi diagrams*, vol. 501. John Wiley & Sons, 2009.

[13] U. Farooq, M. S. Ahmad, S. A. Rakha, N. Ali, A. A. Khurram, and T. Subhani, "Interfacial mechanical performance of composite honeycomb sandwich panels for aerospace applications," *Arab J Sci Eng*, vol. 42, no. 5, pp. 1775–1782, 2017.

[14] A. Redmann, M. C. Montoya-Ospina, R. Karl, N. Rudolph, and T. A. Osswald, "High-force dynamic mechanical analysis of composite sandwich panels for aerospace structures," *Composites Part C: Open Access*, vol. 5, p. 100136, 2021.

[15] M. M. Sychov, L. A. Lebedev, S. V Dyachenko, and L. A. Nefedova, "Mechanical properties of energy-absorbing structures with triply periodic minimal surface topology," *Acta Astronaut*, vol. 150, pp. 81–84, 2018.

[16] O. Rahman, K. Z. Uddin, J. Muthulingam, G. Youssef, C. Shen, and B. Koohbor, "Density-Graded Cellular Solids: Mechanics, Fabrication, and Applications," *Adv Eng Mater*, vol. 24, no. 1, p. 2100646, 2022.

[17] G. Palomba, T. Hone, D. Taylor, and V. Crupi, "Bio-inspired protective structures for marine applications," *Bioinspir Biomim*, vol. 15, no. 5, p. 056016, 2020.

[18] J. F. Davalos, P. Qiao, X. F. Xu, J. Robinson, and K. E. Barth, "Modeling and characterization of fiber-reinforced plastic honeycomb sandwich panels for highway bridge applications," *Compos Struct*, vol. 52, no. 3–4, pp. 441–452, 2001.

[19] G. Savio, S. Rosso, R. Meneghello, and G. Concheri, "Geometric modeling of cellular materials for additive manufacturing in biomedical field: a review," *Appl Bionics Biomech*, vol. 2018, 2018.

[20] L. E. Murr *et al.*, "Next-generation biomedical implants using additive manufacturing of complex, cellular and functional mesh arrays," *Philosophical Transactions of the Royal Society A: Mathematical, Physical and Engineering Sciences*, vol. 368, no. 1917, pp. 1999–2032, 2010.

[21] M. A. El-Sayed, K. Essa, M. Ghazy, and H. Hassanin, "Design optimization of additively manufactured titanium lattice structures for biomedical implants," *The International Journal of Advanced Manufacturing Technology*, vol. 110, pp. 2257–2268, 2020.

[22] S. Pramanik, D. Milaege, K.-P. Hoyer, and M. Schaper, "Additively manufactured novel Ti6Al7Nb circular honeycomb cellular solid for energy absorbing applications," *Materials Science and Engineering: A*, vol. 854, p. 143887, 2022.

[23] K. Boomsma, D. Poulikakos, and F. Zwick, "Metal foams as compact high performance heat exchangers," *Mechanics of materials*, vol. 35, no. 12, pp. 1161–1176, 2003.

[24] A. Ejlali, A. Ejlali, K. Hooman, and H. Gurgenci, "Application of high porosity metal foams as air-cooled heat exchangers to high heat load removal systems," *International Communications in Heat and Mass Transfer*, vol. 36, no. 7, pp. 674–679, 2009.

[25] T. Wen, J. Tian, T. J. Lu, D. T. Queheillalt, and H. N. G. Wadley, "Forced convection in metallic honeycomb structures," *Int J Heat Mass Transf*, vol. 49, no. 19–20, pp. 3313–3324, 2006.

[26] B. Jiang, Z. Wang, and N. Zhao, "Effect of pore size and relative density on the mechanical properties of open cell aluminum foams," *Scr Mater*, vol. 56, no. 2, pp. 169–172, 2007.

[27] M. J. Silva, W. C. Hayes, and L. J. Gibson, “The effects of non-periodic microstructure on the elastic properties of two-dimensional cellular solids,” *Int J Mech Sci*, vol. 37, no. 11, pp. 1161–1177, 1995.

[28] S. Singh and N. Bhatnagar, “A survey of fabrication and application of metallic foams (1925–2017),” *Journal of Porous Materials*, vol. 25, pp. 537–554, 2018.

[29] V. Srivastava and R. Srivastava, “On the polymeric foams: modeling and properties,” *J Mater Sci*, vol. 49, pp. 2681–2692, 2014.

[30] P. Colombo, “Conventional and novel processing methods for cellular ceramics,” *Philosophical Transactions of the Royal Society A: Mathematical, Physical and Engineering Sciences*, vol. 364, no. 1838, pp. 109–124, 2006.

[31] Z. Liu *et al.*, “3D metallic glass cellular structures,” *Acta Mater*, vol. 105, pp. 35–43, 2016.

[32] M. I. Okereke, A. I. Akpoyomare, and M. S. Bingley, “Virtual testing of advanced composites, cellular materials and biomaterials: a review,” *Compos B Eng*, vol. 60, pp. 637–662, 2014.

[33] Y. Yamada, e W. Cui, K. Shimojima, H. Hosokawa, Y. Chino, and M. Mabuchi, “Compressive deformation characteristics of open-cell Mg alloys with controlled cell structure,” *Mater Trans*, vol. 43, no. 6, pp. 1298–1305, 2002.

[34] T. Thomas and G. Tiwari, “Crushing behavior of honeycomb structure: a review,” *International journal of crashworthiness*, 2019.

[35] F. Scarpa, S. Blain, T. Lew, D. Perrott, M. Ruzzene, and J. R. Yates, “Elastic buckling of hexagonal chiral cell honeycombs,” *Compos Part A Appl Sci Manuf*, vol. 38, no. 2, pp. 280–289, 2007.

[36] J. Zhang and M. F. Ashby, “Buckling of honeycombs under in-plane biaxial stresses,” *Int J Mech Sci*, vol. 34, no. 6, pp. 491–509, 1992.

[37] E. Barbero and J. Tomblin, “Euler buckling of thin-walled composite columns,” *Thin-walled structures*, vol. 17, no. 4, pp. 237–258, 1993.

[38] P. R. Jeyakrishnan, K. K. S. K. Chockalingam, and R. Narayanasamy, “Studies on buckling behavior of honeycomb sandwich panel,” *The International Journal of Advanced Manufacturing Technology*, vol. 65, pp. 803–815, 2013.

[39] L. Zhao, Q. Zheng, H. Fan, and F. Jin, “Hierarchical composite honeycombs,” *Mater Des*, vol. 40, pp. 124–129, 2012.

[40] S. Zhang, Y. Ma, and Z. Deng, “Analytical solution and experimental verification for the buckling failure of additively manufactured octagonal honeycombs,” *Compos Struct*, vol. 303, p. 116306, 2023.

[41] H. L. Fan and D. N. Fang, “Modeling and limits of strength of nanoporous foams,” *Mater Des*, vol. 30, no. 5, pp. 1441–1444, 2009.

[42] F. Meraghni, F. Desrumaux, and M. L. Benzeggagh, “Mechanical behaviour of cellular core for structural sandwich panels,” *Compos Part A Appl Sci Manuf*, vol. 30, no. 6, pp. 767–779, 1999.

[43] J. Pflug, F. Xinyu, J. Lavalaye, I. Verpoest, P. Bratfisch, and D. Vandepitte, “Continuously produced honeycomb sandwich materials for automotive applications,” in *at Automotive and Transportation Technology Congress and Exposition. DOI*, 2002, pp. 2001–2002.

[44] G. Palomba, G. Epasto, L. Sutherland, and V. Crupi, “Aluminium honeycomb sandwich as a design alternative for lightweight marine structures,” *Ships and Offshore Structures*, pp. 1–12, 2021.

[45] J. M. Davies, *Lightweight sandwich construction*. John Wiley & Sons, 2008.

[46] F. Cote, V. S. Deshpande, N. A. Fleck, and A. G. Evans, “The out-of-plane compressive behavior of metallic honeycombs,” *Materials Science and Engineering: A*, vol. 380, no. 1–2, pp. 272–280, 2004.

[47] T.-C. Lin, M.-Y. Yang, and J.-S. Huang, “Effects of solid distribution on the out-of-plane elastic properties of hexagonal honeycombs,” *Compos Struct*, vol. 100, pp. 436–442, 2013.

[48] F. Bloom and D. Coffin, *Handbook of thin plate buckling and postbuckling*. CRC Press, 2000.

[49] Y. Wang, “Elastic collapse of honeycombs under out-of-plane pressure,” *Int J Mech Sci*, vol. 33, no. 8, pp. 637–644, 1991.

[50] Y. Wang and S.-H. Lee, “A theoretical model developed for predicting nail withdrawal load from wood by mechanics,” *European Journal of Wood and Wood Products*, vol. 76, pp. 973–978, 2018.

[51] S. Venkataraman, R. T. Haftka, B. Sankar, H. Zhu, and M. L. Blosser, “Optimal functionally graded metallic foam thermal insulation,” *AIAA journal*, vol. 42, no. 11, pp. 2355–2363, 2004.

[52] A. Arjunan, A. Baroutaji, A. S. Praveen, A. G. Olabi, and C. J. Wang, “Acoustic performance of metallic foams,” 2019.

[53] M. Avella, M. Cocca, M. E. Errico, and G. Gentile, “Biodegradable PVOH-based foams for packaging applications,” *Journal of cellular plastics*, vol. 47, no. 3, pp. 271–281, 2011.

[54] R. Attarzadeh, S.-H. Attarzadeh-Niaki, and C. Duwig, “Multi-objective optimization of TPMS-based heat exchangers for low-temperature waste heat recovery,” *Appl Therm Eng*, vol. 212, p. 118448, 2022.

[55] M. Aramesh and B. Shabani, “Metal foam-phase change material composites for thermal energy storage: a review of performance parameters,” *Renewable and Sustainable Energy Reviews*, vol. 155, p. 111919, 2022.

[56] H. Zhang, M. Lei, Z. Lin, W. Gong, J. Shen, and Y. Zhang, “The Compressive Properties and Deformation Mechanism of Closed-Cell Aluminum Foam with

High Porosity after High-Temperature Treatment," *Sustainability*, vol. 14, no. 16, p. 9850, 2022.

[57] X. N. Liu, Y. X. Li, X. Chen, Y. Liu, and X. L. Fan, "Foam stability in gas injection foaming process," *J Mater Sci*, vol. 45, no. 23, pp. 6481–6493, 2010, doi: 10.1007/s10853-010-4736-5.

[58] A. M. Parvanian, M. Saadatfar, M. Panjepour, A. Kingston, and A. P. Sheppard, "The effects of manufacturing parameters on geometrical and mechanical properties of copper foams produced by space holder technique," *Mater Des*, vol. 53, pp. 681–690, 2014, doi: https://doi.org/10.1016/j.matdes.2013.07.047.

[59] B. Xie, Y. Z. Fan, T. Z. Mu, and B. Deng, "Fabrication and energy absorption properties of titanium foam with CaCl2 as a space holder," *Materials Science and Engineering A*, vol. 708, pp. 419–423, 2017, doi: 10.1016/j.msea.2017.09.123.

[60] Y. Liu, Y. Li, H. Zhang, and J. Wan, "Effect of Gasar processing parameters on structure of lotus-type porous magnesium," *Xiyou Jinshu Cailiao Yu Gongcheng/Rare Metal Materials and Engineering*, vol. 34, no. 7, pp. 1128–1130, 2005, [Online]. Available: https://www.scopus.com/inward/record.uri?eid=2-s2.0-23444462472&partnerID=40&md5=60141509bf5d3ce31125b1ab4ecde20c

[61] B. John, "Manufacture, characterisation and application of cellular metals and metal foams," *Prog Mater Sci*, vol. 46, no. 6, pp. 559–632, 2001, doi: 10.1016/s0079-6425(00)00002-5.

[62] Y. Hangai, K. Zushida, H. Fujii, R. Ueji, O. Kuwazuru, and N. Yoshikawa, "Friction powder compaction process for fabricating open-celled Cu foam by sintering-dissolution process route using NaCl space holder," *Materials Science and Engineering: A*, vol. 585, pp. 468–474, 2013, doi: https://doi.org/10.1016/j.msea.2013.08.004.

[63] M. Alkhader and M. Vural, "Mechanical response of cellular solids: Role of cellular topology and microstructural irregularity," *Int J Eng Sci*, vol. 46, no. 10, pp. 1035–1051, 2008, doi: 10.1016/j.ijengsci.2008.03.012.

[64] R. Brezny and D. J. Green, "The effect of cell size on the mechanical behavior of cellular materials," *Acta metallurgica et materialia*, vol. 38, no. 12, pp. 2517–2526, 1990, doi: 10.1016/0956-7151(90)90263-g.

[65] P. Kenesei, C. Kádár, Z. S. Rajkovits, and J. Lendvai, "The influence of cell-size distribution on the plastic deformation in metal foams," *Scr Mater*, vol. 50, no. 2, pp. 295–300, 2004.

[66] C. Tekog, L. J. Gibson, T. Pardoen, and P. R. Onck, "Size effects in foams: Experiments and modeling," *Prog Mater Sci*, vol. 56, no. 2, pp. 109–138, 2011.

[67] H. X. Zhu and A. H. Windle, "Effects of cell irregularity on the high strain compression of open-cell foams," *Acta Mater*, vol. 50, no. 5, pp. 1041–1052, 2002, doi: 10.1016/s1359-6454(01)00402-5.

[68] T. G. Nieh, K. Higashi, and J. Wadsworth, “Effect of cell morphology on the compressive properties of open-cell aluminum foams,” *Materials Science and Engineering: A*, vol. 283, no. 1–2, pp. 105–110, 2000.

[69] Y. An, P. D. Hodgson, and C. Yang, “Investigation of cell shape effect on the mechanical behaviour of open-cell metal foams,” *Comput Mater Sci*, vol. 55, pp. 1–9, 2012.

[70] E. W. Andrews and L. J. Gibson, “The influence of crack-like defects on the tensile strength of an open-cell aluminum foam,” *Scr Mater*, vol. 44, no. 7, pp. 1005–1010, 2001, doi: 10.1016/s1359-6462(01)00673-x.

[71] C. Chen, T. J. Lu, and N. A. Fleck, “Effect of imperfections on the yielding of two-dimensional foams,” *J Mech Phys Solids*, vol. 47, no. 11, pp. 2235–2272, 1999.

[72] M. Alkhader and M. Vural, “The partition of elastic strain energy in solid foams and lattice structures,” *Acta Mater*, vol. 57, no. 8, pp. 2429–2439, 2009, doi: 10.1016/j.actamat.2009.01.034.

[73] M. Alkhader and M. Vural, “An energy-based anisotropic yield criterion for cellular solids and validation by biaxial FE simulations,” *J Mech Phys Solids*, vol. 57, no. 5, pp. 871–890, 2009, doi: 10.1016/j.jmps.2008.12.005.

[74] M. Alkhader and M. Vural, “A plasticity model for pressure-dependent anisotropic cellular solids,” *Int J Plast*, vol. 26, no. 11, pp. 1591–1605, 2010.

[75] M. Alkhader and M. Vural, “IMECE2006-15638 Influence of Cellular Topology on Dynamic Response of Solid Foams,” *ASME APPLIED MECHANICS DIVISION-PUBLICATIONS-AMD*, vol. 257, p. 199, 2006.

[76] V. S. Deshpande and N. A. Fleck, “High strain rate compressive behaviour of aluminium alloy foams,” *Int J Impact Eng*, vol. 24, no. 3, pp. 277–298, 2000, doi: 10.1016/s0734-743x(99)00153-0.

[77] S. F. Fischer, “Energy absorption efficiency of open-cell pure aluminum foams,” *Mater Lett*, vol. 184, pp. 208–210, 2016.

[78] M. Iasiello, N. Bianco, W. K. S. Chiu, and V. Naso, “The effects of variable porosity and cell size on the thermal performance of functionally-graded foams,” *International Journal of Thermal Sciences*, vol. 160, p. 106696, 2021, doi: https://doi.org/10.1016/j.ijthermalsci.2020.106696.

[79] Y. Boonyongmaneerat, C. A. Schuh, and D. C. Dunand, “Mechanical properties of reticulated aluminum foams with electrodeposited Ni–W coatings,” *Scr Mater*, vol. 59, no. 3, pp. 336–339, 2008, doi: https://doi.org/10.1016/j.scriptamat.2008.03.035.

[80] W. Wang, R. Burgueño, J.-W. Hong, and I. Lee, “Nano-deposition on 3-D open-cell aluminum foam materials for improved energy absorption capacity,” *Materials Science and Engineering: A*, vol. 572, pp. 75–82, 2013, doi: https://doi.org/10.1016/j.msea.2013.02.032.

[81] Y. Sun, R. Burgueño, A. J. Vanderklok, S. A. Tekalur, W. Wang, and I. Lee, "Compressive behavior of aluminum/copper hybrid foams under high strain rate loading," *Materials Science and Engineering: A*, vol. 592, pp. 111–120, 2014, doi: https://doi.org/10.1016/j.msea.2013.10.104.

[82] C. Devivier, V. Tagliaferri, F. Trovalusci, and N. Ucciardello, "Mechanical characterization of open cell aluminium foams reinforced by nickel electro-deposition," *Mater Des*, vol. 86, pp. 272–278, 2015.

[83] A. Jung, E. Lach, and S. Diebels, "New hybrid foam materials for impact protection," *Int J Impact Eng*, vol. 64, pp. 30–38, 2014.

[84] A. Jung, J. Luksch, S. Diebels, F. Schäfer, and C. Motz, "In-situ and ex-situ microtensile testing of individual struts of Al foams and Ni/Al hybrid foams," *Mater Des*, vol. 153, pp. 104–119, 2018, doi: https://doi.org/10.1016/j.matdes.2018.04.075.

[85] S. Mancin, C. Zilio, A. Diani, and L. Rossetto, "Air forced convection through metal foams: Experimental results and modeling," *Int J Heat Mass Transf*, vol. 62, pp. 112–123, 2013.

[86] M. Alipanah and X. Li, "Numerical studies of lithium-ion battery thermal management systems using phase change materials and metal foams," *Int J Heat Mass Transf*, vol. 102, pp. 1159–1168, 2016, doi: https://doi.org/10.1016/j.ijheatmasstransfer.2016.07.010.

[87] Y. Amani, S. Dancette, J. Luksch, A. Jung, and E. Maire, "Micro-tensile behavior of struts extracted from an aluminum foam," *Mater Charact*, vol. 166, p. 110456, 2020.

[88] T. Wan, Y. Liu, C. Zhou, X. Chen, and Y. Li, "Fabrication, properties, and applications of open-cell aluminum foams: A review," *J Mater Sci Technol*, vol. 62, pp. 11–24, 2021.

[89] H. Zhang, W. J. Suszynski, K. V. Agrawal, M. Tsapatsis, S. Al Hashimi, and L. F. Francis, "Coating of open cell foams," *Ind Eng Chem Res*, vol. 51, no. 27, pp. 9250–9259, 2012.

[90] A. Antenucci, S. Guarino, V. Tagliaferri, and N. Ucciardello, "Improvement of the mechanical and thermal characteristics of open cell aluminum foams by the electrodeposition of Cu," *Mater Des*, vol. 59, pp. 124–129, 2014.

[91] A. Jung, H. Natter, S. Diebels, E. Lach, and R. Hempelmann, "Nanonickel coated aluminum foam for enhanced impact energy absorption," *Adv Eng Mater*, vol. 13, no. 1-2, pp. 23–28, 2011.

[92] O. Al-Osman, M. Alkhader, and W. Abuzaid, "Enhancing the multifunctionality of open-cell foams through tailoring their thermal and mechanical properties using coatings," *European Journal of Mechanics-A/Solids*, vol. 99, p. 104923, 2023.

[93] S. Talebi, M. Sadighi, and M. M. Aghdam, "Numerical and experimental analysis of the closed-cell aluminium foam under low velocity impact using

computerized tomography technique," *Acta Mechanica Sinica*, vol. 35, pp. 144–155, 2019.

[94] A. Jung, L. A. A. Beex, S. Diebels, and S. P. A. Bordas, "Open-cell aluminium foams with graded coatings as passively controllable energy absorbers," *Mater Des*, vol. 87, pp. 36–41, 2015.

[95] Y. Shajari, L. Nikzad, and M. Razavi, "Investigation on mechanical properties of nickel open cell metal foam after heat treatment," *Sci Rep*, vol. 13, no. 1, p. 16569, 2023.

[96] C. Grill, M. Fries, A. Jung, and S. Diebels, "Numerical and experimental investigations of the electrodeposition process on open porous foams, determination of the parameter influence on the coating homogeneity," *Int J Heat Mass Transf*, vol. 180, p. 121791, 2021.

[97] S. Sengupta, A. Patra, S. Jena, K. Das, and S. Das, "A study on the effect of electrodeposition parameters on the morphology of porous nickel electrodeposits," *Metallurgical and Materials Transactions A*, vol. 49, pp. 920–937, 2018.

[98] A. Kyner, K. Dharmasena, K. Williams, V. Deshpande, and H. Wadley, "Response of square honeycomb core sandwich panels to granular matter impact," *Int J Impact Eng*, vol. 117, pp. 13–31, 2018.

[99] M. E. Çetin, "Investigation of carbon nanotube reinforcement to polyurethane adhesive for improving impact performance of carbon fiber composite sandwich panels," *Int J Adhes Adhes*, vol. 112, p. 103002, 2022.

[100] B. V. Ramnath, K. Alagarraja, and C. Elanchezhian, "Review on sandwich composite and their applications," *Mater Today Proc*, vol. 16, pp. 859–864, 2019.

[101] X. Li, P. Zhang, Z. Wang, G. Wu, and L. Zhao, "Dynamic behavior of aluminum honeycomb sandwich panels under air blast: Experiment and numerical analysis," *Compos Struct*, vol. 108, pp. 1001–1008, 2014.

[102] B. Hou, H. Zhao, S. Pattofatto, J. G. Liu, and Y. L. Li, "Inertia effects on the progressive crushing of aluminium honeycombs under impact loading," *Int J Solids Struct*, vol. 49, no. 19–20, pp. 2754–2762, 2012.

[103] D. Asprone, F. Auricchio, C. Menna, S. Morganti, A. Prota, and A. Reali, "Statistical finite element analysis of the buckling behavior of honeycomb structures," *Compos Struct*, vol. 105, pp. 240–255, 2013.

[104] Y. Zhang, X. Liu, Y. Zhou, and Y. Shi, "Uniaxial compressive performance of an aramid and aluminum honeycomb sandwich structure," *Ocean Engineering*, vol. 270, p. 113676, 2023.

[105] M. Safarabadi, M. Haghighi-Yazdi, M. A. Sorkhi, and A. Yousefi, "Experimental and numerical study of buckling behavior of foam-filled honeycomb core sandwich panels considering viscoelastic effects," *Journal of Sandwich Structures & Materials*, vol. 23, no. 8, pp. 3985–4015, 2021.

[106] W. Miller, C. W. Smith, F. Scarpa, and K. E. Evans, “Flatwise buckling optimization of hexachiral and tetrachiral honeycombs,” *Compos Sci Technol*, vol. 70, no. 7, pp. 1049–1056, 2010.

[107] Y. Zhong, Z. Shi, Q. Luo, and M. Zhang, “A simplified semi-analytical model for predicting the global and local responses of hybrid honeycomb-like sandwich panel,” *Thin-Walled Structures*, vol. 182, p. 110307, 2023.

[108] M. Shendy, M. Alkhader, B. A. Abu-Nabah, M. A. Jaradat, and T. A. Venkatesh, “Machine learning assisted approach to design lattice materials with prescribed band gap characteristics,” *European Journal of Mechanics - A/Solids*, vol. 102, p. 105125, 2023, doi: https://doi.org/10.1016/j.euromechsol.2023.105125.

[109] Y. Chen, F. Qian, L. Zuo, F. Scarpa, and L. Wang, “Broadband and multiband vibration mitigation in lattice metamaterials with sinusoidally-shaped ligaments,” *Extreme Mech Lett*, vol. 17, pp. 24–32, 2017.

[110] L. J. Gibson and M. F. Ashby, *Cellular solids: structure and properties*. Cambridge university press, 1999.

[111] Z. Li *et al.*, “Fabrication and failure mechanisms of all-composite honeycomb sandwich cylinder under the axial compression,” *Compos Part A Appl Sci Manuf*, vol. 161, p. 107075, 2022.

[112] M. Stanczak, T. Fras, L. Blanc, P. Pawlowski, and A. Rusinek, “Blast-induced compression of a thin-walled aluminum honeycomb structure—Experiment and modeling,” *Metals (Basel)*, vol. 9, no. 12, p. 1350, 2019.

[113] S. Akram, S. H. I. Jaffery, M. Khan, M. Fahad, A. Mubashar, and L. Ali, “Numerical and experimental investigation of Johnson–Cook material models for aluminum (Al 6061-T6) alloy using orthogonal machining approach,” *Advances in Mechanical Engineering*, vol. 10, no. 9, p. 1687814018797794, 2018.

[114] D. R. Lesuer, G. J. Kay, and M. M. LeBlanc, “Modeling large-strain, high-rate deformation in metals,” Lawrence Livermore National Lab.(LLNL), Livermore, CA (United States), 2001.

[115] A. L. Lyford, R. K. Kapania, and T. Stoumbos, “Honeycomb Core Failure Prediction in Joint using Nonlinear Finite Element Analysis,” in *58th AIAA/ASCE/AHS/ASC Structures, Structural Dynamics, and Materials Conference*, 2017, p. 1604.

[116] F. Xia, Y. Durandet, P. J. Tan, and D. Ruan, “Three-point bending performance of sandwich panels with various types of cores,” *Thin-Walled Structures*, vol. 179, p. 109723, 2022, doi: https://doi.org/10.1016/j.tws.2022.109723.

[117] M. Kashif Khan and Q. Y. Wang, “Experimental and finite element based investigations of in-plane and out-of-plane properties of aluminum honeycomb,” in *Applied mechanics and materials*, Trans Tech Publ, 2013, pp. 111–116.

[118] Z. Zhi, H. Chen, J. P. Longtin, M. Alkhader, and T. A. Venkatesh, “Computational modeling of through-thickness flow and pressure drop

characteristics in woven matrix porous media," *International Journal of Modelling and Simulation*, vol. 40, no. 3, pp. 163–183, 2020.

[119] B. Boots, K. Sugihara, S. N. Chiu, and A. Okabe, "Spatial tessellations: concepts and applications of Voronoi diagrams," 2009.

[120] T. Miyoshi, M. Itoh, S. Akiyama, and A. Kitahara, "ALPORAS aluminum foam: Production process, properties, and applications," *Adv Eng Mater*, vol. 2, no. 4, pp. 179–183, 2000, doi: 10.1002/(SICI)1527-2648(200004)2:4<179::AID-ADEM179>3.0.CO;2-G.

[121] P. R. Onck, E. W. Andrews, and L. J. Gibson, "Size effects in ductile cellular solids. Part I: modeling," *Int J Mech Sci*, vol. 43, no. 3, pp. 681–699, 2001.

[122] C. Sun, L. Guo, G. Lu, Y. Lv, and F. Ye, "Interface bonding between particle and substrate during HVOF spraying," *Appl Surf Sci*, vol. 317, pp. 908–913, 2014.

[123] L. E. Iliescu, A. A. Lakis, and A. Oulmane, "Satellites-spacecraft materials and hypervelocity impact (HVI) testing: Numerical simulations," *Eur. J. Mech. Eng. Res*, vol. 3, no. 3, pp. 41–77, 2016.

[124] H. X. Zhu, J. F. Knott, and N. J. Mills, "Analysis of the elastic properties of open-cell foams with tetrakaidecahedral cells," *J Mech Phys Solids*, vol. 45, no. 3, pp. 319–343, 1997.

[125] F. P. Beer, E. R. Johnston, J. T. DeWolf, and D. F. Mazurek, "Mechanics of materials. 7th_edition," *New York. MeGraw-Hill Education Ltd*, 2015.

[126] M. Alkhader, W. Abuzaid, M. Elyoussef, and S. Al-Adaileh, "Localized strain fields in honeycomb materials with convex and concaved cells," *European Journal of Mechanics - A/Solids*, p. 103890, 2019, doi: https://doi.org/10.1016/j.euromechsol.2019.103890.

[127] A. Ahmed, M. Alkhader, and B. Abu-Nabah, "In-plane elastic wave propagation in aluminum honeycomb cores fabricated by bonding corrugated sheets," *Journal of Sandwich Structures & Materials*, p. 1099636217729569, 2017.

[128] C. Zing, S. Mahjoob, and K. Vafai, "Analysis of porous filled heat exchangers for electronic cooling," *Int J Heat Mass Transf*, vol. 133, pp. 268–276, 2019, doi: https://doi.org/10.1016/j.ijheatmasstransfer.2018.12.067.

[129] A. Bhattacharya, V. V Calmidi, and R. L. Mahajan, "Thermophysical properties of high porosity metal foams," *Int J Heat Mass Transf*, vol. 45, no. 5, pp. 1017–1031, 2002.

[130] K. Boomsma and D. Poulikakos, "On the effective thermal conductivity of a three-dimensionally structured fluid-saturated metal foam," *Int J Heat Mass Transf*, vol. 44, no. 4, pp. 827–836, 2001.

[131] M. A. A. Mendes, S. Ray, and D. Trimis, "A simple and efficient method for the evaluation of effective thermal conductivity of open-cell foam-like structures," *Int J Heat Mass Transf*, vol. 66, pp. 412–422, 2013.

[132] E. Sadeghi, N. Djilali, and M. Bahrami, “Thermal conductivity and thermal contact resistance of metal foams,” in *Heat Transfer Summer Conference*, 2009, pp. 355–365.

[133] H. Yang, Y. Li, Y. Yang, D. Chen, and Y. Zhu, “Effective thermal conductivity of high porosity open-cell metal foams,” *Int J Heat Mass Transf*, vol. 147, p. 118974, 2020, doi: https://doi.org/10.1016/j.ijheatmasstransfer.2019.118974.

[134] N. Budynas and J. K. Nisbett, “Shigley’s Mechanical Engginering Design,” *Mechanical Engineering*, vol. 2, p. 904436, 2006.

[135] I. G. Masters and K. E. Evans, “Models for the elastic deformation of honeycombs,” *Compos Struct*, vol. 35, no. 4, pp. 403–422, 1996, doi: http://dx.doi.org/10.1016/S0263-8223(96)00054-2.

Vita

Omar Abdulhadi Al Osman was born in 1996, in Sharjah, United Arabi Emirates. He was educated in local public schools and graduated from Al Mawakeb-Garhoud School with distinction in 2013. He was admitted to the American University of Sharjah, United Arab Emirates, from which he graduated with a BSc in Civil Engineering in 2018.

Omar has then moved to the United Kingdom to pursue his master's degree in Structural Engineering at the University of Glasgow. He graduated in 2020 and continued working as a lab tutor, teaching and aiding in Finite Element Analysis lectures and laboratory work. Omar joined the Ph.D. program in Material Science and Engineering at the American University of Sharjah in Fall 2020. As a Ph.D. student, he has published two conference papers titled "Dynamic compressive response of coated open-cell aluminum foam" and "Flexural response of sandwich structures comprising topologically perturbed cores" and a journal paper titled "Enhancing the multifunctionality of open-cell foams through tailoring their thermal and mechanical properties using coatings".